UNIVERSITY OF OKLAHOMA

GRADUATE COLLEGE

NUMERICAL STUDY ON CASING INTEGRITY DURING HYDRAULIC

FRACTURING SHALE FORMATION

A THESIS

SUBMITTED TO THE GRADUATE FACULTY

in partial fulfillment of the requirements for the

Degree of

MASTER OF SCIENCE

By

XIAYE WU
Norman, Oklahoma
2019

NUMERICAL SIMULATION OF HYDRAULICALLY INDUCED CASING
DEFORMATION IN SHALE RESERVOIR

A THESIS APPROVED FOR THE
MEWBOURNE SCHOOL OF PETROLEUM AND GEOLOGICAL ENGINEERING

BY THE COMMITTEE CONSISTING OF

Dr. Xingru Wu, Chair

Dr. Catalin Teodoriu

Dr. Hamidreza Karami

Acknowledgements

I would like to express my deepest thankfulness to my advisor, Dr. Xingru Wu for his numerous supports during this research study. Dr. Wu had shown me the essential qualities that must be achieved as a professional technical specialist. I have learned to keep the passion, be focus, stay patient, and no fear of any challenge that I might face in my career.

I also like to acknowledge my committee member, Dr. Catalin Teodoriu. He has helped me in general as he provided huge details about field situations, which are critical for any engineer as no theory should be established without practical purposes. From him, I have learned the importance of compromise between theory and realistic, which should be accomplished by any engineer who pursues an engineering career. I appreciated Dr. Karami's kindness. And thank him for agreeing to become my committee.

I would like to express my gratitude to my parents, not only for their support for providing me this opportunity to study abroad but also as guides in my life. Their strength of character, courage while facing difficulties and a strong sense of responsibility have set a model to me. I admire them as predecessors of life and would always keep trying to do better.

Finally, I would like to thank all my friends Qianwen Liu, Jiali Zhang, and Junwen Huo. They have provided a great amount of mental support throughout the entire period of my oversea study. Also, my friends in Sarkeys Energy Center: Kai Wang, and Hao Xiong. I will never forget these days that we spent doing research on 13th floor.

Table of Contents

List of Tables

List of Figures

X

Abstract

Due to complex sedimentation environment, shale formations are usually characterized as highly heterogeneous and anisotropic in in-situ stresses. The injection process for reservoir stimulation changes the local in-situ stresses in a quick and significant manner. Activation of existing geo-features is frequently observed by researchers. The large magnitude of matrix displacement potentially deforms the casing which cut through the discontinuous plane, weakly bonded interfaces, and bedding planes. Casing deformations during hydraulic fracturing have been observed in the Southwest China Sichuan basin, which impeded shale gas development. This research analyzed this phenomenon and discuss practical engineering solutions.

The theoretical geomechanics studies indicate water-induced shear will activate shale formation. This study used the finite element model to study the casing-cement-formation geostatistical conditions under hydraulic fracturing. And studied risks for hydraulic fractures intersecting with casings in different aspects. It discussed major mechanisms that govern this interaction behavior. Fluid flow rate and in-situ stresses are two main parameter that induced anisotropic stresses onto casing-fault. A high injection rate (0.005m/s) can apply over 600 MPa unbalanced stress on casing on the top part of casing-fault intersection. Anisotropic in-situ stresses can apply over 100 MPa stress on casing during hydraulic fracturing. This type of casing damage can be reduced by improving stimulation design, adjust the perforation location, and improve the strength of the casing-cement system.

Chapter 1: Introduction

1.1 Problem Statement

The Longmaxi formation in China Sichuan basin was a shale gas resource and has been producing since 2005. The Sichuan basin covers around 44.5 million acres, including 106 gas fields and 14 oil fields. The pilot well in Changning-Weiyuan area was drilled in 2009. The first production well Wei-201 was drilled in 2010 and produced 106 BCF in 2015. Multiple horizontal and multiple fractured wells were drilled through a common drilling pad and each well was about 1338 ft apart. However, the complex stratigraphic environment had impeded its development. Hydraulic fracture had resulted in casing damage in this area. Several attempts such as increase steel grade and strengthen its connection had been tried with some success. This study used data source from CNPC and examined the potential rationale that caused severe casing deformation in this area.

Deformation or failure of casing occurred at the dogleg and the horizontal extent with similar possibilities. This study aims to summarize the past casing deformation analysis and propose a 3D casing-fault intersect model for stress analysis during fluid injection. The following objectives were studied in specific:

- Hydraulic fracture and natural fracture interaction behavior, and its impacts upon formation parameters from formerly lab experiments and numerical simulations
- Summarize and discuss geological settings in Changning-Weiyuan area compare with shale gas play in the United States
- The significance of fracture mechanism, the leak-off mechanism for casing failures analysis during hydraulic fracture in the Changning-Weiyuan area.

- Studied potential parameters, including cement qualities and casing qualities, for the purpose of exploring the possible operational solution for decrease deformation magnitude.

1.2 Background of Longmaxi

The depth of Longmaxi formation in studied areas varies from 4921 ft to over 11483 ft, with the pay zone shale thickness ranging from 69 ft to 525 ft [1]. The mineral analysis shows that the quartz composition ranges from 29% to 33%, and clay from 40% to 43%. Reservoir Total Organic Content (TOC) is 1-4%, and porosity ranges from 1% to 8%. Longmaxi formation is characterized by ultra-low permeability varying from 0.001 mD to 0.1 mD [2]. A cross-section map is shown in **Figure 1**, and the Longmaxi formation has 2 sequences in thickness from 56 ft to 653 ft. The lower Silurian Longmaxi and Wufeng shale were deposited in a deep shelf environment (**Figure 2**). The upper section of Longmaxi Formation deposited in a shallower water-continental environment and their lithologies mainly consist of siltstone and gray mudstone [2]. Compared with the United States stress regime map shown in Error! Reference source not found., Sichuan basin has a complex stress regime (**Figure 3**). This complexity brings problems during hydraulic fracturing. The stress maps show that normal fault and strike-slip fault concentrated in the basin area and thrust faulting aligned around the basin edge. Normal fault in the N-S orientation and strike-slip fault are mainly in the northeast-southwest direction. **Figure 4** reveals the detailed lithology and TOC contents of 3 members from Longmaxi formation are the type II organic matter [4]. Member 4 has a higher porosity and fracture density but lower gas content, while member 2 is enriched of TOC and gas content.
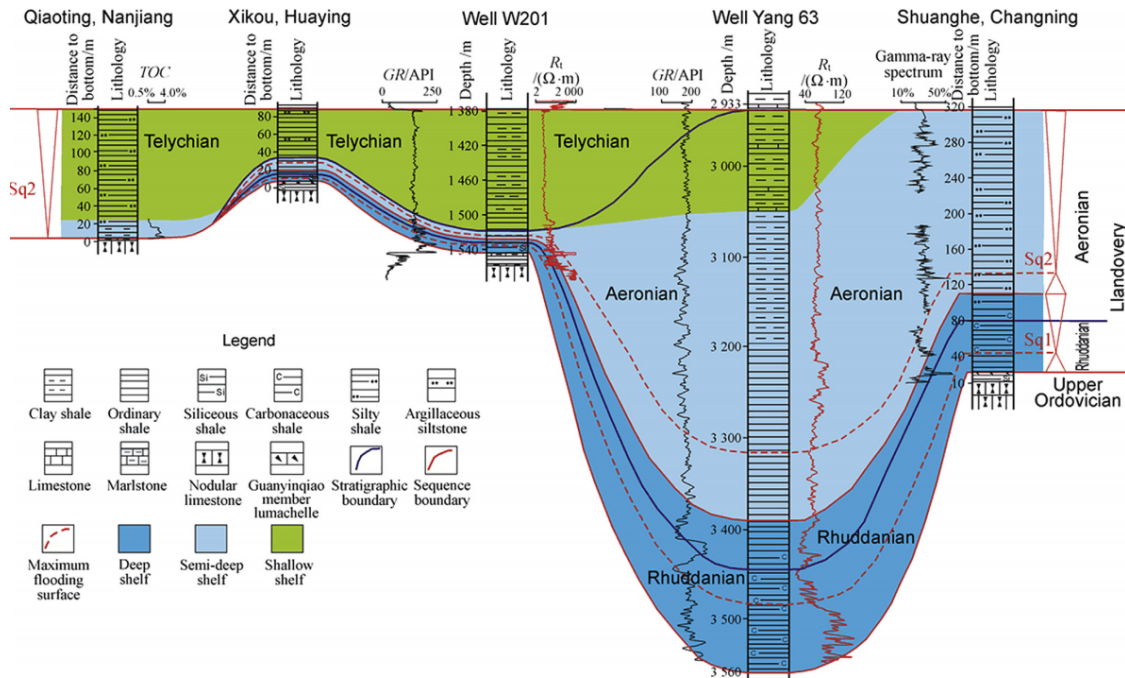
Figure 1: Stratigraphic sequence of Longmaxi formation in the north-south direction [1]. There are 2 sequences in Longmaxi shale gas play, Sq1 has a thickness of 20 meters and Sq2 has a thickness about 200 meters.

Figure 2: Stratigraphic units in the Fuling area with Wufeng and Longmaxi formations [2]. The mineralogy of Longmaxi formation is a major carbonaceous shale.
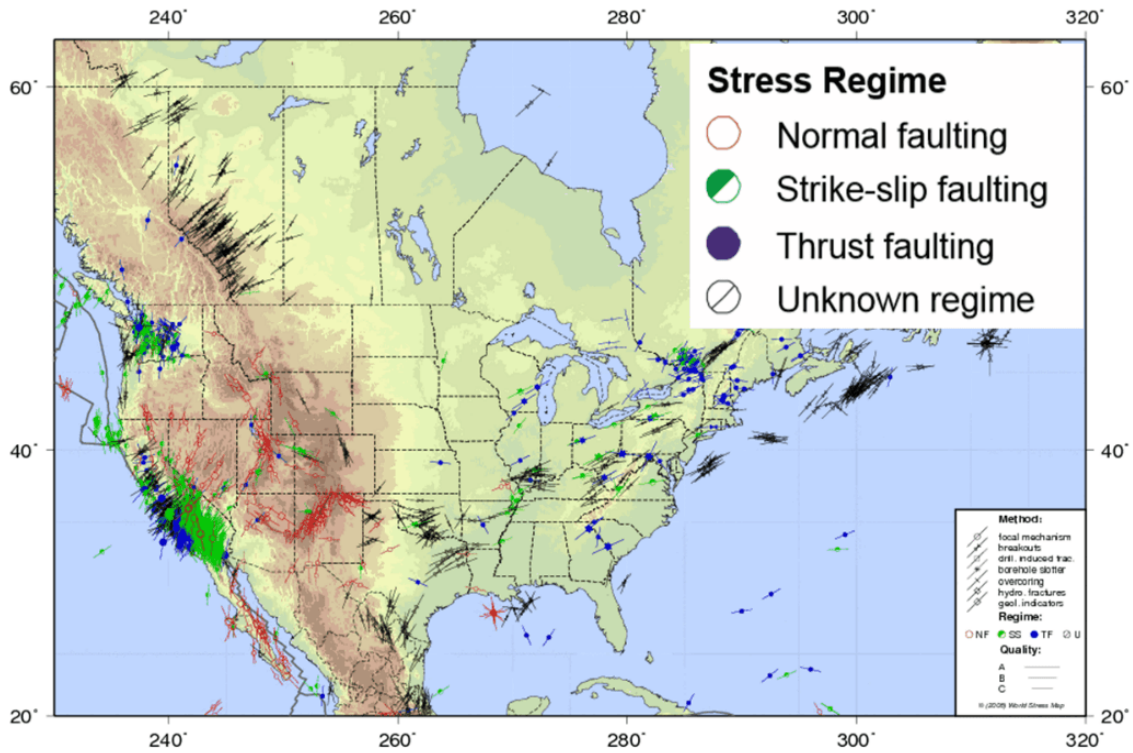
Figure 3: Stress map for United States (World Stress Map).
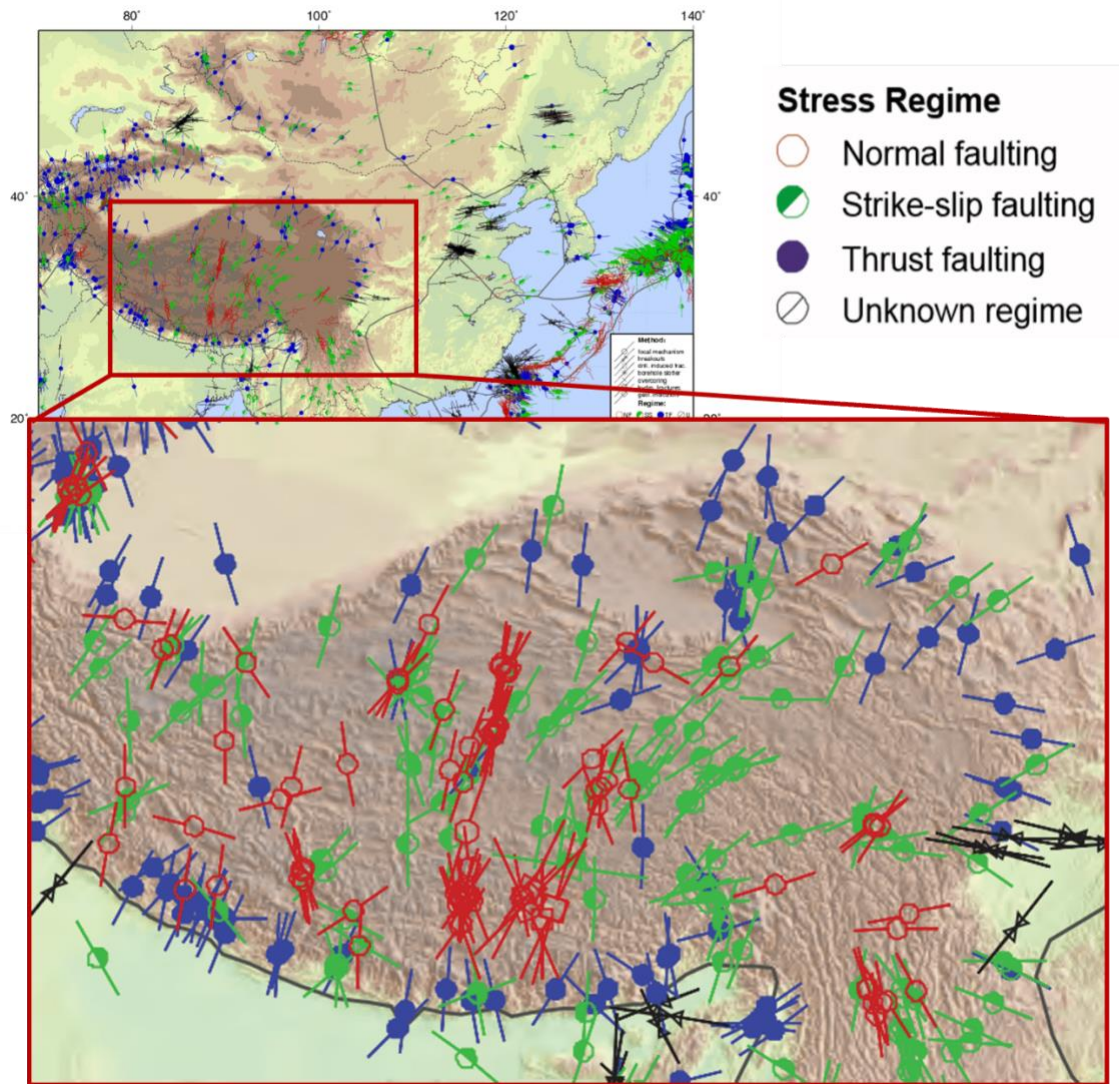
Figure 3: Stress map for Sichuan Basin (World Stress Map).
Stress regimes alternate largely and cross each other in the basin area.
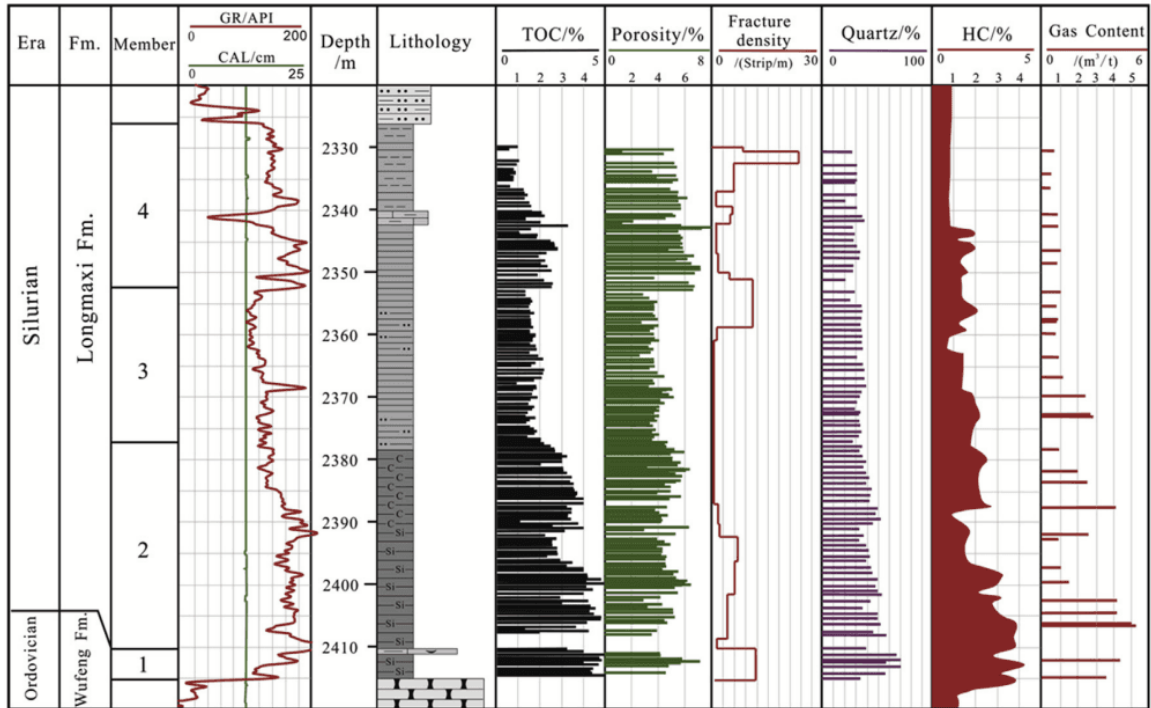
Figure 4: Wufeng-Longmaxi formation in Jiaoshiba, Fuling 4.
TOC, hydrocarbon, and Gas content clearly change across lithology boundaries between members 2, 3, and 4. Organic porosity is the major porosity type.

1.3   Organization of this Thesis

Chapter 1 states research objectives and introduced the background of Longmaxi formation, Changning-Weiyuan operation block. Chapter 2 summarizes previous studies related to the interaction of hydraulic fracture and natural fracture experimental lab works, reservoir stimulations, and microseismic interpretation for hydraulic fracture network in shale reservoirs. Chapter 3 lists fracture mechanisms and leakoff mechanisms, which govern hydraulic fracture propagation. Chapter 4 covers the methodologies used for fracture initiation and propagation simulation. Chapter 5 includes base models in 2D and 3D with discussions about assumptions and parameter selections. Sensitivity studies in Chapter 6 discussed impacts on injection induced casing stresses from injection rate, casing properties, and cement properties. Chapter 7 summarized this thesis and

concluded the findings. Suggestions for hydraulic fracture operation in Longmaxi and further studies are included.

Chapter 2: Literature Review

This chapter composed of experiment studies and simulation studies for hydraulic fracture and natural fracture intersection behavior. Fracture analysis from microseismic interpretation is included. The lab experiments studied hydraulic fracture propagation in natural fracture enriched reservoirs. Some of the experiment used sample rocks extracted from Longmaxi outcrops. Lab tests used instances with weak interfaces. The weak interfaces indicating natural fracture in the formation. Several simulations studied certain scenario for analyzing different formations. Microseismic interpretation provides the fracture network and the stimulated reservoir volume (SRV). Horizontal and vertical offsets in different magnitude with different fault regimes.

Hydraulic fracturing is used to enhance well flow rates by creating more flow conduits in an unconventional reservoir[5]. By injecting millions of pounds of proppant and gallons of fracturing fluids, operators can produce hydrocarbon resources from the stimulated reservoir volume (SRV). Warpinski, et al. [6] compared the complexity of fracture growth from a field experiment with a basic bi-wing fracture model and concluded a complex fracture would be preferred for wells in tight formations. Fisher, et al. [7] used a microseismic fracture mapping method to analyze the fairway of a complex hydraulic fracture network. They also observed layer debonding in the vertical direction influenced the hydraulic fracture performance. As summarized in **Figure 5**, fracture treatment fluid and proppant volume started to grow exponentially around 2002 with the application of hydraulic fracture technology in unconventional reservoirs [8].

Casing deformations and failures were observed in various unconventional reservoirs with different severity. Using a 3D analytical geomechanical model, Meyer, et.al [9] concluded the most critical parameters of deformation in Montney play was the maximum shear strength magnitude. Over the past few years, operators in the Sichuan basin experienced hydraulic fracturing

incompletion caused by casing deformation. The rate of uncompleted stages reaches up to 18% due to casing deformation [10]. This resulted in reduced well productivity and significant financial loss. Casing deformation also led to sustained casing pressure that will decrease the gas rate [11]. Furthermore, casing failure might compromise the well integrity and cause underground water contamination [12]. Therefore, it is necessary to study casing deformation causes and seek possible solutions for obtaining higher completion rates and production rates.
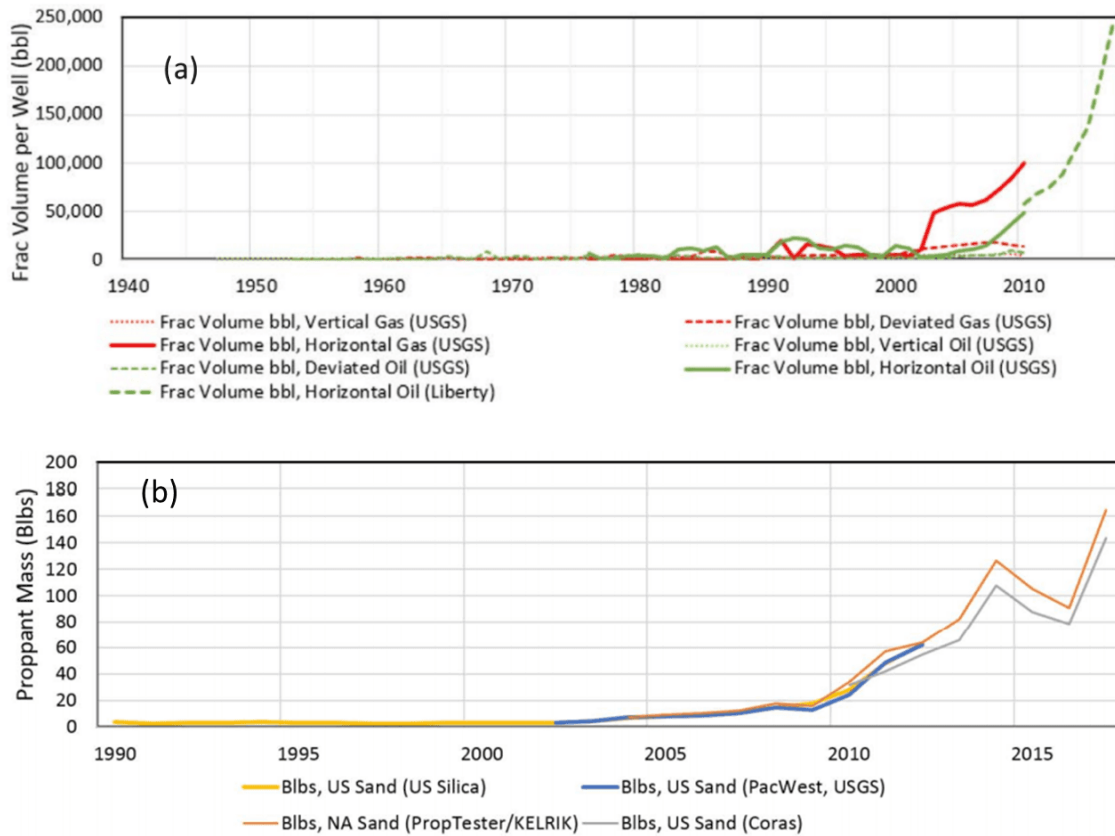
Figure 5: Trend of fracturing fluid and proppant volume [8].
(a) Historical changes to average fracture treatment fluid volume by well. Both horizontal gas (in red) and oil (in green) frac volume in barrel increased exponentially since 2000. (b)Historical changes in the US and North American sand market. The use of proppant was adapted widely since 2010. Although there are changes in the frac water and proppant selections.

2.1   Experiment Studies for Fracture Interaction

Experiments in lab works provide insights for the hydraulic fracture (HF) intersects natural fracture (NF). Fractures intersection was believed to increase the stimulated reservoir volume (SRV) as it provides more fluid conduits. However, faults reactivation may cause relative movements on the opposite sides of fault interfaces. HF intersects with the NF in three ways: penetration, arrested, and dilation[13]. From experiments, the sealed fracture breakdown pressure is 50% or less compare with the matrix breakdown pressure[14].

Table 1 summarizes a comparison of experiment settings for two different works in studying HF intersecting with natural fractures. They studied the influencing parameters on crossing/non-crossing intersection. Studies included the fracture intersection angle, the interface friction coefficient, and the crossing stress ratio. For intersection angle, Bunger, et al. [15] stated a small oblique angle (15° and 30°) offsets hydraulic fracture propagation. They summarized that the contact friction coefficient has minor impacts upon fracture penetration for orthogonal interaction. Experiment results and analytical results using crossing criteria plotted in **Figure 6**. Ma, et al. [16] tested the interaction behavior with a 50° dipping bedding plane and obtained the difference between the formation breakdown pressure and fracture propagation pressure. With the net pressure increasing, injection pressure fluctuated and created a complex fracture network. The injection rate is different for 15 fold but difference of instances size is less than 5 cm. Bunger, et al. [15] recorded the breakdown pressure 27 – 35 MPa for 2 ml/min injection rate. Ma, et al. [16] measured the largest breakdown pressure around 16 MPa with 30 ml/min injection rate for their different experiments.

Table 1: Experiment design for hydraulic fracture and natural fracture interaction study

Author	Bunger et al.	Ma et al.
Samples	Wondabyne sandstone and Adelaide black granite	Lujiaping formation
Young's Modulus (GPa)	15; 102	30 - 35
Sample Size (cm)	40×36×35 and 40×36×15	40 × 40 × 40
Stress (MPa) σ_v	5 - 6	12
Stress (MPa) σ_H	8 - 28	20
Stress (MPa) σ_h	-	3, 6, 9, 12
Injection Rate (ml/min)	2	30
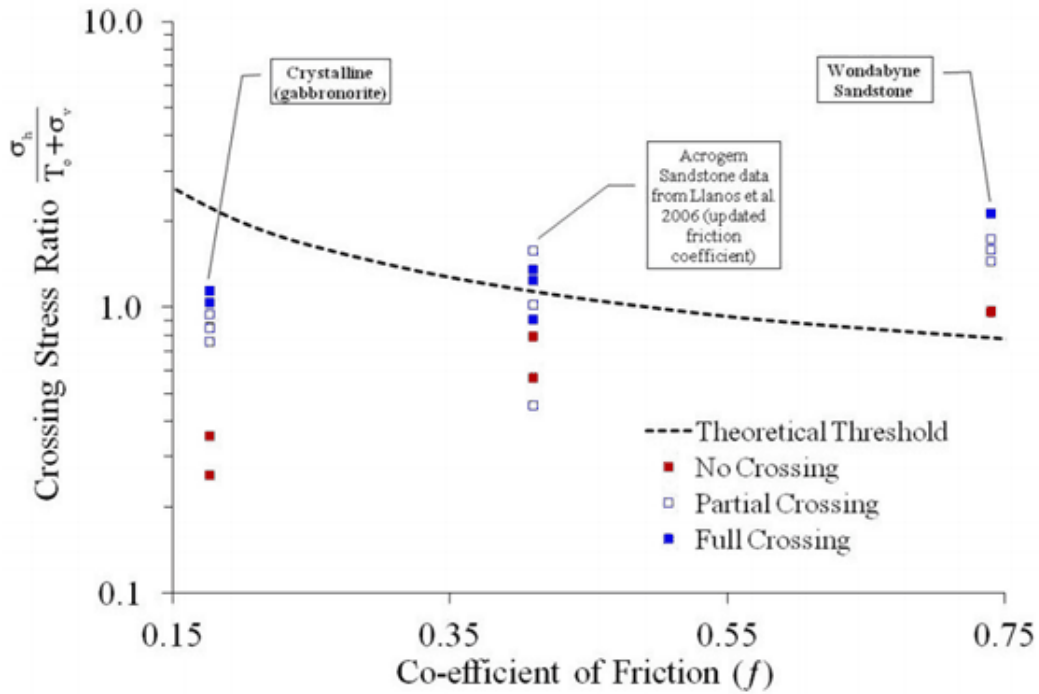
Figure 6: Fracture crossing scenarios versus crossing stress ratio[15].
Experimental results for perpendicular intersection testing Renshaw and Pollard criteria

Experiment from Longmaxi Samples

Ma, et al. [16] studied the SRV of Longmaxi samples using acoustic events (AE). Their samples sizes are 30cm×30cm×30cm containing 1.5cm OD and 0.8 cm ID steel pipes. The horizontal stresses of these instances were at 10MPa and 15Mpa, and the vertical stresses were tested at 15MPa, 25Mpa, and 30MPa. Water was injected through steel pipes at 20 ml/min for 10 minutes. AE recorded from unconducted bedding planes besides the induced fractures during injection. They claimed a high vertical stress difference ($\sigma_v - \sigma_h$) benefits fracture height growth and low vertical stress difference alter fracture orientation parallel to the bedding planes (BP). Only half of the AEs emitted from SRV is revealed in **Figure 7.** These experiments indicate the interpolation of microseismic method might lead to an overestimated SRV.

Other than the far-field in-situ stress, locale permeability anisotropy and the existence of micro-fractures add complexities to the Longmaxi. Ma, et al. [16] measured the permeabilities of 3 Longmaxi cubic samples with a dimension of 20.8cm×19.8cm×22.8 cm and found that the permeabilities in x, y and z-direction can be 2 and 3 orders difference for the samples from the same well. The main reason for this difference was found to be the presence of microfracture for Longmaxi formation.

Yan, et al. [17] studied the friction at fracture interfaces and concluded that the introduction of slickwater possibly reduces friction coefficient from 0.6 for dry matrix down to 0.36 for slickwater wet shale (**Figure 8**). They observed micro-slip happened before the major plane failure and attribute it to the friction drop. In addition, **Figure 9** reveals that the energy release peak rate for the wet sample is half of the rate for the dry sample. Maximum axial failure stress for wet shale samples is also half of the dry samples. This experiment indicating weakening of shale strength during injection process.
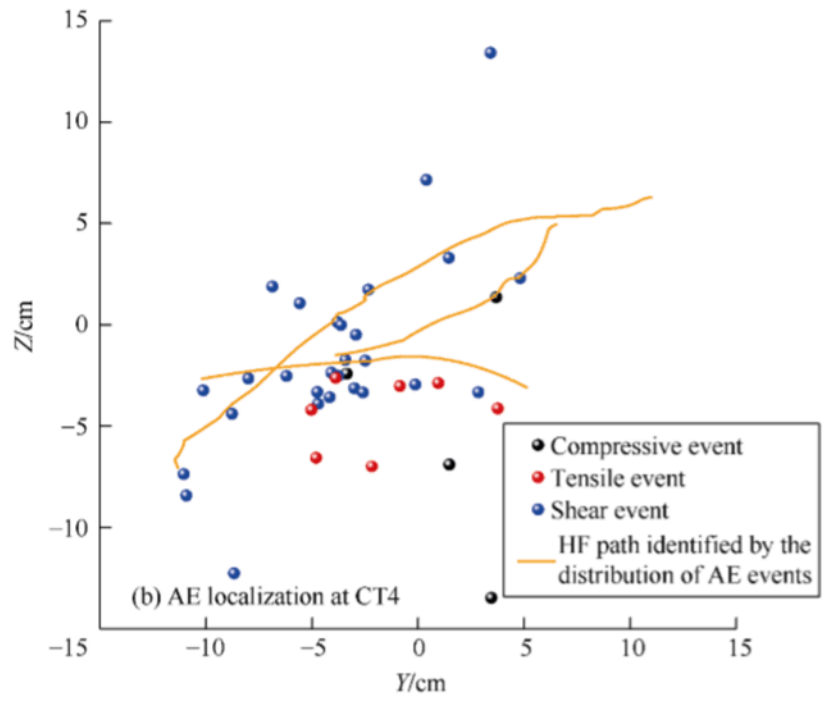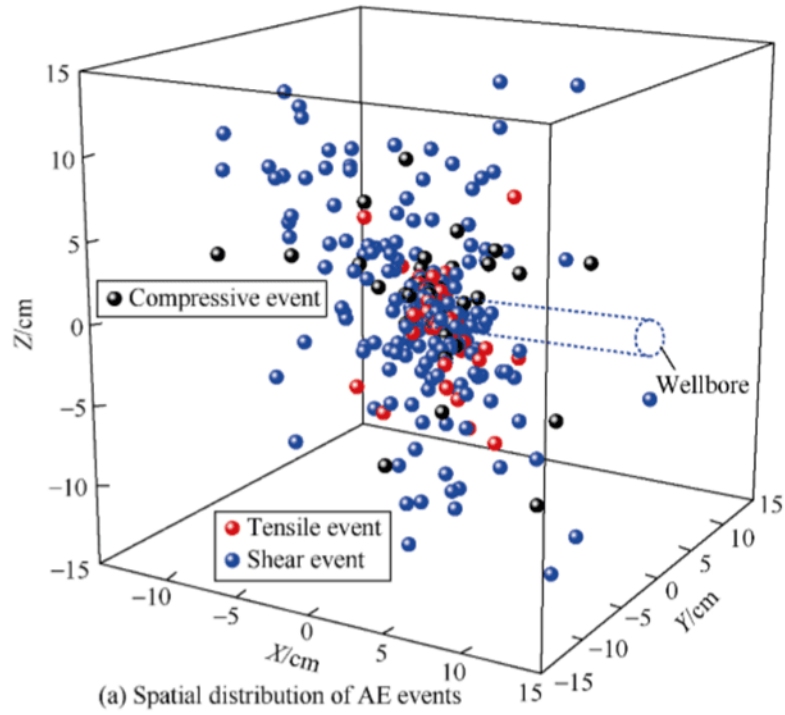
Figure 7: SRV interpretations from AEs.
Fracture connected SRV is distinguished with acoustic signals. Shear event is the major type among all three types captured during injection.
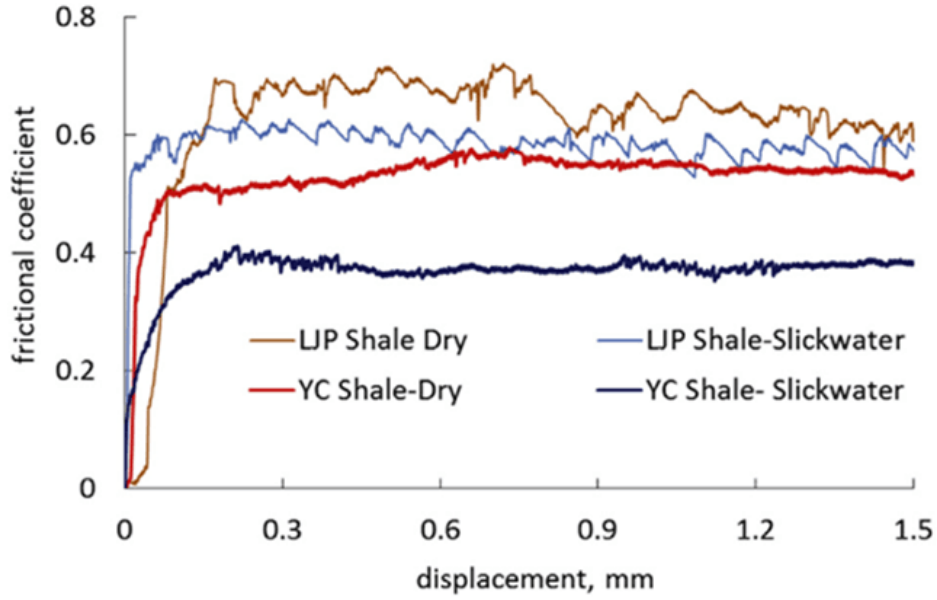
Figure 8:Interfaces of friction coefficient measurement for dry and wet samples[17].
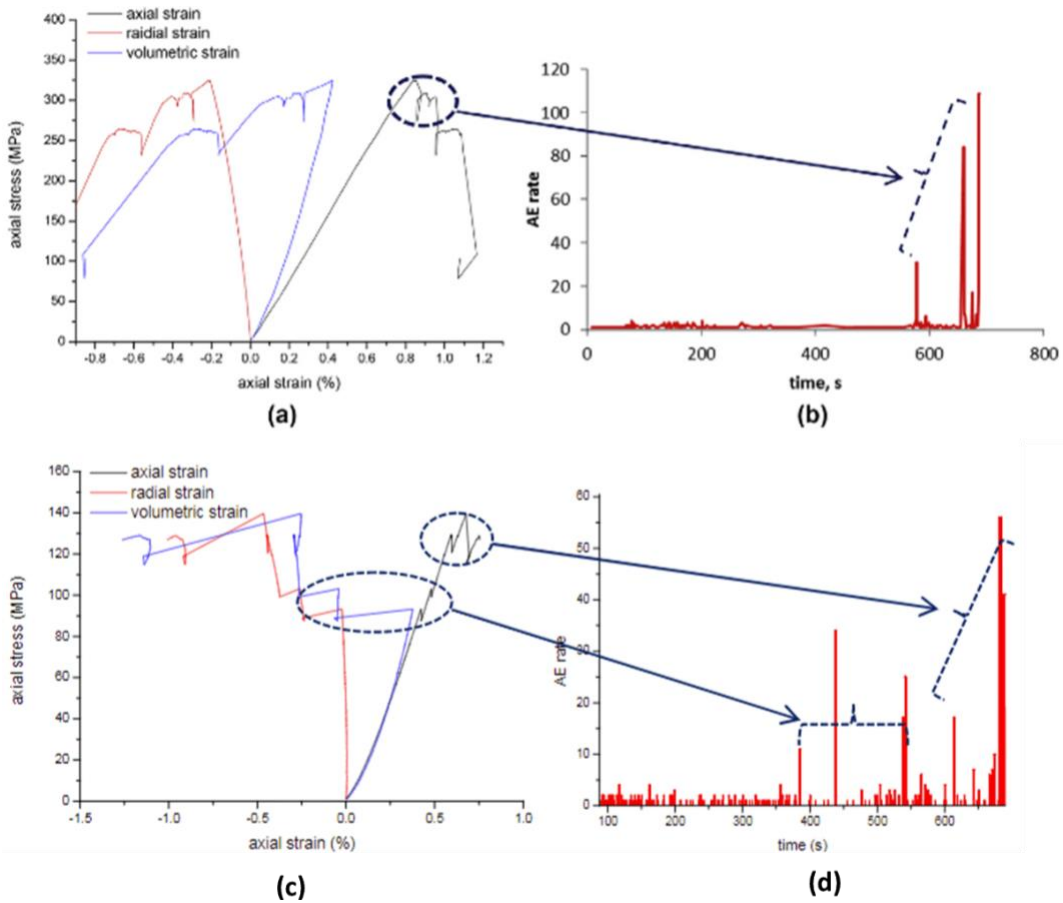
Figure 9: Acoustic emission rates comparison[17].
(a)(b) for dry samples; (c)(d) for the slick water-soaked samples.

14

2.2 Simulation Results for Fractures Interactions

The interaction of hydraulic fracture and pre-existing interfaces had been simulated under various constraints. The intersect condition impacts pressure dissipation along the hydraulic fracture, propagation of fracture tip, and the fracture width. Early studies analyzed and simulated this issue using vertical wells. Dusseault, et al. [18] concluded horizontal shear at lithology interfaces leads to casing deformation for vertical wells. Daneshy [19] brought formation compaction as a cause besides interfaces slippage. Chipperfield, et al. [20] used a mechanical model to illustrate the casing deformation induced by shear expansion of the formation. Furui et al. [21] stated that rock mechanical properties variation during stimulation caused wellbore unstable and displacement in the axial direction.

Warpinski [22] observed from the seismic data that interacting natural faults will change HF propagation orientation and restrict fracture height because the fracturing fluid preferentially transports through higher conductive interfaces, and triggers shear slippage at the interfaces. Maxwell, et al. [23] categorized the shear mechanism into the failure of rock and weak interface slip. Chen, et al. [24] used a coupled 2D model to simulate HF and natural fracture intersection mechanism for different intersecting degrees under confined conditions. They discussed the impact from parameters including in-situ stress, fracture contact friction, intersection angle, as well as fluid injection rate and fluid viscosity. They concluded that a similar injection rate and fluid viscosity resulted in similar intersection patterns. This model was improved by Haddad, et al. [25] in 3D to study Vaca Muerta shale in Argentina. They concluded a positive correlation between the distance of injection point and natural fracture with the casing displacement quantity. Moreover, various leak-off coefficients of vicinity shale beds also lead to different degrees of increase of pore pressure and change stress around interfaces, causing shear-slip. Moradian, et al. [26] calculated

fracture mechanical aperture and found that the aperture is of 2 to 3 times of fracture shear magnitude due to interface unconformity. Daneshy [27] concluded that a lower intersect angle has a higher possibility of arresting hydraulic fracture propagation, and large principal stress difference likely to induce shear sliding of natural fracture. Dahi Taleghani and Olson[28] showed that the stress induced by HF propagation could cause NF tensile debonding and activate fault slip to a large offset distance[29]. Shrivastava and Sharma [30] claimed that in NF rich formation, HF propagation direction was dominated by NF orientation.

Different mathematical models proved that formation shear slippage is one of the major potential risk of casing deformation in the hydraulic fracture stage [10, 31, 32]. [33] stated that interaction angles, fracture friction, and distance to perforation point are parameters that should be analyzed while studying injection-induced shear slip casing deformation. Mapping the fracture network method could help improve fracturing design. Lian, et al. [34] established a 3-D geomechanically model and simulated each stage of hydraulic fracture. Chen, et al. [35] concluded an overlay of seismic signals for more than 61.7% can be interpreted to indicate discontinuous interfaces and deformation points. Thermal loading introduced by the cooling effect of massive hydraulic fracture operations had been studied [36-38]. Some studies showed that cooling effect magnifies casing load, especially the bending stress, and reduces the annular stress. The thermal effect can attenuate casing collapse strength about 19.16 %, thus exacerbate casing resistance through interfacial activation [39]. Low-quality cementation could generate exceeding stress under the eccentric thermal effect. Cement voids can introduce asymmetric pressure and cause the casing to deform under certain temperature conditions [10]. Simulation using casing ovality with layered formation shown that increasing casing wall thickness is more effective than upgrade steal strength [40].

2.3　　Microseismic Interpretation

Maxwell, et al. [41] interpolated the seismic signal from Barnett Shale in Texas with ultra-low permeability (0.0001mD). They generated the growth of the fracture revealed in **Figure 10**. Fracture propagation is highly anisotropic. NE wing is 2.5 to 4.5-fold in length compared with the other three fracture wings. This off-balance fracture propagation would change the fracture failure type from tensile (type I) to shear (type II) [19]. Amirhesari and Tani [42] analyzed the displacement magnitude in vertical and horizontal directions for different types of fault regimes. They claimed that strike-slip and oblique faults had large horizontal offset and normal, reserve fault type had a high vertical displacement (**Figure 11**). The complexity of the mixture existence of normal, reverse, and strike-slip fault regimes in Changning-Weiyuan area would lead to high displacement potential in both vertical and horizontal directions. Overlapping microseismic signals had been used to indicate shear failure, while other kinds categorized as opening failure. Results from the previous lab experiments manifested that less than half of the microseismic signal came from conducted fracture network and fault reactivation due to stress change. Stress reorientation and uneven leak-

off respect toward wellbore also dominate matrix strength and possibly cause extreme stress concentration near wellbore.
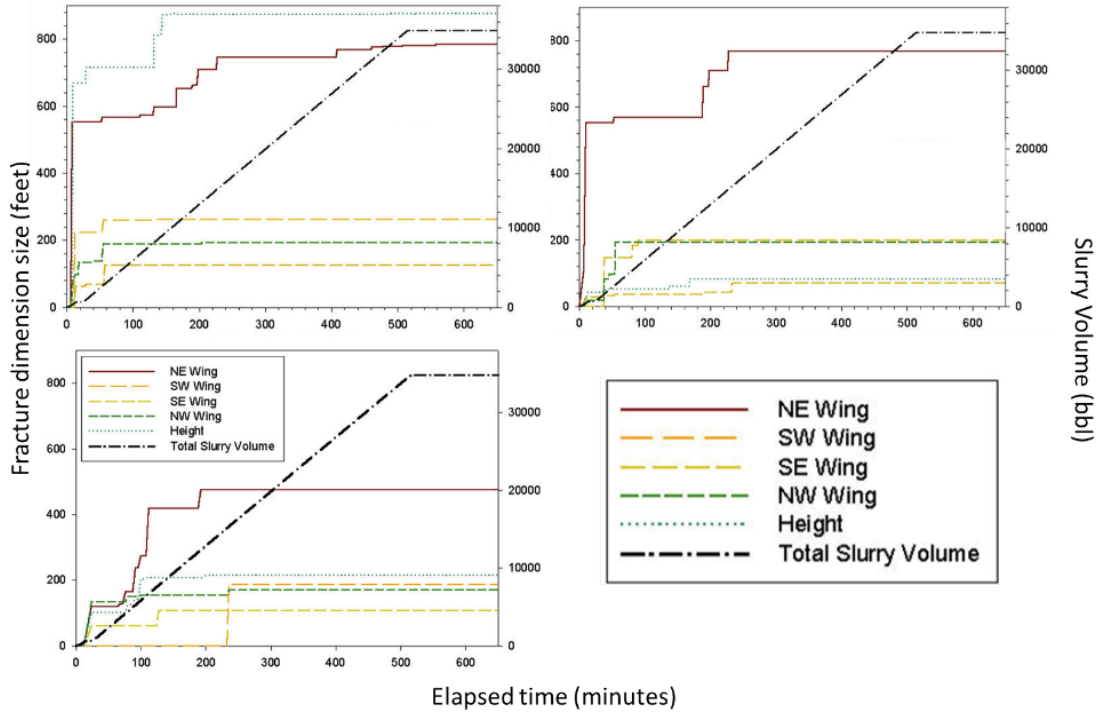
Figure 10: Asymmetric fracture geometry for Barnett shale 41.
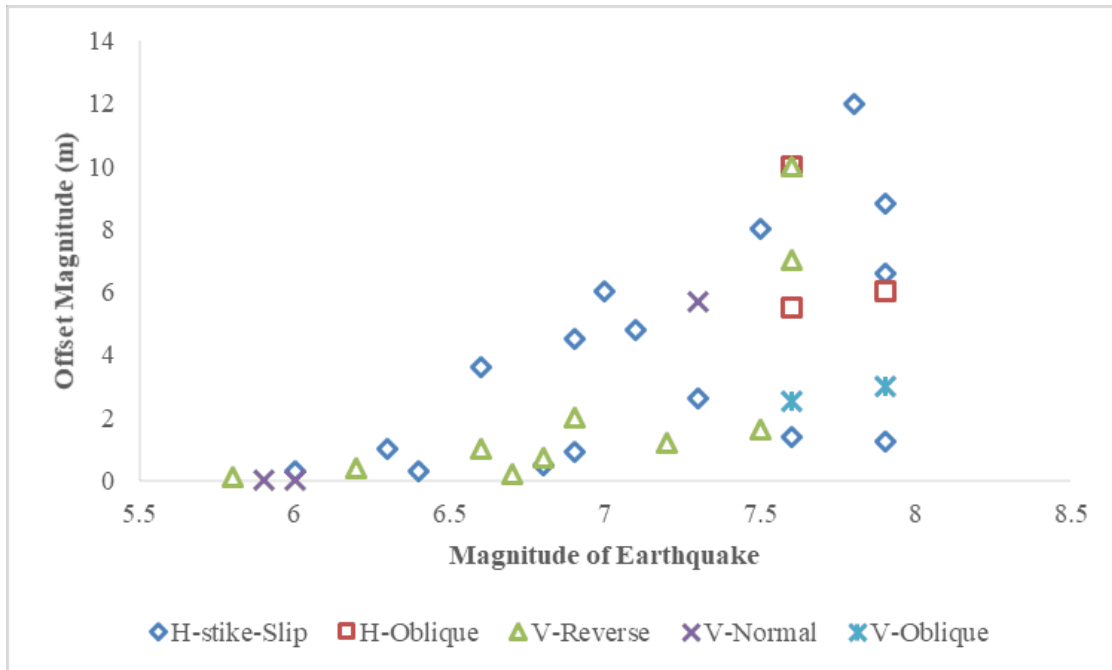
Figure 11: Horizontal displacement and vertical displacement during an earthquake for different fault regime.
Strike-slip type of fault has a larger horizontal displacement compare with oblique faults. Reserve fault types have higher displacement magnitude in the vertical direction. The increase of the vertical displacement also tends to be exponential with earthquake magnitude increases [42].

Chapter 3: Mechanisms and Field Introduction

This chapter talked about mechanisms that govern fracture propagation and available field data. Fracture mechanism governs the HF propagation. Leakoff mechanism governs fluid flow. These two mechanisms determine Stimulated Reservoir Volume (SRV). These mechanisms also alter near-wellbore stress thus must be studied for casing deformation analysis.

3.1   Fracture Mechanisms

Fracture propagation dominated by matrix mechanical properties and impacted by sedimentary conditions and mineral composition. Rock strength increases with the increase of effective confinement stress [43]. Although rock matrix strength varying in several magnitudes, the internal friction coefficient is between 0.5 to 2.0 with a median of 1.2 [44]. Shale owns a low internal friction coefficient thus draws in **Figure 12** for 0.7, 1, and 1.2. The friction at fracture surface provides resistance during slippage after fault reactivation. This can be explained by Mohr Coulomb's criteria in **Eq. 1**. Mohr-Coulomb criteria summarized this correlation as shear tensile strength equals the summation of rock cohesion and a fraction of effective normal stress at interfaces. τ is the frictional strength, S is the cohesion of matrix, μ_i is the internal friction coefficient, $\boldsymbol{\sigma_n}$ ($\boldsymbol{\sigma'}$) is the effective stress calculate using **Eq. 2**, where α is the biot coefficient from 0 to 1, P_w is pore pressure [45].

$$\tau = S_0 + \mu_i \, \sigma_n \qquad\qquad \text{Eq. 1}$$

$$\sigma' = \sigma - \alpha \, p_w \qquad\qquad \text{Eq. 2}$$
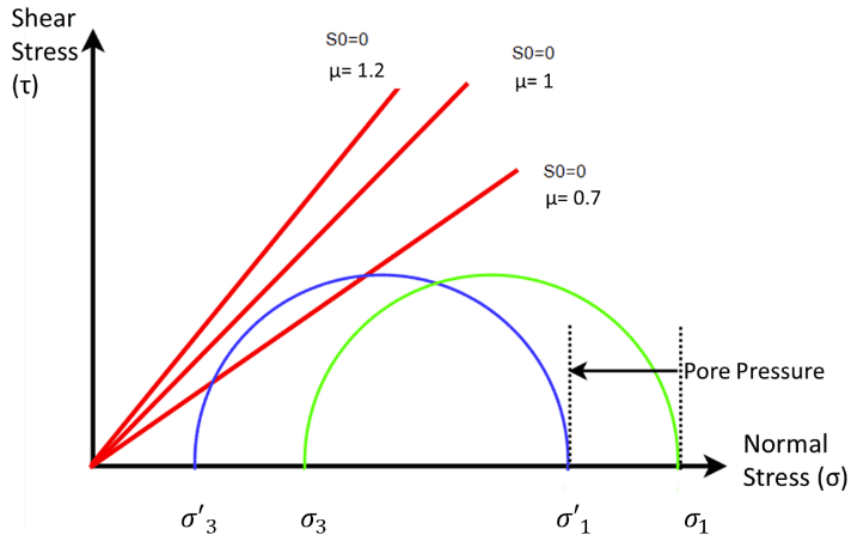
Figure 12: Mohr Columbo shear slippage criteria schematic.
Increase of pore pressure reducing effective stress acting upon matrixes. The initial friction coefficient of the rock matrix governs the failure envelope and would reduce rock strength. Where the green circle is original MC circle defines shear and normal stress of any plane in the matrix. Increase of the pore pressure shifts effective stress toward left (blue MC circle)

Intersection properties impact nature fracture failure mode and dominate displacement direction and magnitude at interfaces [24]. Renshaw and Pollard [46] provided a criterion which was broadly referred for perpendicular fracture intersecting shown as **Eq.3**.

$$-\frac{\sigma'_{xx}}{T_0 - \sigma'_{xx}} > \frac{0.35 + \frac{0.35}{\mu}}{1.06} \qquad \text{Eq. 3}$$

Parameters that govern penetration behavior are far-field stress, fracture tensile strength, and fracture friction. This empirical criterion stated the compression stress required for the fracture to penetrate the perpendicular unconformity interfaces. Gu and Weng [47] expand Renshaw & Pollard criterion with interfacial cohesion in **Eq.4**.

$$\frac{\frac{S_0}{\mu} - \sigma_H}{T_0 - \sigma_h} > \frac{0.35 + \frac{0.35}{\mu}}{1.06} \qquad \text{Eq. 4}$$

S_o is cohesion at the interface, t_o is shear strength, and μ represents the interface friction coefficient. The rock matrix shear strength margin that likely to introduce slippage is derived in **Eq. 5.**

$$T_0 > \frac{\frac{\left(0.35 + \frac{0.35}{\mu}\right)\sigma_h}{1.06} + \frac{S_0}{\mu} - \sigma_H}{\frac{0.35 + \frac{0.35}{\mu}}{1.06}} \qquad \text{Eq. 5}$$

The rock strength range with different interfaces frictions and stress ratios are plotted from **Figure 13**. The maximum and minimum values are plotted in **Figure 14**. Shear strength of the connected interface below the plotted line indicating a probability of slippage. Moreover. increase of pore pressure decreases stress ratio. The existence of cohesion at interfaces increases the slipping probabilities while reducing penetration possibilities. Gu and Weng [47] summarized higher stress difference (S_H/S_h) and lower intersection angle (β) tends to change fracture propagation from the cross to slipping and alter its direction along a natural fracture (**Figure 15**).

Slippage Criteria

Slippage Criteria (Cohesion=5MPa)

Slippage Criteria (Cohesion=10MPa)
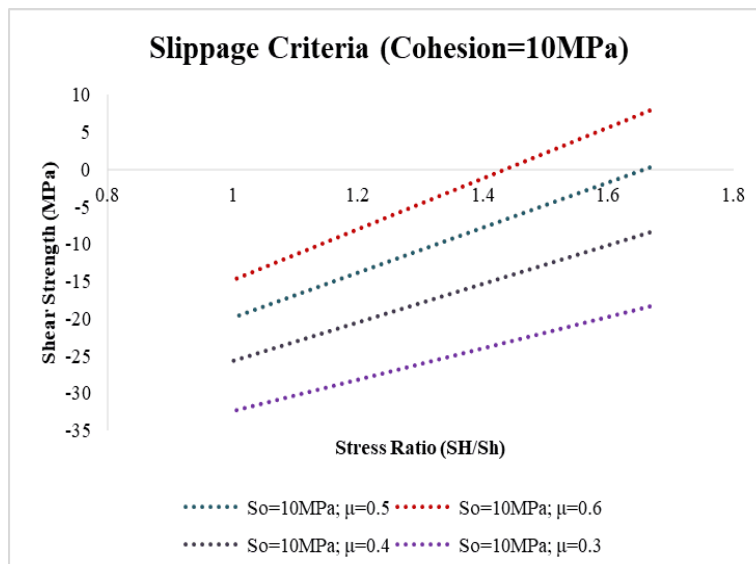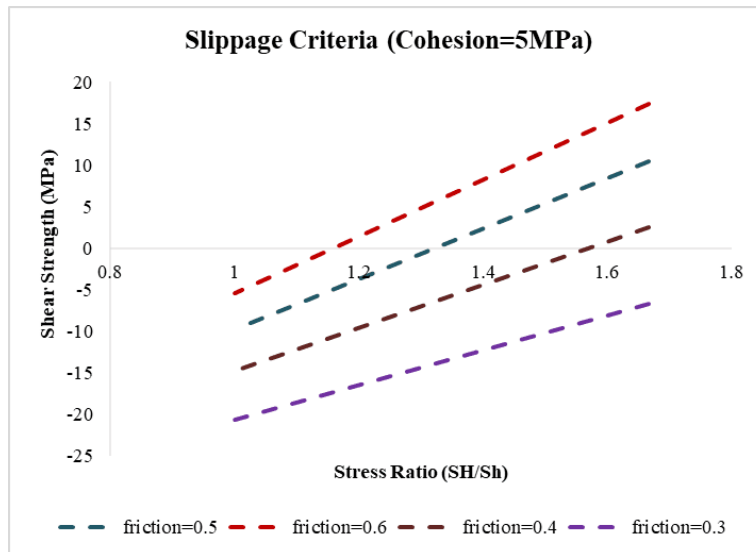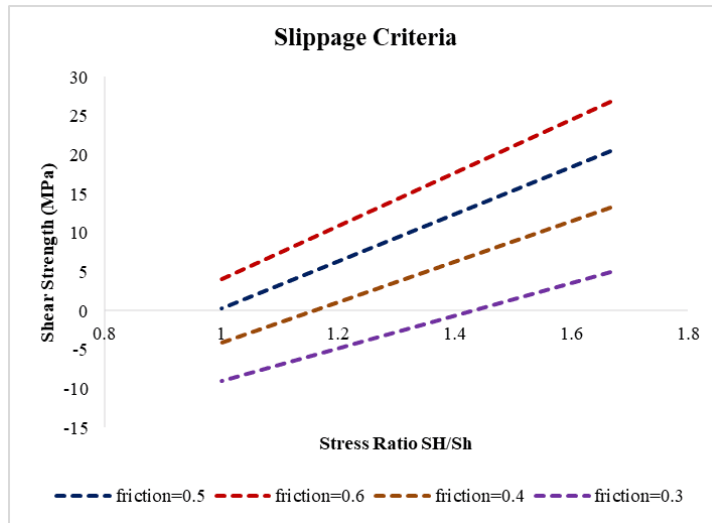
Figure 13: Possible induce slippage at interfaces.
Calculated with 10 MPa cohesion, with the friction coefficient at values using 0.3, 0.4, 0.5, and 0.6.
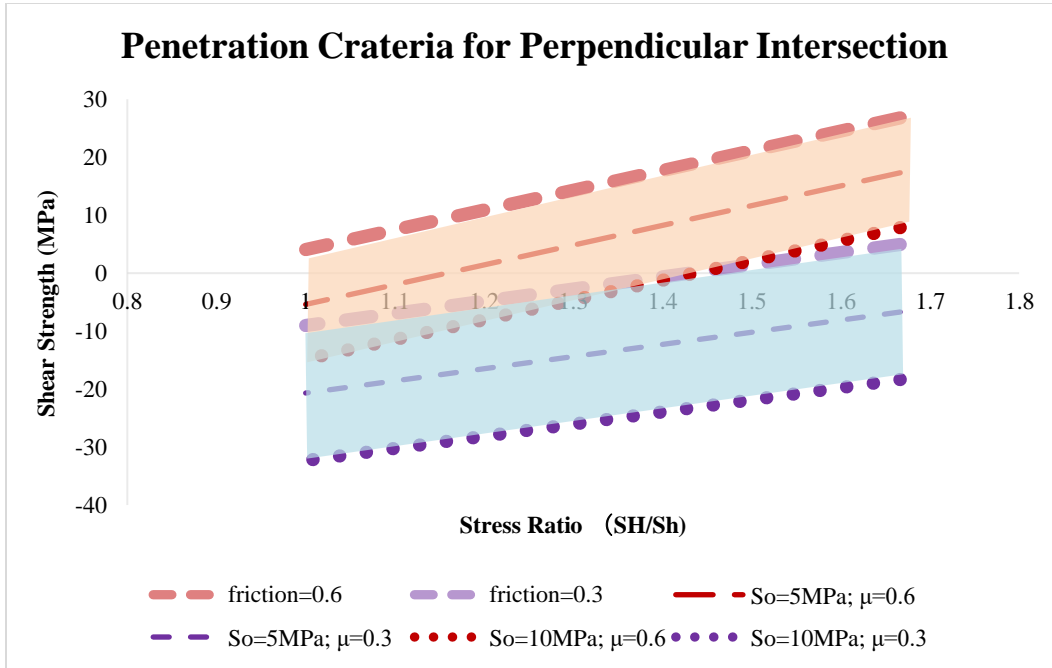
Figure 14: Shear strength impacts upon slippage initiation.
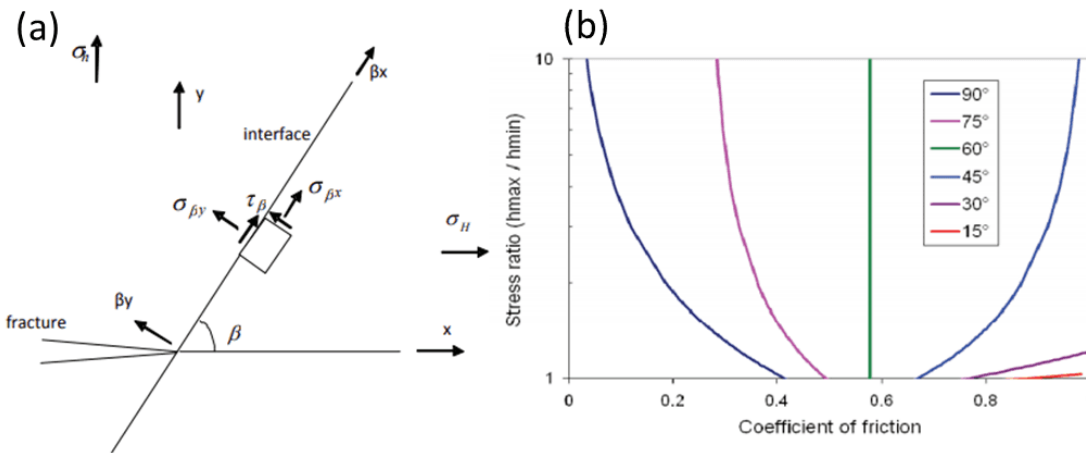
Figure 15: Intersection angles and slippage [48].
(a) schematic of hydraulic fracture approaching natural fracture with an angle β. (b) with angle β using values of 15, 30, 45, 60, 75, 90 degrees.

Wu and Olson [49] derived an explicit solution from Renshaw and pollard criteria with a linear elastic fracture mechanism for intersection angle β equals 90 degrees.

Sarmadivaleh and Rasouli [48] modified Renshaw and pollard, derived the crossing criteria as a function of shear strength to maximum horizontal stress ratio. A higher ratio leads to a higher crossing possibility and contribution of friction drop.

$$\frac{\frac{S_0}{\mu} + S_{Hmax}}{T_0 + S_{hmin}} > \frac{(K_I - 3K_{II}) + \frac{|-K_I + K_{II}|}{\mu}}{3K_I - K_{II}}$$

Eq. 6

The reactivation of closed interfaces assumed as mixing failure of type 1 and type 2 fracture modes [50]. Benzeggagh and Keane (BK) model of fracture breaking is a fundamental theory in the fracture break process.

$$G_{TC} = G_{IC} + (G_{IIC} - G_{IC})(\frac{G_{II}}{G_T})^m$$

Eq. 7

Where mode 1 is opening fracture and mode 2 is a shear fracture, and power m indicating the portion of shear failure energy release rate (G_{II}) towards total energy release rate (G_T), Parameter m use value 2 for brittle and 3 for ductile. the strain energy released is summarized as a function of crack length and mode 2 ratios. The results of the original BK studies summarized that the higher mode 2 fracture percentage (shear failure) lead to a larger energy release rate. Fracture strength, and energy release rate govern the fracture propagation during stimulation. These parameters usually tested and measured from the experiment [51], and highly dependent on the material properties, geometric condition, and loading environment, which is likely to vary in a large range.

Fracture toughness (stress intensity factor) is used to estimate fracture energy release rate G using **Eq. 8** and **Eq. 9**. Where G_I is an energy release rate for fracture mode 1 opening

mechanism and G_{II} for shear mode fracture energy release rate [52, 53]. Fracture toughness (K) is scale related and impacted by reservoir geometry, with the unit in Pa·$\sqrt{m}$. Fracture energy release rate in our simulation use fracture toughness that measured from Longmaxi formation [54]. Open and shear fracture toughness in the range of 0.75 to 0.92 MPa·$\sqrt{m}$ and 0.92 to 1.13 MPa·$\sqrt{m}$ respectively. **Figure 16** shows the statistical study of the fracture toughness data measured from Longmaxi formation and the normality test gave p-values of 0.1 and 0.8 separately assume both parameters in a normal distribution. Through bootstrap using R with parameter from **Table 2**. The Poisson's ratio varies in a range from 0.16 to 0.25, Young's modulus from 25 GPa to 59 GPa. Assumed normal distribution for fracture toughness and uniform distribution for other parameters. The highest frequency fracture energy release rate shown in **Figure 17** is in the range of 10-30 (KPa·m) with a lognormal distribution from Monte Carlo simulation.

$$G_I^C = K_{IC}^2(1 - \nu^2)/E \qquad\qquad \text{Eq. 8}$$

$$G_{II}^C = K_{IIC}^2(1 - \nu^2)/E \qquad\qquad \text{Eq. 9}$$

Table 2: Energy release rate Monte Carlo simulation with parameters and each distribution

Parameters	Distribution	Unit	Mean	Standard deviation	Min	Max
K1	Normal	MPa$\sqrt{m}$	0.8	0.071	-	-
K2	Normal	MPa$\sqrt{m}$	0.96	0.9	-	-
Poisson's ratio	Uniform	-	-	-	0.16	0.25
Young's Modulus	Uniform	GPa	-	-	25	59
m	Uniform	-	-	-	2	3
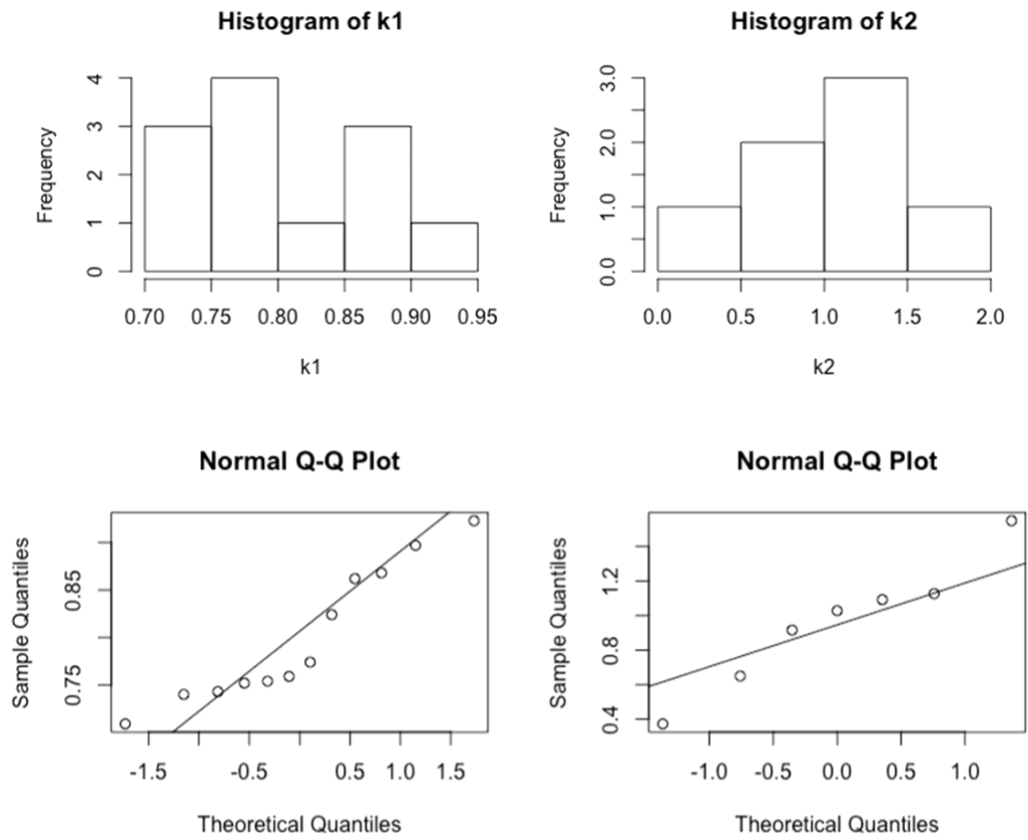
Figure 16: Histogram of fracture stiffness for type I (k1) and type II (k2).
Q-Q plots indicating it is reasonable to assume the distributions of k1 and k2 are normal
distributions for Longmaxi shale gas play

Histogram of Energy Release Rate
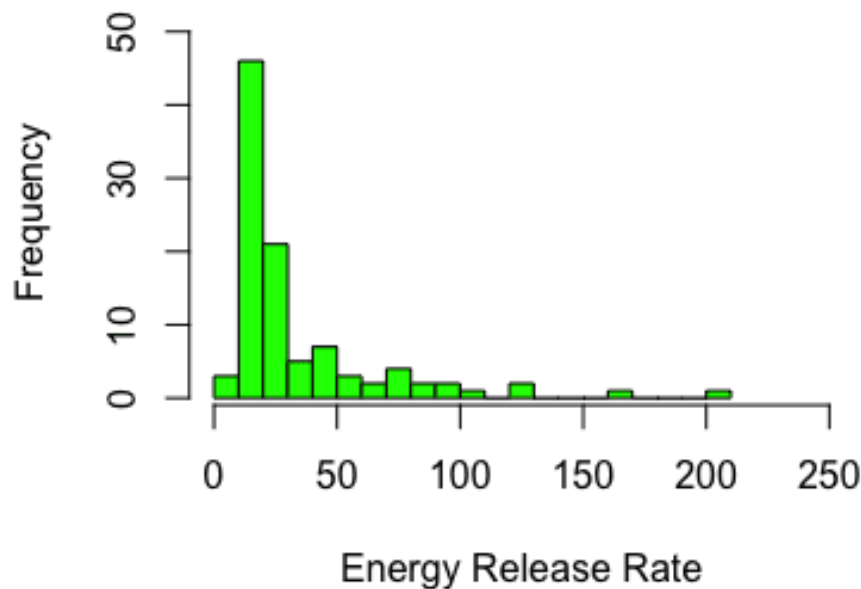
Figure 17: Monte Carlo simulations using parameters in Table 2.
The fracture energy release rate has a log-normal distribution. Highest possibility (over 60 %) drops in 10 to 30 KPa·m, the possibility is smaller for the energy release rate to have a value from 30 to 60 KPa·m, the highest energy release rate value can be up to over 200 MPa/ m^2.

The fracture mechanism contributes to the hydraulic fracture propagation process. Increases of fracture aperture with interfaces slipping and fracture dilation during hydraulic fracture might dominate fracture performance as well. The fracture gap distance default set at 0.002 (dimensionless) in Abaqus. Considering the unconformity of fracture surfaces, slippage along interface increases its aperture and thus enhances the conductivity further. By calculating the average of surface apertures for various ranges of slippage, Moradian, et al. [26] proposed the dilation governs fracture surface behavior during slippage and the aperture of fractures increases double as the slippage occurs. 1mm displacement increase aperture to 2mm, where 6-10 mm displacement leads to fracture average aperture reaches 3.5 mm. The large fracture opening can adjust fluid flow

28

in fracture networks. The additional fracture mechanical aperture decreases fluid flow velocity and pressure gradient in the fracture geometry.

3.2 Leak-off Mechanism

Tangential fluid flow and normal fluid flow are two types of fluid flow within fractures, fluid flow in the direction along fracture surface and normal toward the formation respectively shown in **Figure 18.** Tangential fluid flow in the fracture is assumed as Newtonian flow shown as **Figure 19** (**Eq. 10**), in which it is incompressible, single-phase, steady-state, and governed continuity equation of Reynold's lubrication theory shown in **Eq. 11**. Fluid injection efficient was as low to 4 % and 2 % for both simulated lateral and radial fractures [55]. Normal flow (tangential flow) velocity and flow rate towards the top and bottom layer are governed by **Eq. 13** and **Eq. 14** respectively. The analytical solution of fracture flow is derived in **Eq. 15**.

$$q = \frac{d^2}{12\mu} \nabla p \qquad \text{Eq. 10}$$

Where **q** is the volume flow rate in cohesive element, dimensionless, d is the separation displacement of the cohesive element in m, μ is the viscosity and ∇p is the tangential pressure gradient of injected fluid in mPa·s and MPa/m respectively

$$g + \frac{\partial q_f}{\partial s} + v_T + v_B = 0 \qquad \text{Eq. 11}$$

$$q_f = -\frac{g^3}{12\mu_f} \frac{\partial p_f}{\partial s} \qquad \text{Eq. 12}$$

$$v_T = c_T(p_f - p_T); \ v_B = c_B(p_f - p_B) \qquad \text{Eq. 13}$$

$$q_t = c_t(p_i - p_t); \ q_b = c_b(p_i - p_b) \qquad \text{Eq. 14}$$

$$g + c_T\left(p_f - p_T\right) + c_B\left(p_f - p_B\right) = \frac{\partial}{\partial s}\left(\frac{g^3}{12\mu_f}\frac{\partial p_f}{\partial s}\right)$$

<div align="right">Eq. 15</div>

Where **q** is flow rate in m³/s, **c** is the leak-off coefficient at interfaces in m/s0.5, and p is pressure

in MPa. Subscribe t for direction towards upper cohesive elements, b for flowing direction toward

the bottom layer, subscribe i represent the middle point.
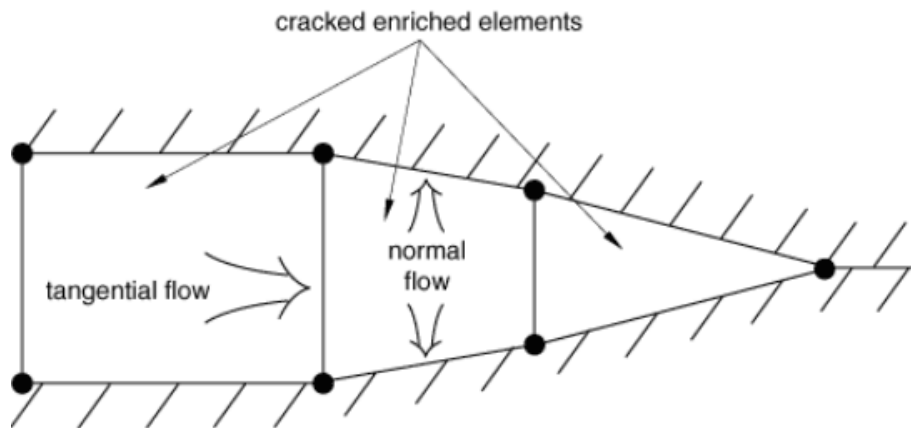
Figure 18: Fluid flow in the crack element [57].
Tangential flow along the crack and normal flow penetrating crack wall perpendicularly
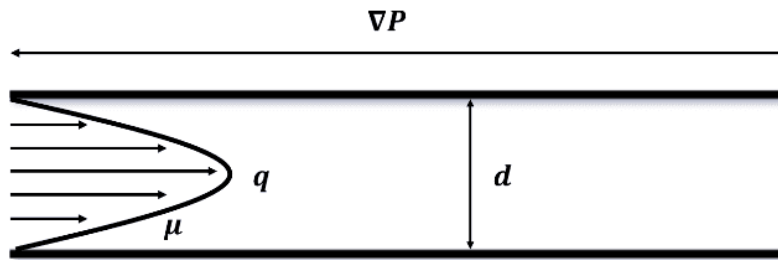
Figure 19: Newtonian Flow regime schematic for tangential flow in the crack.

Many methods can be used to quantify the leak-off coefficient which controls the efficiency

of hydraulic fracture and determines the dimension of the induced fracture [58]. Asymmetric HF

geometry respect to wellbore was verified asymmetric through seismic signals. This asymmetry results in unbalanced fluid leak-off and spurt loss (**Figure 20**) on different HF wings.
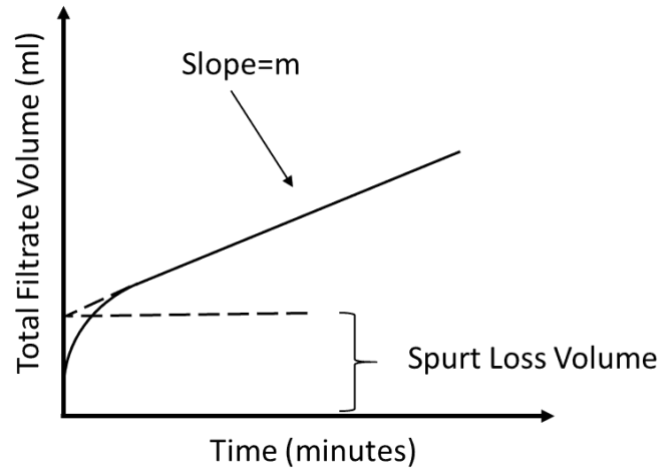
Figure 20: Spurt Loss before filter cake build-up with hydraulic fluid injected.

Opening or dilation of weakly bonded interfaces provides additional flow path. Opening interfaces with a higher conductivity can arrest the HF propagation thus decrease hydraulic fracture efficiency (SRV). Furthermore, fluid flow through interfaces decreases friction coefficient and reduces resistance during fault slippage.

The injected fluid is either stored in the propagated fractures or leaks off into matrices. Access of near fracture storage such as layer interfaces and faults results in pressure drop around the fracture tip. The pressure dissipation rate is impacted by leak-off and permeability. Confined pressure around contact surfaces also affects mechanical properties including Young's modulus, tensile strength, and Poison's ratio. A higher loss ratio leads to leak-off-dominated fracture propagation. As the fluid leak-off measured from the lab has a shape in **Figure 20**. Leak-off model (**Eq. 19** to **Eq. 21**) can be much more complex summed by a wall-building coefficient (C_w) in filter-cake zone, viscosity controlled coefficient (C_v) in invade zone, and compressibility controlled coefficient (C_c) in the reservoir zone [59]. However, Longmaxi case with extreme low

permeability. Also, most of the parameters in these equations are not available and varying in a great range. There are simulations concluded that intersecting of hydraulic fracture and natural fracture result fluid leak-off coefficient in three times compare with formation without fractures [60]. Leak-off volume increase due to the additional spurt loss. For the fissure system, this volume continuously increases with conducting to NF network. Considering the scenarios of fracture propagation and fracture-tip screen out processes. The leak-off type is reservoir dominated for low permeability oil reservoir with a permeability less than 5 mD, and gas reservoir with a permeability lower than 0.1mD [61]

$$V_L = 2C_W\sqrt{t} + S_p \qquad \text{Eq. 16}$$

The leak-off volume is V_L, t is the leakoff time, and S_p stands for spurt loss.

$$\eta = 1 - \frac{V_L}{V_I} = \frac{1}{1 + 2C_L\sqrt{2t}/\overline{w}} \qquad \text{Eq. 17}$$

The efficiency of hydraulic fracture (η) is fracturing fluid volume in the created fractures over total injected volume (V_I). With the fracture face area (A_f) can be determined as follows.

$$A_f = \frac{q_i t}{\overline{w} + 2C_L\sqrt{2t}} \qquad \text{Eq. 18}$$

q_i is the injection rate, $\overline{w}$ is the fracture width, and C_L is the leakoff coefficient.

$$C_w = \sqrt{\frac{k_{cake}\alpha\Delta p_{cake}}{V_L}} \qquad \text{Eq. 19}$$

wall-building coefficient (C_w), k_{cake} is the wall filter cake permeability, Δp_{cake} being the pressure drop across the filter cake, V_L is the leakoff volume.

$$C_v = \sqrt{\frac{k_{fil}\varphi\Delta P}{2\mu_{fil}}} \qquad \text{Eq. 20}$$

Viscosity controlled coefficient C_v dominated the invaded zone. k_{fil} is the relative permeability for filtrate to flow in the invaded zone, μ_{fil} is the viscosity of the filtrate, φ is the porosity.

$$C_c = \sqrt{\frac{k_r c_t \varphi}{\pi \mu_r}} \Delta P_c \qquad \text{Eq. 21}$$

Compressibility controlled coefficient (C_c) in the reservoir zone, the pressure drop between the filtrate reservoir and far-field reservoir is ΔP_c, c_t is the constant total compressibility, k_r is the reservoir matrix permeability and μ_r is the reservoir fluid viscosity. while using a high carter's leak-off coefficient, (0.00015m/s0.5).

3.3 Discussions upon Longmaxi Formation

Figure 21 depicts highly fractured wellbore, with lateral bedding planes and drilling-induced fractures in the near-wellbore region. Stress reorientation is detected by breakout rotation for Wei-202 well. These phenomena reveal the complex and highly anisotropic stress condition near the wellbore. Poisson's ratio, pore pressure, and vertical stress are stable whereas Young's Modulus and horizontal stresses (σ_H and σ_h) vary at different layers. As at 2400 m, all three parameters drop consistently (**Figure 22**). Large structural features such as fault may dominate reservoir stimulation effects [62]. As shown in **Figure 23**, the fault has been activated more than 6 stages. The intersecting angle of natural fracture (NF) and hydraulic fracture (HF) ranges from 20 to 70 degrees. The connection of NF and HF will not only cause interface displacement but also lead to low fracturing efficiency due to additional leak-off volume. If a fracture or fissure has been activated, it would be much easier to be reactivated by following fracture stages.

Figure 24 depicted a reactivation of the same geological features from adjacent stimulation stages., **Figure 25** is a side view of all stimulation stages showed an increase signal magnitude in later stimulation stages compare to former stimulation stages. **Figure 26** is a top

view of all stimulation stages from dataset. The anisotropic fracture propagation is clear from this figure. Seismic signals are largely dispersed on the northwest side of the wellbore and densely distributed on the southeast side of the wellbore. Although the view of microseismic signals can be biased since it is interpreting 3D with a 2D map. **Figure 27** is an experiment measuring Longmaxi compressive strength, this parameter is later applied as mechanical properties the injection model.
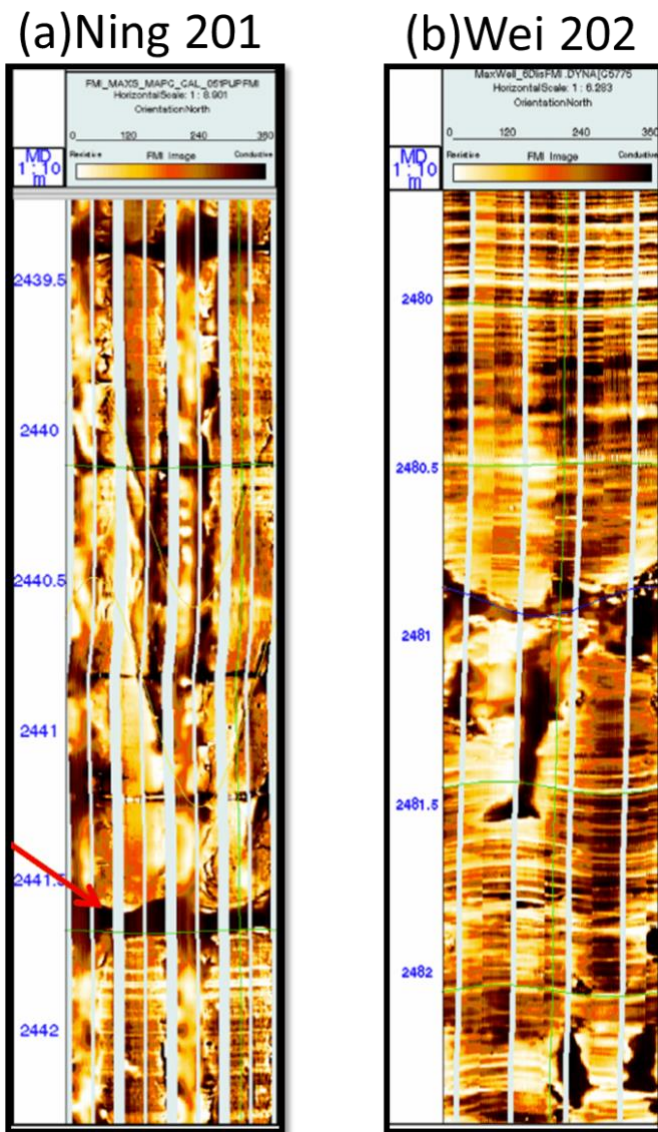
Figure 21: Full Waveform Invasion images for Ning201 and Wei 202 wells.

(a) There is a sedimentary bedding interface at depth 2441m labeled with a red arrow. Smaller scaled lateral gaps in 2440.2 m, 2440.8 m, and 2441.2 m usually interpreted as drilling-induced fractures near the wellbore.
(b) the wave formed pattern indicating laminated shale sequence and the sin like wave due dip angle of sedimentation. Compare the breakout shadow in 2481m to 2481.5 m with the breakout shadow from 2482m, the breakout rotation is clear to be observed. This also indicates a complex stress condition around the wellbore.
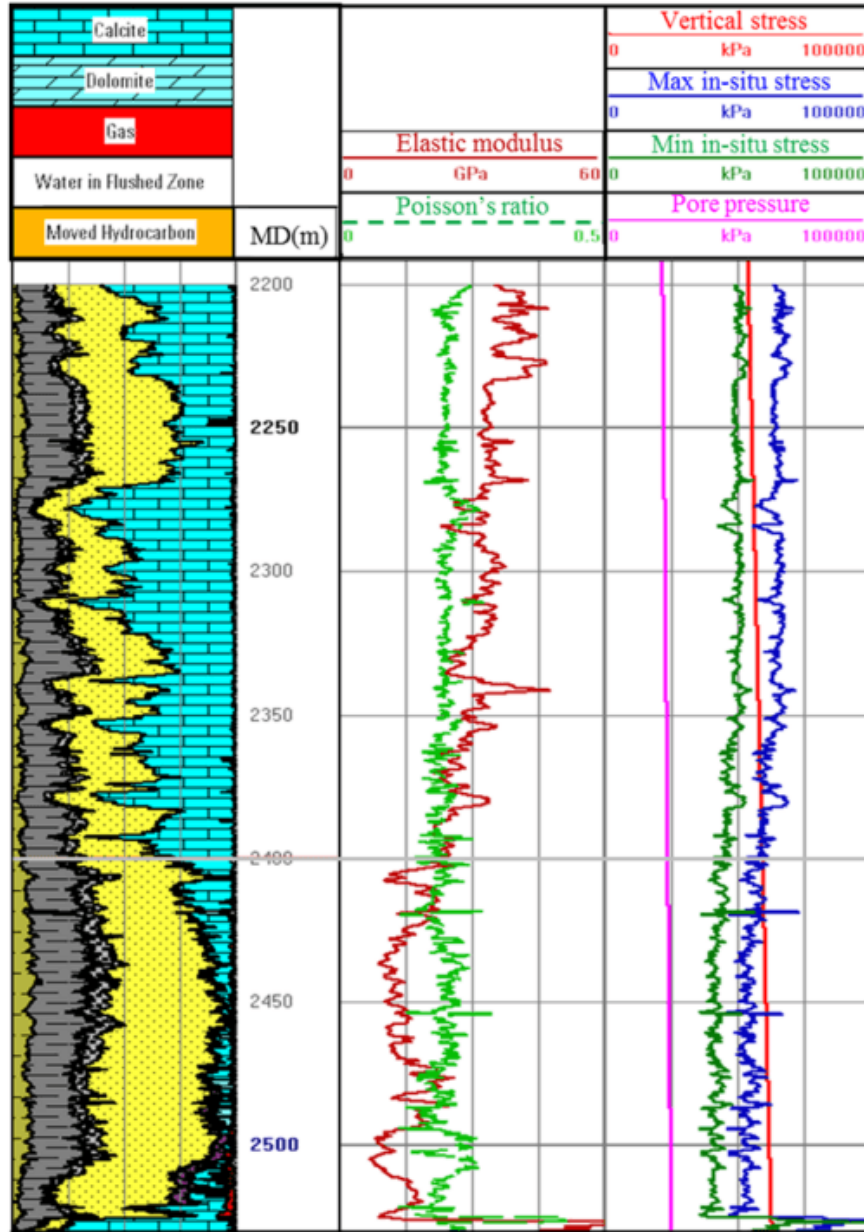
Figure 22: Rock mechanical properties for W201 well from measured depth 2200 m to 2500m.
Young's Modulus drops gradually from 2200m for 40 GPa to 2400m for 25 GPa and maintain a lower magnitude from 2400m to 2550 m at a value of around 15 GPa. Pore pressure along this lateral is stable with a value around 25MPa 40
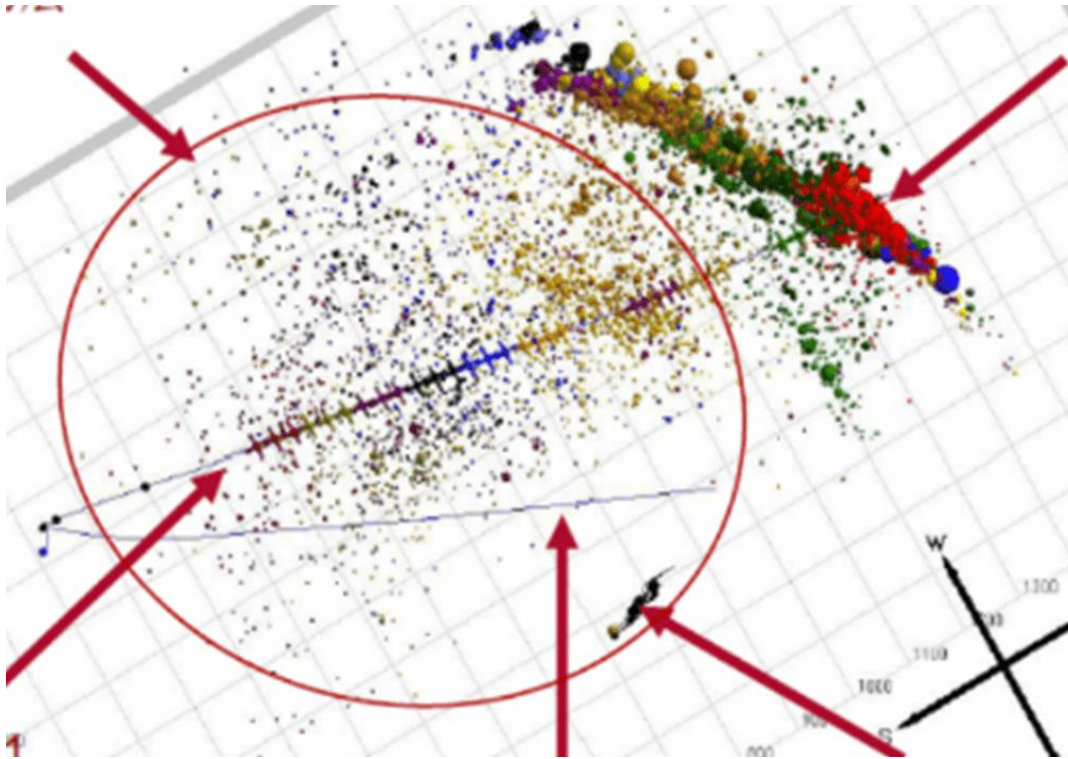
Figure 23: Natural fracture activated with multiple hydraulic fracture stages.
The large fracture intersects with wellbore is clear from microseismic signals as it is activated almost for every fracture stage repeatedly. The length of this fracture from the map is about the same compared with the entire horizontal lateral for the well. The intersect angle from this view is about 45 to 60 degrees estimated from the map. From the natural fracture trigger signals, it also revealed that each stage will activate natural fractures in different sections, the direct intersection point is the most significant point where it directly causes displacement. Stages away from intersection points are less likely to impact the casing-fault displacement as the triggered location is relatively far from the intersection point. It is also clear that the magnitude of the signal from fault is apparently greater than other hydraulic fracture signals scattered on the map.
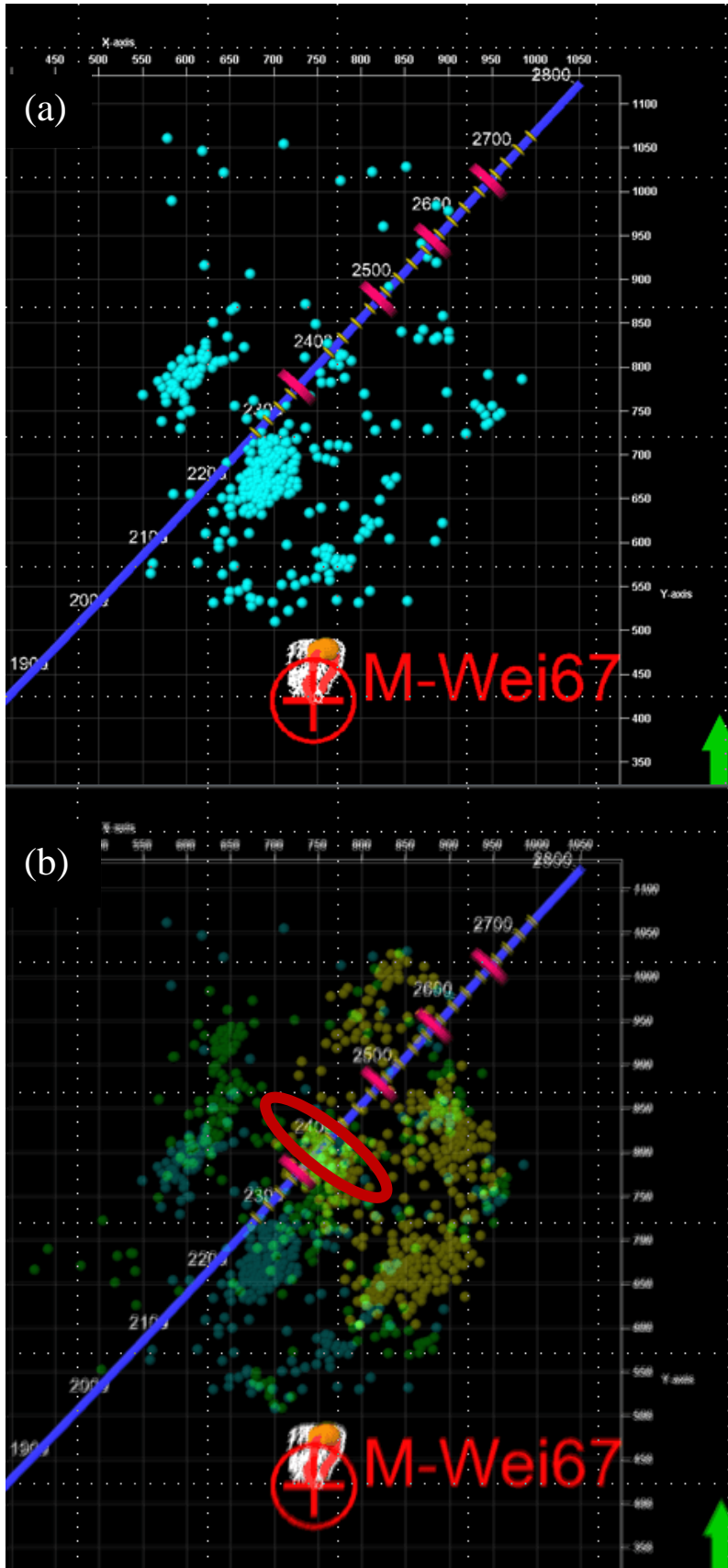
Figure 24: Wei-201 horizontal well hydraulic fracture microseismic signals.

(a)stage 5; and (b) overlapping stages 3, 4, and 5. Overlapped signals circled in red are highly possible emitted from original fissure networks. At measured depth around 2403m, it is observed that signals are reactivated for all three stages across the wellbore. Highly repeated reactivation of the same fracture, and the potential of certain fracture passing across the wellbore. The potential
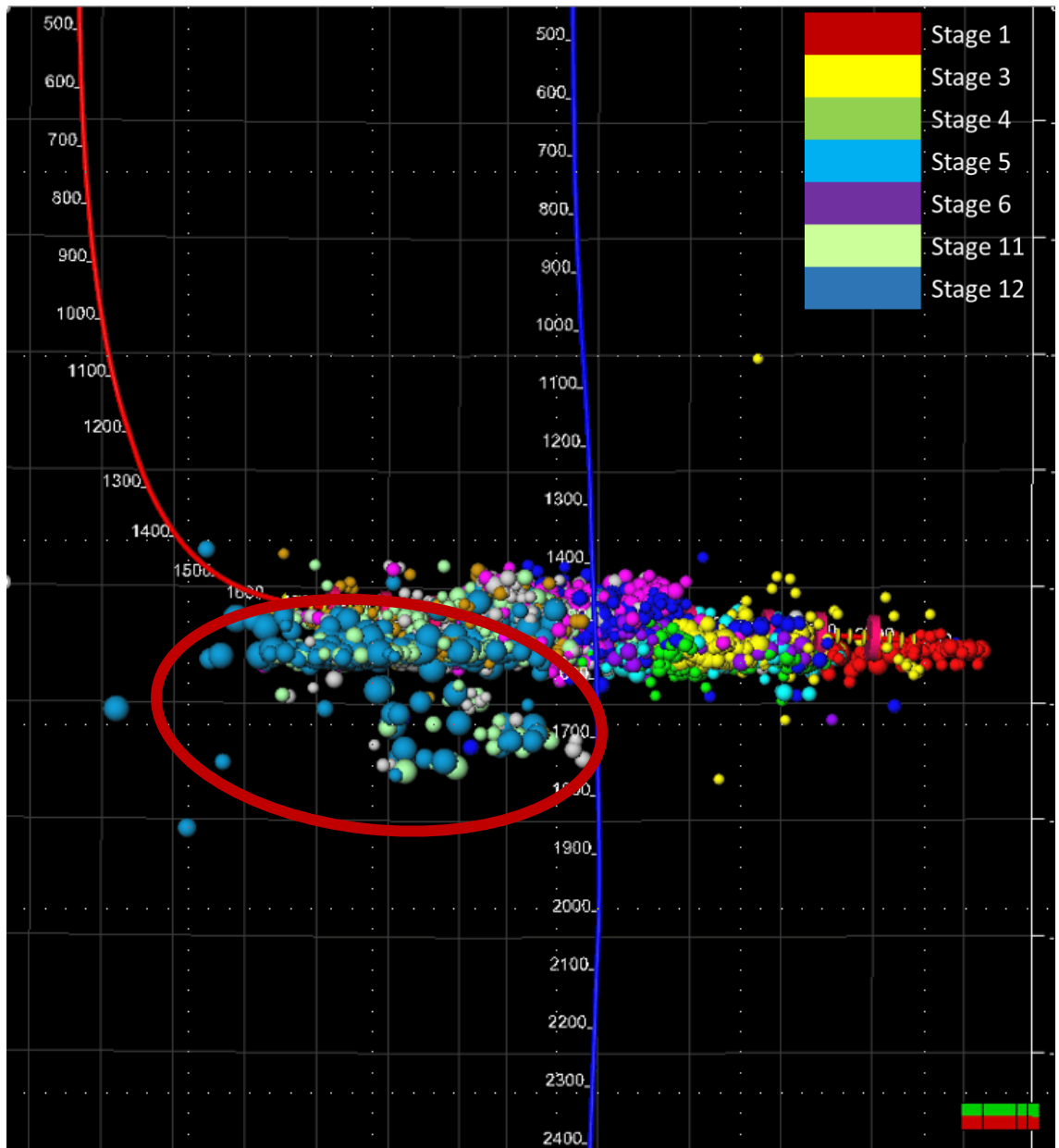
Figure 25: Side view of microseismic signals for fracture stages 1 to 12.
The size of the signal represents the magnitude of the recorded microseismic event. Stage 12 has the largest magnitude compare with any other stages. This could indicate the activation of a natural fracture or unconformity surface.
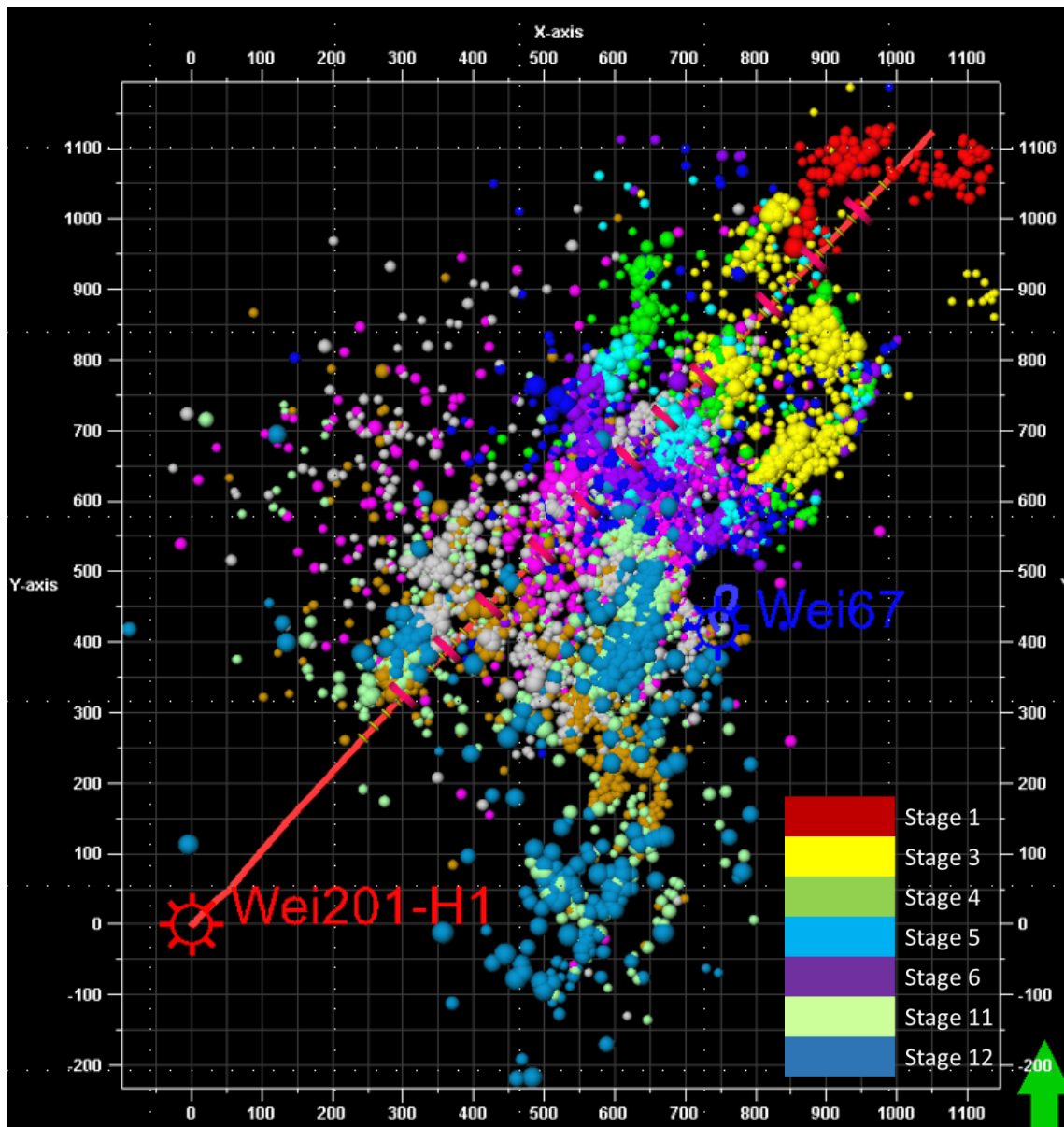
**Figure 26: Microseismic signals map for wei201-H1.
Asymmetrical distribution is obvious from this map.**
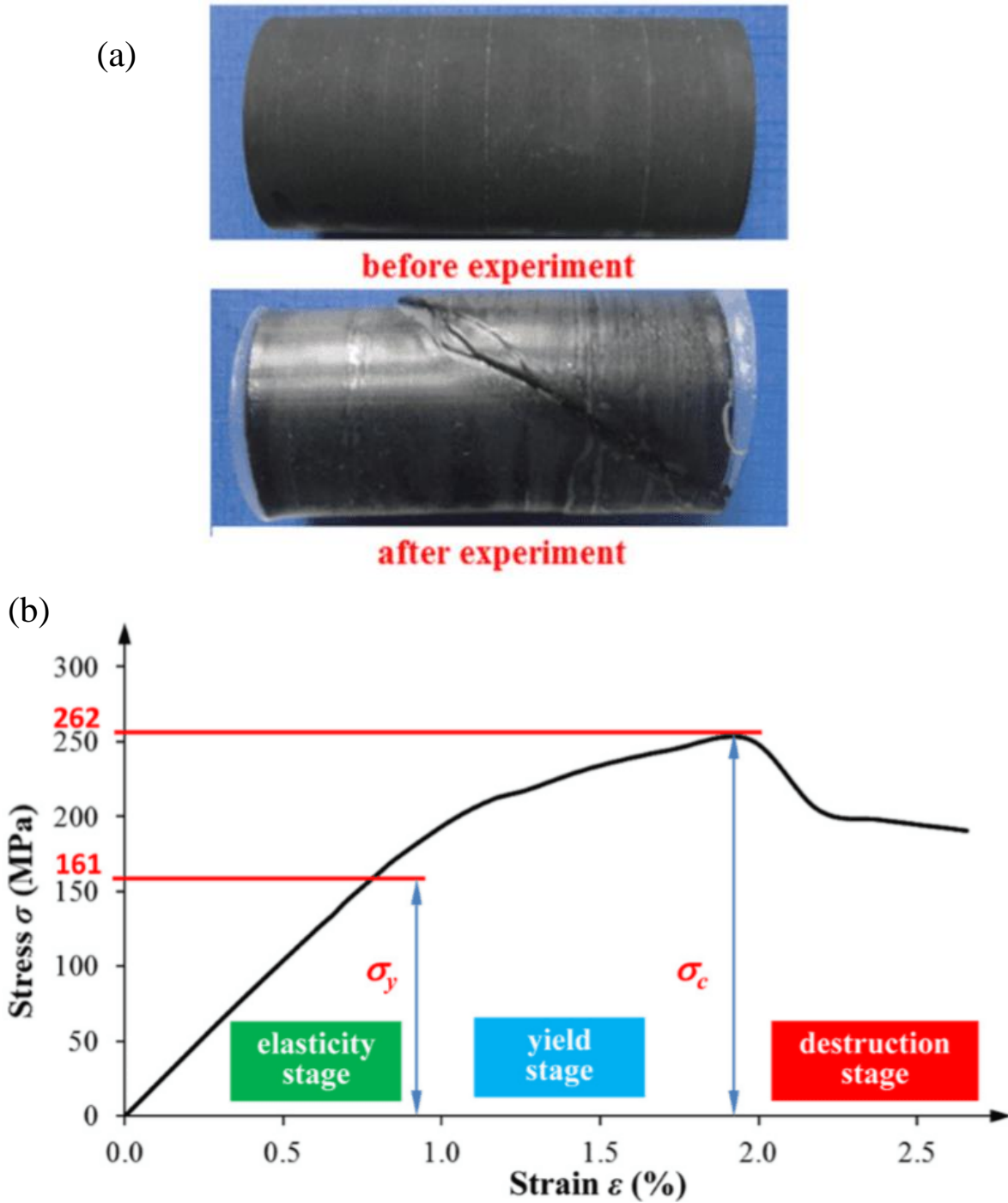
Figure 27: Compression experiment for Longmaxi Shale.
(a) a brittle failure plane from a triaxial compression test with a 53 MPa confining stress. Rock Young's Modulus is 22.6 GPa, Yield strength is 161MPa, compressive strength is 262 MPa from experiment measurement. The cohesion for this shale sample is 15MPa and internal angle of friction 43°. (b) stress-strain curve of the tri-axial compression test. 40

For a naturally fractured reservoir, it is always important to identify the fracture scale and to avoid large weak interfaces. Roussel and Sharma [63] suggested cluster space determined by average HF height. They studied stress reorientation for Barnett and claimed that fracture interval in the range of 1.4 to 2 times of fracture height. **Figure 28** shows an HF geometry in Longmaxi Formation. The stimulation stage should be more than 83 m to avoid activating adjacent HFs. Smaller fracture stage intervals highly likely to trigger severe slipping potential. Thus, the fracturing stage length should be analyzed for different fracture performance according to formation properties.
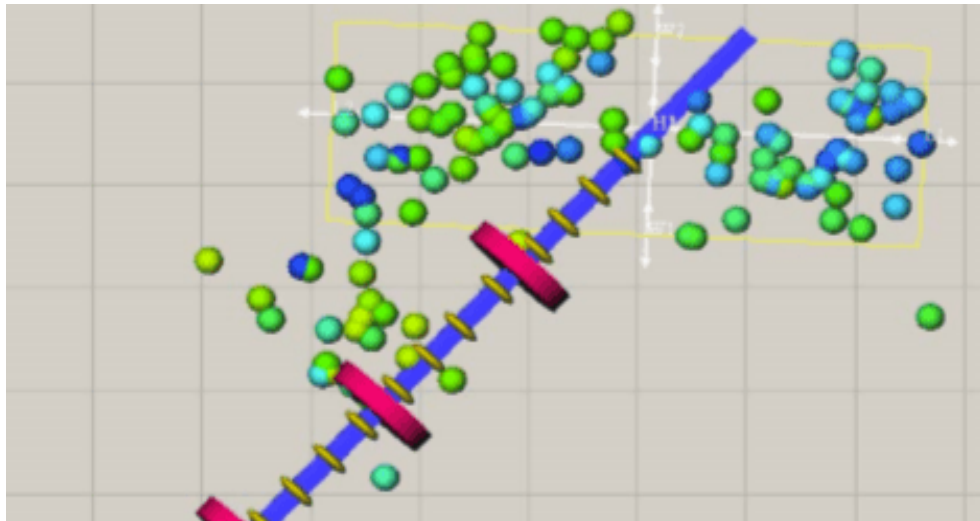
Figure 28: Fracture geometry from seismic interpretation in Longmaxi formation. Fracture dimension with a length of 272m, a width of 95.8m, and a height of 59.3m.

Chapter 4: Methodology

The governing equations are based on the mass balance of fracturing fluid and pore fluid to solve the equilibrium of the porous medium including fracture initiate and propagation criteria [56]. Hydraulic fracturing is a Multiphysics problem containing rock deformation, hydraulic fracture initiation and propagation, hydraulic fracture and natural fracture intersection, natural fracture activation and displacement, fluid flow in pores and fluid leak-off into formation. The heterogeneity and anisotropy of mechanical properties of formation further complicated the fracturing process.

ABAQUS was used in this study with the Cohesive Zone Method (CZM). CZM setup fractures pathway before simulation [56]. Tangential flow for CZM along fracture interfaces needs to generate use keyword "GAPFLOW" and the radial flow is modeled through leakoff. The simulator solves through continuity, mass conservation, constitutive relationships and momentum equations [64]. Three typical fracture propagation mechanisms are the Linear Elastic Fracture Mechanics (LEFM), the Elastic-Plastic Fracture Mechanics (EPFM), and the Cohesive Zone Method (CZM). CZM is selected for this simulation as it works better for the quasi-brittle rock matrix [65].

4.1 Cohesive Zone Method (CZM)

Introduced by Dugdale [66] and Barenblatt [67], CZM can be used to describe nonlinear relation at the fracture tip and plastic zone [65]. CZM involves fracture initiation, propagation, and failure completion stages, investigate failure mechanics combining discontinuity failure stage and undamaged continuum fields [68].

In the model, zero thickness cohesive element was used to simulate fracture behavior. The constitutive function of CZM is a bilinear traction separation law depicted in Figure 29, $\boldsymbol{\delta_n^o}$ represents the fracture initiation, $\boldsymbol{\delta_f^o}$ is the failure completion. Comparing this separation-traction law with stress-strain figure, traction can be interpreted as stress while separation can be interpreted as strain [69]. Before fracture initiation, a cohesive element is assumed to follow the linear elastic law. The break energy (G_{TC}) governs the fracture behavior. The quadratic nominal stress criterion is used in fracture initiation criteria where tractions are constrained in three directions at the interface. The material softens after fracture initiation, and fracture evolution will follow the pre-set pathway until failure completion. The cohesive element is considered fully open after failure, with zero traction. This methods can simulation fracture propagation but might encounter convergence problem during calculation [57].
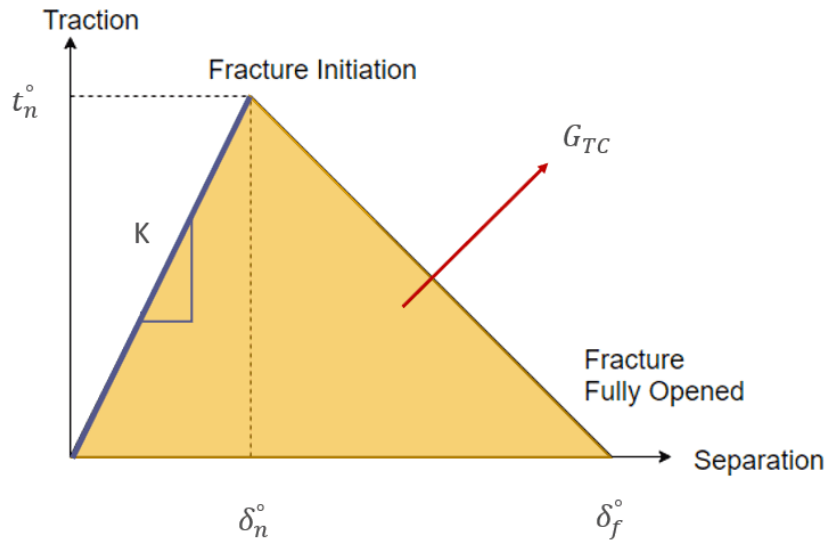
Figure 29: bilinear traction-separation law [57]

The damage initiation uses the quadratic nominal stress criterion as **Eq. 22** [69]. Fracture initiates when the sum of quadratics for the ratio of displacement and damage imitation peak in the nominal, the first and second shear directions reaches 1.

43

$$\left\{\frac{\langle t_n \rangle}{t_n^0}\right\}^2 + \left\{\frac{t_s}{t_s^0}\right\}^2 + \left\{\frac{t_t}{t_t^0}\right\}^2 = 1 \qquad \text{Eq. 22}$$

Softening part is the process of damage evolution, where $\delta^0 < \delta < \delta^f$. When the stress applying on the cohesive element reaches its ultimate tensile strength, where fracture fully opens. Energy dissipation principle, Benzeggagh and Kenane [70] (BK criteria) are selected for the damage evolution process to simulate the fracture propagation. The shear failure energy in the first and second directions are assumed to be same in the BK mode failure. G_n^C, G_s^C, G_t^C are the critical fracture energy in each direction (**Eq. 25**). η is the material paramer. The other method is to setup displacement magnitude and simulte fracturing energy release quantity.

$$G_n^C + (G_s^C - G_n^C)\left\{\frac{G_S}{G_T}\right\}^\eta = G^C \qquad \text{Eq. 23}$$

$$G_S = G_s + G_t \qquad \text{Eq. 24}$$

$$G_T = G_n + G_S = G_n + G_s + G_t \qquad \text{Eq. 25}$$

4.2 Fracture Geometry

The importance of fracture geometry is that most of the fractures are pre-designed for the cohesive zone approach. This geometry constrains the stress alteration region and determined the leakoff surface area.

KGD and PKN models shown in **Figure 30**, were the first to combine volume balance and solid mechanics. The differences between these 2 methods are the ways that they used to convert the 3D fracture model to 2D. Perkins and Kern assumed the vertical cross-section acts independently, indicated a correlation of fracture height and pressure, rather than the length of the fracture. The PKN model estimates the fracture width with a given length and flow rate.

Khristianovich and Zheltov (KGD) assume plane strain in the horizontal direction or the complete slip occurs at the boundaries of the play zone. KGD model is usually used for conditions that potentially slip happen at upper and lower boundaries. The primary assumption of KGD is a constant fluid flow rate and thus constant pressure in the main fracture body, except for the fracture tip region. As the fracture width sharply decreases near the fracture tip thus it does not involve fluid penetration.

Both the KGD and PKN models assume constant fracture heights with propagation along the fracture length and fluid flow along height direction is neglected. In the simulation, the fracture height is usually assumed to be the pay zone thickness. KGD model is suitable for the case whose length-height ratio is much less than 1, while the PKN model is the best for the scenario whose length-height ratio is more than 1 [71, 72].
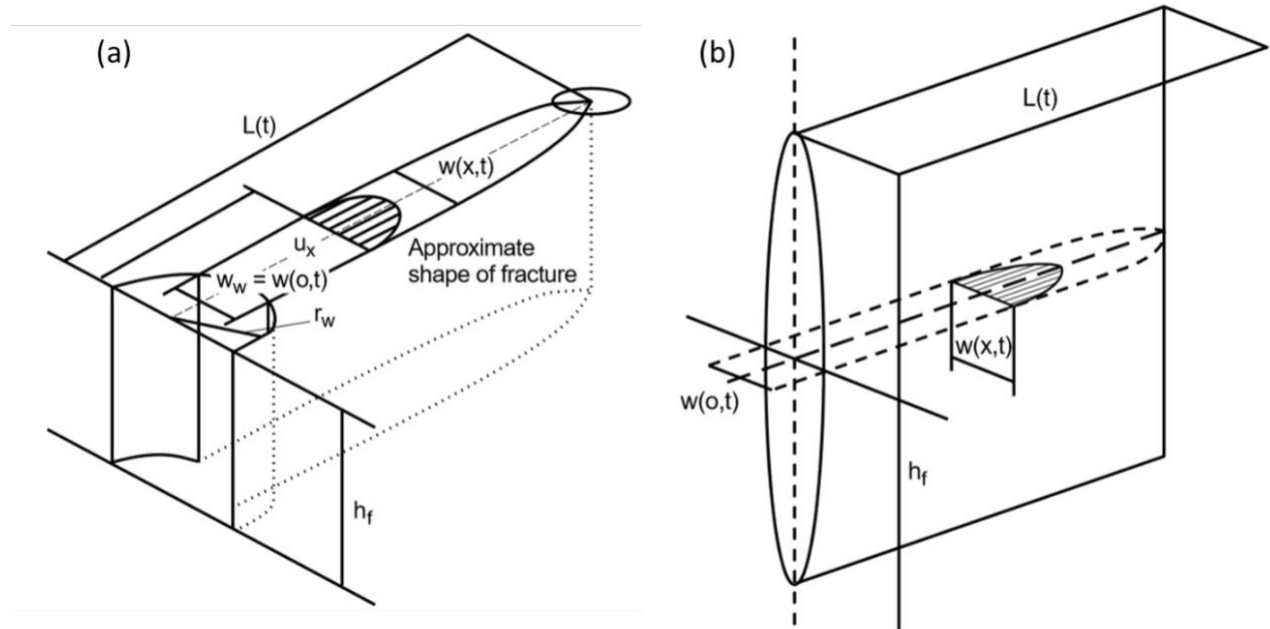
Figure 30: KGD and PKN fracture models.
(a) KGD fracture modal; (b) PKN model. w (x, t) is the width of the fracture, L(t) is the length of the fracture, r_w is the radius of the and u_x is the fluid flow velocity within the fracture

To overcome the limitations of PKN and KGD models, 3-D fracture models have a dynamic dimension where fracture height and length grow with time. Typically, there are three types of 3D fracture models, namely the general 3-D model, Planar 3-D model, and Pseudo-3D (P3D) model. Different assumptions are made for different models the Planar 3-D model assumes planar fracture extending in the direction perpendicular to the minimum in situ stress, and the P3D model has an elliptic fracture shape. Basic assumes fluid flow follows the streamline pattern from perforations points toward fracture elliptical boundary (**Figure 31**).
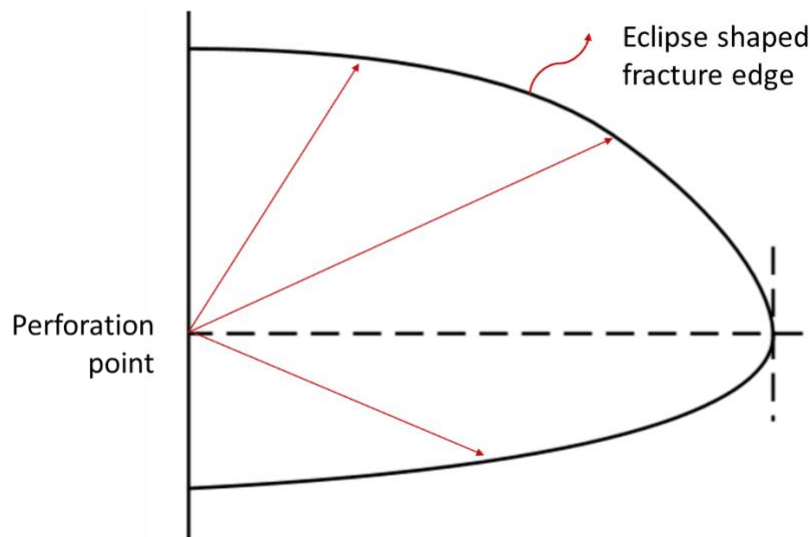
Figure 31: Schematic of P3D fracture geometry.
The fundamental assumption is that fluid flow follows the streamline pattern from perforated point to elliptical fracture edge as drawn in the figure.

Some analysts used a discrete fracture network model as shown in **Figure 32**. This type of fracture geometry can cover most of the seismic signal, yet introduce additional complexity regard fracture geometry. The naturally fractured formation is easily activated with stress field change as the volume of hydraulic fluid and proppant injected. This fracure system might overestimated conducted fracture network. Since NF actimation does not equate toward fully conduction from previous experiment results, these signals might include non-conductucted NF interfaces. Due to

these differences between natural unconformities and hydraulic fractures, this fracture geometry is not used for study casing deformation during injection.
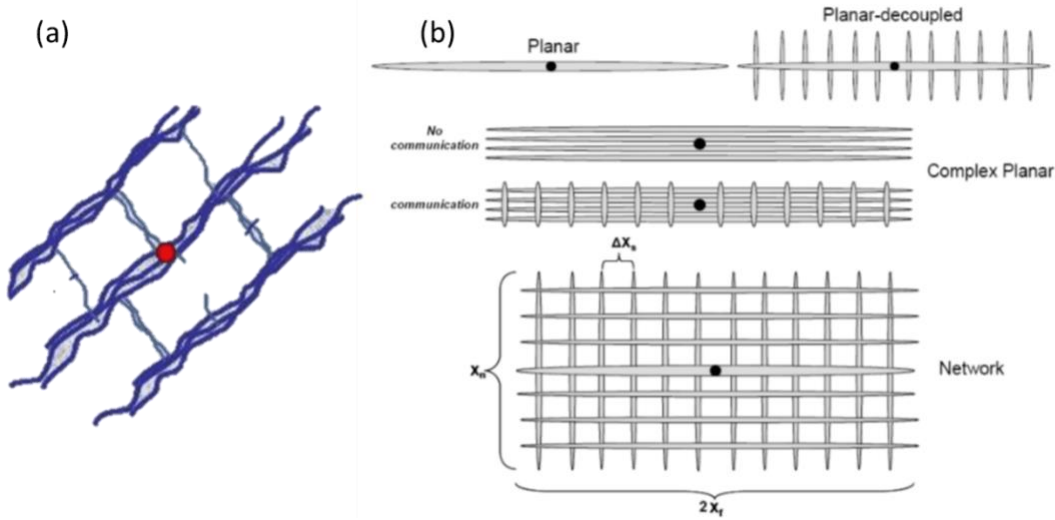
Figure 32: Discrete fracture network [73].

While fracture is not symmetrically propagating toward the reservoir, the fracture setup should take a one-sided geometry to simulate the unlanced stress change and fluid leakoff condition around the wellbore regime. Since fractures and interfaces can be categorized in open and close [27], where the tensile strength is not guaranteed to present for closed fracture. Most of the simulations select to use a small cohesion for fractures, it basically trying to calculate either the closed but none bonding interfaces, or previously activated interfaces.

Injection volume needs to be considered while determining the fracture geometry as shown in **Eq. 26** [74]. From the classical Griffith energy release theory, the fracture opening is expressed in δ_f in **Eq. 27** [75]. This separation parameter should be equal to the final fracture open width, this is the value of w. from the previous 2D study, the width is ranging from 0.02mm to 0.12mm with the injection rate from 0.0003 to 0.0009 m^3/s/m. Considering the fracture opening scale.

$$x_f = (\frac{k_f V_f}{2C_f k h_f})^{0.5}$$

Eq. 26

X_f is the half-length of the hydraulic fracture, V_f is the …., k is the reservoir permeability, and h_f is the fracture height

$$G_C = \frac{T_{ult}\delta_f}{2}$$

Eq. 27

G_c is the releasing energy rate, T_{ult} is the stress after fracture fully opened and δ_f is the ultimate fracture opening. As G_c is in the range from 10 to 30 MPa/ m^2 from previous Monte Carlo simulation, δ_f in the range of 0.02 mm to 0.12 mm from 2D solid-fluid coupled study. T_{ult} varying between 167 to 300 MPa.

4.3   Failure Criteria

This section discusses the different failure criteria for determining casing, cement, and matrix fail. Von-Mises (1913) is a failure criterion for metal (**Eq. 28**). The interpret of Von-Mises stress is that it defines failure when the 2nd deviatoric stress (J_2) reach a critical number. P110 and P140 casings have yield strength at 758 MPa and 966 MPa from the test. And the yield strength is not changing with increasing casing wall thickness. The maximum Von-Mises stress with 1.2 safety factor equal to 632MPa and 805 MPa for P110 and P140 respectively.

Drucker-Prager (1952) added the mean normal stress, J_1 shown as **Eq. 29**, into the Von-Mises criterion and get **Eq. 30.** Parameters k and α related to the cohesion of the rock and internal friction respectively. These parameters can be calculated from Mohr-Columb parameters. Since rock yield strength increase when J_1 increase, Drucker-Prager failure criterion can be validated from lab tests.

Tresca shear failure criterion (**Eq. 31)** used for analysis cement failure indicates that the failure appears while any plane of rock reaches its cohesion or shear strength. Cement cohesion is estimated as half of the uniaxial compressive strength [76]. Cement strength determines the highest

stress difference $(\sigma_1 - \sigma_3)$ that it can withstand until failure. Cement strength depends on operation quality. Simulations had interpret weak and strong cement annuli with cohesion of 225 to 500 psi (1.55 -3.44MPa) [77].

$$\sqrt{J_2} = \sqrt{\frac{1}{6}[(\sigma_1 - \sigma_2)^2 + (\sigma_1 - \sigma_3)^2 + (\sigma_2 - \sigma_3)^2]} = \frac{C_0}{3} \qquad \text{Eq. 28}$$

$$J_1 = \frac{1}{3}(\sigma_1 + \sigma_2 + \sigma_3) \qquad \text{Eq. 29}$$

$$\sqrt{J_2} = k + \alpha(\frac{1}{3}(\sigma_1 + \sigma_2 + \sigma_3)) \qquad \text{Eq. 30}$$

$$c = \frac{(\sigma_1 - \sigma_3)}{2} = \tau_{max} \qquad \text{Eq. 31}$$

Chapter 5: Cases Studies

5.1   Model setup

Modeling casing deformation involves the geological environment, the performance of induced fractures and pre-existing weak bonded interfaces, fluid flow in fractures and porous media, and operation parameters. The deformation of the casing needs to focus on near-wellbore but the faults behavior in a larger scale requires further simplification. The porosity of the target shale reservoir is in the range of 2~10%, and the gas permeability between 0.1~ 1 mD. A high permeability is applied because the model size is relatively small (50cm). Other related field parameters are listed in **Table 3.**

The fracture geometry is established with an asymmetrical planar fracture along the horizontal casing lateral. The fracture failure type combines of type I (opening) and type II (shear). The proppant transportation is out of the study scope. Matrix strains and permeability are assumed to be constant through wells in the target formation. Natural fracture or fault is opened with slickwater in the previous fracture stage, in which they have weak cohesion at the interface. Slip at cement-casing and formation-cement contact surfaces are restrained to 0, which means cement bond well on both casing side and formation side [78]. Hydraulic fracture fluid is be Newtonian fluid within fractures.

Table 3: parameters outline for well X from the dataset

Parameters	Unit	Magnitude
Depth	ft.	5108
Thickness	ft.	190
Lateral extent	ft.	3760
Porosity	%	2~10
Permeability	mD	0.1 – 1
Fluid volume	MM bbl.	1.4
Proppant	lb.	229,717 (100mesh);1,761,052 (40/70 mesh)
Pressure	psi	8702 (toe); 5801 (heel)
Stage	#	11

5.2   Governing Equations and Boundary Conditions

In simulating hydraulic fracturing process, fluid pressure applied on surface interface, solid deformation defining the aperture height and fracture opening. Energy-based fracture mechanics determine fracture propagation processes [55].

The minimum time step for stabilization for fully saturated flow is

$$\Delta t > \frac{\gamma_w(1 + \beta v_w)}{6Ek}\left(1 - \frac{E}{K_g}\right)^2 (\Delta l)^2 \qquad \text{Eq. 32}$$

Where Δt is time increment; γ_w is the specific weight of the wetting liquid; E is Young's modulus of the soil; k is the permeability of the soil; and v_w is the *in situ* velocity of fluid; β is the velocity coefficient in Forchheimer's flow and 0 as for Darcy's flow; K_g is the bulk modulus of the solid grains; Δl is a representative element length.

Fluid-Solid Coupled Equilibrium Equation is used for solid porous media with single-phase. According to the principle of virtual work, at any time t, the equilibrium equation is:

$$\int_V (\boldsymbol{\sigma'} - P_P\boldsymbol{I})\delta\boldsymbol{\varepsilon}dV = \int_S \boldsymbol{t} \cdot \delta v dS + \int_V \boldsymbol{f} \cdot \delta v dV \qquad \text{Eq. 33}$$

V is the control volume, m3; $\boldsymbol{\sigma'}$ is the effective stress, MPa; P_P is the pore pressure, MPa; $\boldsymbol{I}$ is the unit matrix, dimensionless; $\delta\boldsymbol{\varepsilon}$ is the virtual strain rate, dimensionless; S is the surface area under surface traction, m2; $\boldsymbol{t}$ is the surface traction vector, N; δv is the virtual velocity vector, m/s; f is the body force vector, N/m3.

The fluid-solid coupled continuity equation, from the law of conservation of mass, relates the fluid mass crossing the surface S at any time and the rate of the total fluid mass change in the control volume V as follows:

$$\frac{d}{dt}\left(\int_V \rho_f\,\varphi\,dV\right) + \int_S \rho_f\boldsymbol{n} \cdot \boldsymbol{v_{fp}}\,dS = 0 \qquad \text{Eq. 34}$$

ρ_f is the density of the fluid, kg/m3; φ is the porosity of the medium, dimensionless; v_{fp} is the average velocity of the fluid relative to the solid phase, m3/s; $\boldsymbol{n}$ is the unit vector normal to the surface S, dimensionless. The fluid flow in the formation follows Darcy's law as:

$$\boldsymbol{v_{fp}} = -\frac{1}{\varphi g \rho_f}\boldsymbol{k} \cdot \left(\frac{\partial P_P}{\partial \boldsymbol{X}} - \rho_f\boldsymbol{g}\right) \qquad \text{Eq. 35}$$

$\boldsymbol{g}$ is the gravitational acceleration vector, dimensionless; g is the magnitude of gravitational acceleration, m/s2; $\boldsymbol{k}$ is the hydraulic conductivity of the porous medium, m/s; P_P is pore pressure, MPa; $\boldsymbol{X}$ is a spatial coordinate vector, dimensionless.

The effective mechanical response of the solid skeleton can be described with either elastic or elastic-plastic constitutive models. The plastic behavior follows the Drucker-Prager model which is generally used to represent the constitutive behavior of granular and geological materials. The yield criterion for the Drucker-Prager model is based on the shape of the yield surface in the meridional plane. The yield surface has a linear form:

$$F = q' - p'tan\beta - d = 0 \qquad\qquad \text{Eq.36}$$

F is the yield function; p' is the effective mean stress, defined by the effective stress tensor $\boldsymbol{\sigma'}$ as:

$p' = -\frac{1}{3}\ trace(\boldsymbol{\sigma'})$, MPa; q' is the deviatoric stress, defined by the effective deviatoric stress

tensor $\mathbf{s}$ as: $q' = \sqrt{\frac{3}{2}s:s}$; β and d are the friction angle and cohesion of the material in $q' \sim p'$ the

plane, respectively.

The boundary of the model is set to be constrained from displacing in three directions. Pore

pressure change cross the boundary is 0, indicating an open boundary. Porosity is set using the

predefined field with the porosity of the matrix.

5.3   2D Injection Model

The 2-D plain strain model was established using fluid solid coupling elements and

cohesive element with pore pressure. Fixed boundary condition was used to simulate the

constraints under in-situ stresses. The study interest aims to quantify formation slippage with

various geological scenarios. Parameters that used in simulation models had been selected and

tested validate in order to avoid inconvergent scenario. As well believed that natural fracture only

needs lower level of energy to be reactivate, our model selects natural fracture shear strength 60%

of induced fracture, and tensile strength 50% of hydraulic fracture. Specified parameters are listed

in **Table 4**. An amplitude concentrate fluid injection pressure was applied onto reference

perforation point, indicated as red circle in **Figure 33**. The initial gap of 40 meters was set to

indicate perforated length. For parametric studies, injection rates are applied amplitude from 0 to

1, as injection rate start from 0 and reach at the designated injection rate at the shut-in time.

Injection rate is proportional downsized from field scale to fit model scale. Besides parameter

studies, a case study using 130 hours instantaneous injection plan is performed to compare simulated pressure history with field injection profile.
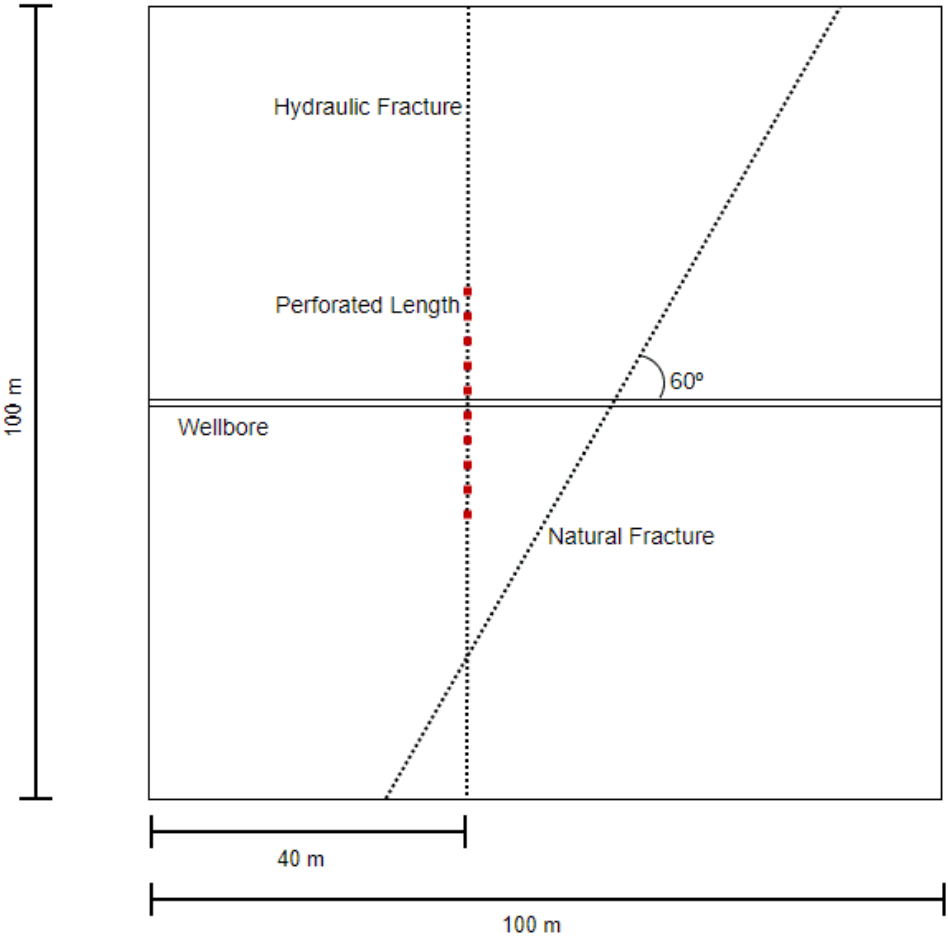
Figure 33: 2-D plain-strain schematic. Red dashed line indicate perforation length (40m). Natural fracture intersects with wellbore in 60 degrees.

Table 4: Model parameter selection.

Parameter	Value	Unit
Young's Modulus	21	GPa
Poisson's Ratio	0.25	-
Tensile Strength	2.9 (HF), 1.45 (NF)	MPa
Shear Strength	20 (HF), 12 (NF)	MPa
Matrix Permeability	0.1	mD
Void Ratio	0.02	-
Fracture Break Energy	30	J/m$_2$
Leak-off Coefficient	$2\times10_{-12}$	m$_2$/s/Pa
Fluid Viscosity	1	mPa·s
Maximum Horizontal Stress S_H	53	MPa
Minimum Horizontal Stress S_h	33	MPa
Vertical Stress S_v	48	MPa
Initial Pore Pressure	23	MPa
Injection Rate	0.0003	m$_2$/s

Figure 34 shows the formation displacements after 900s fracturing fluid injection. There are two types of displacement: symmetric and asymmetric about wellbore. The displacement shown in 4a and 4b take place as a saltation when the natural fracture slippage is initiated. This can be explained as the traction energy exceeds the fracture break energy assigned for cohesive element. Fracture opening and relative larger movement happen instantaneously fracture fully open. In addition, these figures explain why there is not a clear relationship between the casing deformation location and perforation point, which is consistent with Changning-Weiyuan

reservoirs in Sichuan Basin. Displacements around perforation points are either near 0 or negligible compared with the maximum displaced region. This indicates that the stress will not concentrate around perforation location over the entire lateral extension. Furthermore, the local stress redistribution increases the probability of casing deformation and failure.
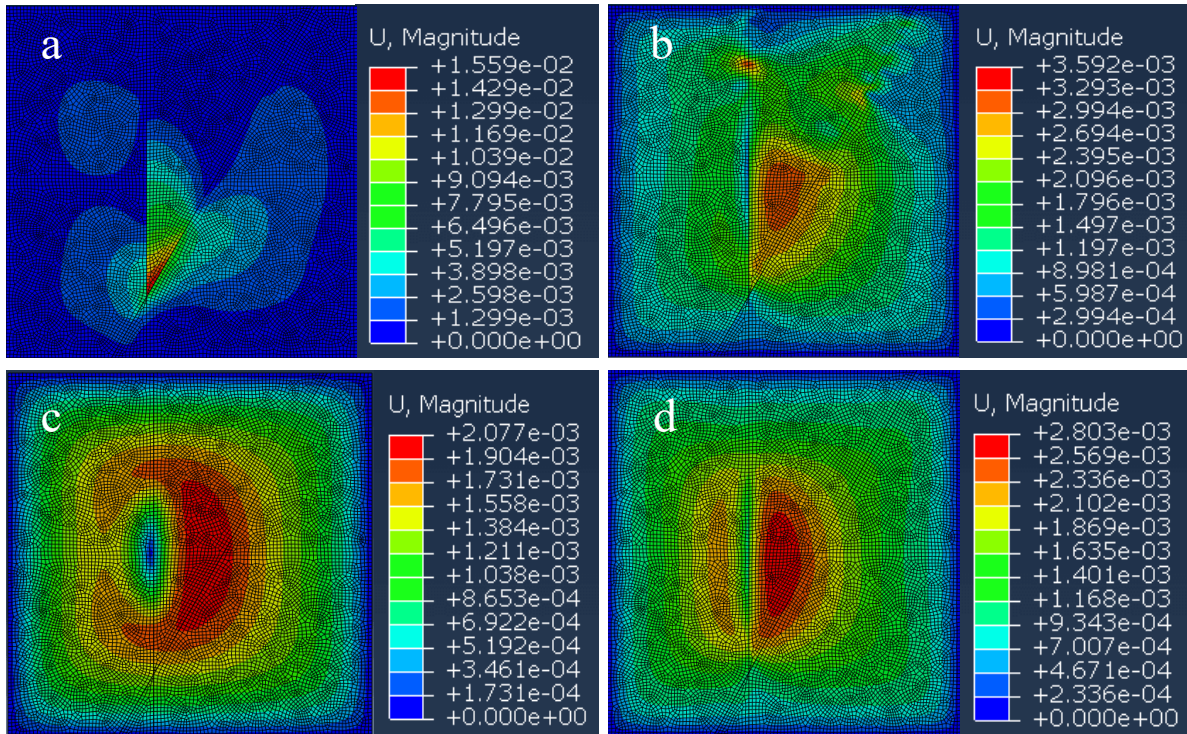
Figure 34: counter maps of formation displacements for different permeability after 900 s fracturing fluid injection (permeabilities are a: 0.7 mD; b: 0.8 mD; c: 0.9 mD; d: 3 mD)

Matrix permeability affects the fracturing fluid leakoff and in-situ stresses redistribution. For one of parametric studies, the matrix permeability is examined from 0.5 mD to 10 mD with 600 seconds and 1000 seconds. Since our model shows HF intersects with NF around 400s to 500s, thus we compare fracture slippage after fractures' intersection at 600s and 1000s. 15 simulations are performed at a step in 0.1 for permeability less than 1 mD; for permeability from 1 mD to 10 mD with a step of 1 Md. The simulation results are shown in **Figure 35**. With the increase of permeability, displacement decreases before the fracture fully opens. Figure reveals a constant decreasing trend from low permeability to high permeability. The second set for time at 1000s, we

observed that under the same time period, the displacement at the fracture and wellbore intersection is decreasing with the permeability increase before fracture initiation and after fracture open. In these permeability tests, the injection rate is set using amplitude method, increasing from 0 to 0.0003 m2/s over the injection period. Simulation results are listed in **Table 5**.

Comparing different permeability and its impact on formation slippage can also be used to interpret the scenario of different conductivity from adjacent formation layers penetrated by fractures. Due to the deposition characteristics of shale formation, shale formation intrinsically contains multiple layers while each one might have different lithology and permeability. The difference in displacement between adjacent layers might further enlarge interface movement. The discrepancy of formation displacement then further create offset around wellbore and thus suppress abnormal high stress onto cement and casing system.
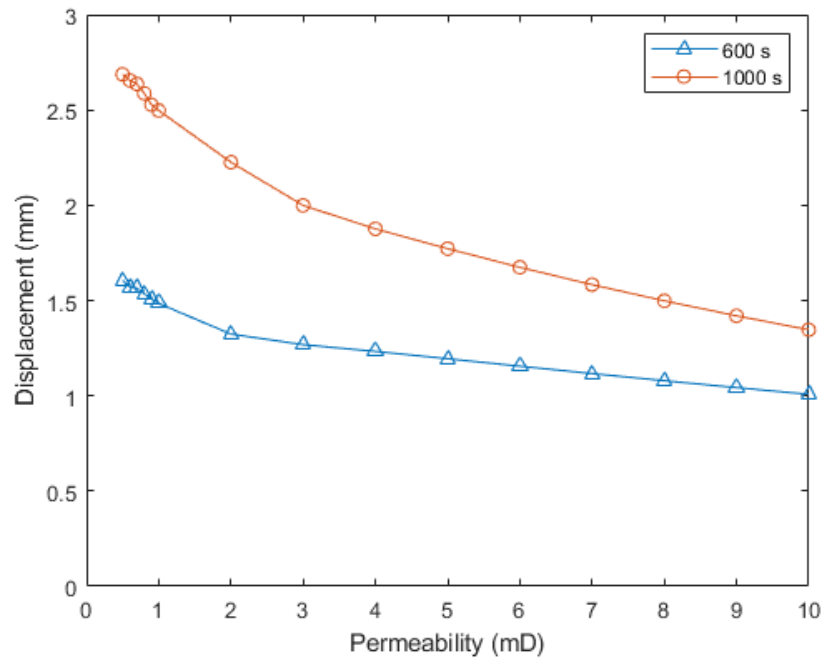
Figure 35: Displacement for simulation at 600s and 1000s permeability rage from 0.5mD to 10m

Table 5: Displacement at 9 minutes and maximum displacement for different permeability.

permeability (mD)	Displacement (mm)	
	600s	1000s
0.5	1.60	2.69
0.6	1.57	2.66
0.7	1.56	2.64
0.8	1.53	2.59
0.9	1.51	2.53
1	1.48	2.50
2	1.32	2.23
3	1.27	2.00
4	1.23	1.88
5	1.19	1.77
6	1.16	1.67
7	1.12	1.58
8	1.08	1.50
9	1.04	1.42
10	1.01	1.35

Fracturing fluid leakoff coefficient is closely related to injection fluid viscosity. In this study, leak-off coefficient values as shown in **Table 6** are tested and the results recorded in **Figure 36**. With leak-off coefficient increases, wellbore displacement at the natural fracture and wellbore intersection is lower. With leakoff coefficient increase from $1.2 \times 10^{-13} \, m^2 s^{-1} Pa^{-1}$ to $2 \times 10^{-9} \, m^2 s^{-1} Pa^{-1}$, it is observed a 13 % reduction for 0.6 mD and 22.5% displacement decrease for 0.8 mD. This indicates that a higher leak-off coefficient yields a smaller effective hydraulic fracture volume. Under the same range of leakoff coefficient, increase permeability further reduced displacement in a range of 10% to 20%. Maximum displacement results are listed

in **Table 7** and in **Figure 37**. For the same time period, leakoff coefficient increase leads to the decrease of displacement. The leakoff coefficient of $2 \times 10^{-12} \ m^2 s^{-1} Pa^{-1}$ gives the minimum displacement in the studied leakoff coefficient values. Nonlinear trend can be observing for low permeability and low leakoff coefficient.
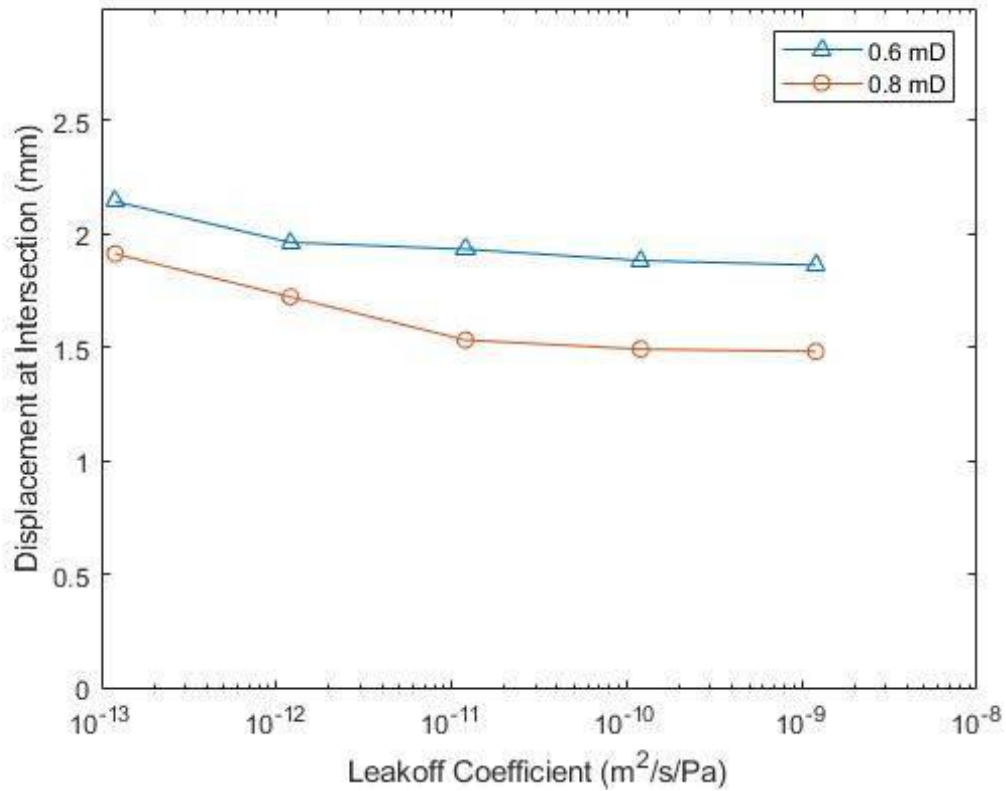
Figure 36: Vertical displacement amount of the formation at intersection of natural fracture and wellbore

Table 6: leak-off coefficient sensitivity study for permeability of 0.6 mD and 0.8 mD at 10 minutes.

	Displacement at 10 mins (mm)	
Leak-off Coefficient $\mathbf{m^2s^{-1}Pa^{-1}}$	**0.6 mD**	**0.8 mD**
1.20E-09	1.86	1.48
1.20E-10	1.88	1.49
1.20E-11	1.93	1.53
1.20E-12	1.96	1.72
1.20E-13	2.14	1.91
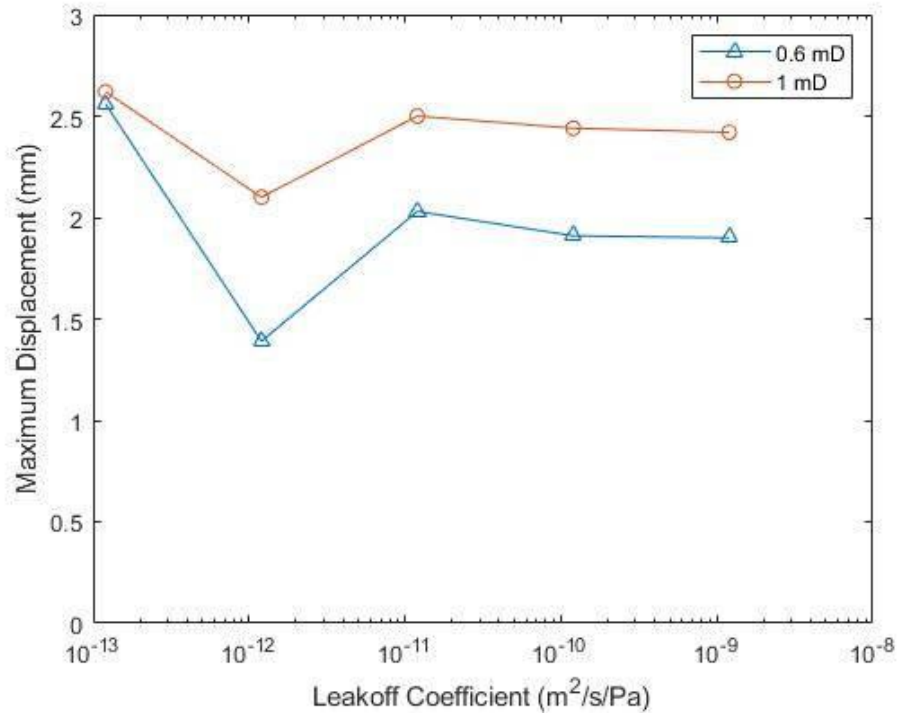
Figure 37: maximum displacement after cohesive zone break, fracture reactivated

Table 7: leakoff coefficient sensitivity study and its maximum displacement for permeability 0.6 mD and 1 mD

leakoff coefficient $m^2 s^{-1} Pa^{-1}$	Maximum Displacement (mm)	
	0.6 mD	1 mD
1.20E-09	1.9	2.42
1.20E-10	1.91	2.44
1.20E-11	2.03	2.5
1.20E-12	1.39	2.1
1.20E-13	2.56	2.62

Figure 38 shows an example of hydraulic fracture injection and pressure profiles for a field in Sichuan Basin. In order to examine our model accuracy, the injection rate is proportional to the calculated injection rate. The injection rates and injection time periods are listed in **Table 8.** Using operational perspective with a set of different injection rates, the performance of pressure is recorded and shown in **Figure 39**. From both pressure profiles, we can see the pressure history share similar pattern in filed and simulation.

Table 8: simulated injection rates with time elapse

Stage	Time (s)	Injection Rate (m2/s)
Injection	1000	0.0003
Pulse	300	0.0002
Breakdown	200	0.0007
Fracture Propagation	7800	0.0005
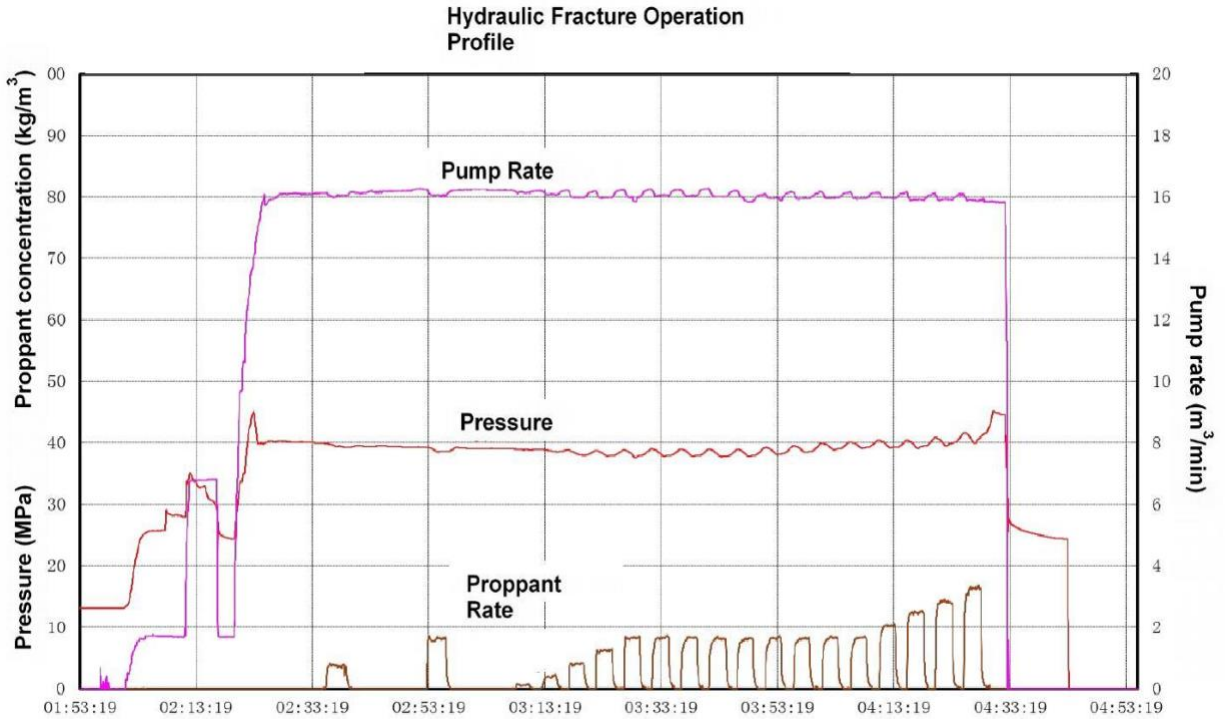
Figure 38: Hydraulic fracture field history
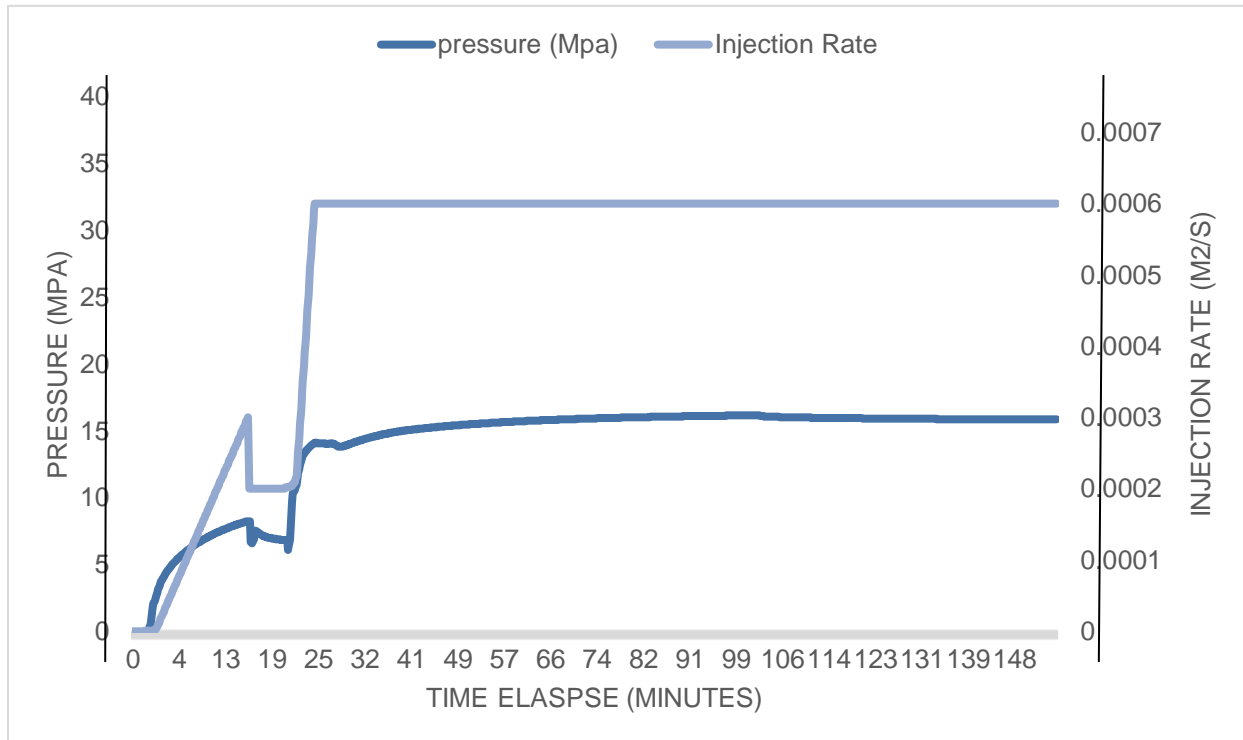
Figure 39: Simulated Pressure with Designed Injection Rates

Simulations results shows that a higher matrix permeability will yield a smaller displacement if other parameters are unchanged. This indicates that a lower permeability layer would have a high probability of undergoing a larger formation slippage comparing with vicinity shale layers. Ultra-low permeability area should be treated carefully or avoid massive hydraulic fracture to prevent reactivating discontinuous faces instead. Considering the results presented by Feng and Gray [79] for field injective test study, where a 2-D model using CZM was used to investigate the fracture breakdown, propagation and closure pressure, they concluded that with the matrix permeability and leak-off coefficient decrease, the propagation pressure would reduce. Low fracture propagation pressure results to fracturing fluid flows to interfaces once the hydraulic fracture intersected with large interfaces. Fracture fluid convert then induce natural fracture shear slippage. Moreover, Lele, et al. [80] interpreted hydraulic fracture influence from fracture and fault geometry, they concluded that if a higher permeability from intersections exists, this section would be more likely to be reactivated and prevent pressure propagating further. These observations is alighted with our simulation results. Duvernay reservoir simulated in this model is also lay in strike-slip fault regime, where the minimum and maximum horizontal stress gradients are 0.93 psi/ft and 1.24 psi/ft, respectively; and overburden gradient is of about 1psi/ft.

Sichuan basin is located in either strike-slip or reverse fault regimes where natural fractures are easily to be reactivated [10]. The excessive pressure and massive injecting volume could impact on geological discontinuous interfaces and induce shear slippage. It is important for wells in this region to keep accessibility before completion. Thus, under these extreme geomechanical environment, hydraulic fracture design in the terms of fluid volume, proppant concentration, and viscosity need be designed accordingly to alleviate the fracture displacement in order to mitigate the casing deformation probability. In ultra-low permeability regions, a conserved injection design

and longer stage distance might alleviate formation displacement compare to massive injection design. Refracture should be adopted as alternative method for production rate enhancement over depletion period. Potential solution for solving severe casing damage should increase perforation interval. On the one hand, to eliminate the possibility of intersecting with large geological interfaces. On the other hand, increase stage length also can help to design and reasonably setup fracture plan. In addition, with the combined analysis of microseismic, the large discontinuities and fault area should be avoided to reduce the displacement. There is no single design that would work for every shale. Appropriate adjustment should always be applied in fracturing shale gas reservoirs.

This study used a 2-D coupled model to study the permeability and leakoff coefficient impacts on natural fracture displacement during hydraulic fracturing process. A concentrated fluid flow load is involved to simulate injection operation at single perforated point. Model is constrained by strike-slip in-situ stresses with parameters from filed. A range of permeability and leakoff coefficient are simulated. Permeability increase will lead to smaller displacement. Leakoff coefficient has the same correlation, where increase of leakoff coefficient results in decrease of displacement quantity. Considering the complexity of unconventional shale gas reservoir, bedding planes and weak interfaces have high possibility undergo through shear reactive in injection process to different extent. Under severe situations, the displacement is large enough to damage the integrity of casing and prevent well from further completion.

Hydraulic fracturing operation is irreversible, and it is vital to assure accessibility of wellbore through the operation period. The natural fractures, geological discontinuities, and depositional bedding layers have potentials to be reactivated under volumetric hydraulic fracturing process. Weak interfaces have higher conductivity while fracturing result in fluid pressure

dissipating through large natural fracture faces and enlarging its aperture instead of propagating and creating new fracture systems. The high anisotropy of permeability and leak-off coefficient for adjacent layers would alter the hydraulic fracture performance. Therefore, different injection design from current should be tested as formation characteristics varies.

5.5   Injection 3D Case Study

The dimension of the model is defined as 50cm X 50 cm X 50 cm. fractures use 4-node two-dimensional pore pressure cohesive element (COH3D8P) and rock matrix use (C3D8P) element. The injection model schematic is depicted in **Figure 41**. The schematic of these elements and nodes is depicted in **Figure 41**. Boundary conditions of the model are fixed for displacement. The pore pressure at the boundary is 0 and porosity at the boundary is the matrix porosity. The input parameters are listed in **Table 9** which is based upon Wei201 shale gas play. The base model injection induces stress spectrum is shown in **Figure 42 and Figure 43.** From the figures, the induced stress is 371 MPa at on both top and bottom fracture-casing intersection regions**.** From isosurfaces figure (**Figure 44**), this shape match the caliper log (**Figure 45**) gathered from deformed casing in field. From Y-Z view of isosurfaces (**Figure 46**), the highest stresses applied onto fracture-casing intersection surface.

Table 9: Base injection model input parameters

Parameter	Value	Unit
Young's modulus	20	GPa
Cohesion Traction	10	GPa
Fracture Initiation Strength	100	MPa
Matrix Permeability	1	mD
Void Ratio	0.1	-
Fracture Energy Release Rate	10000	Pa·m
Leak-off coefficient	1×10^{-9}	$m_2/s/Pa$
Fluid viscosity	1	mPa·s
Maximum horizontal stress S_H	65	MPa
Minimum horizontal stress S_h	36	MPa
Vertical stress S_v	37	MPa
Initial pore pressure	29	MPa
Injection Rate	0.005	m_2/s
The specific weight of the fluid	9800	N/m_3
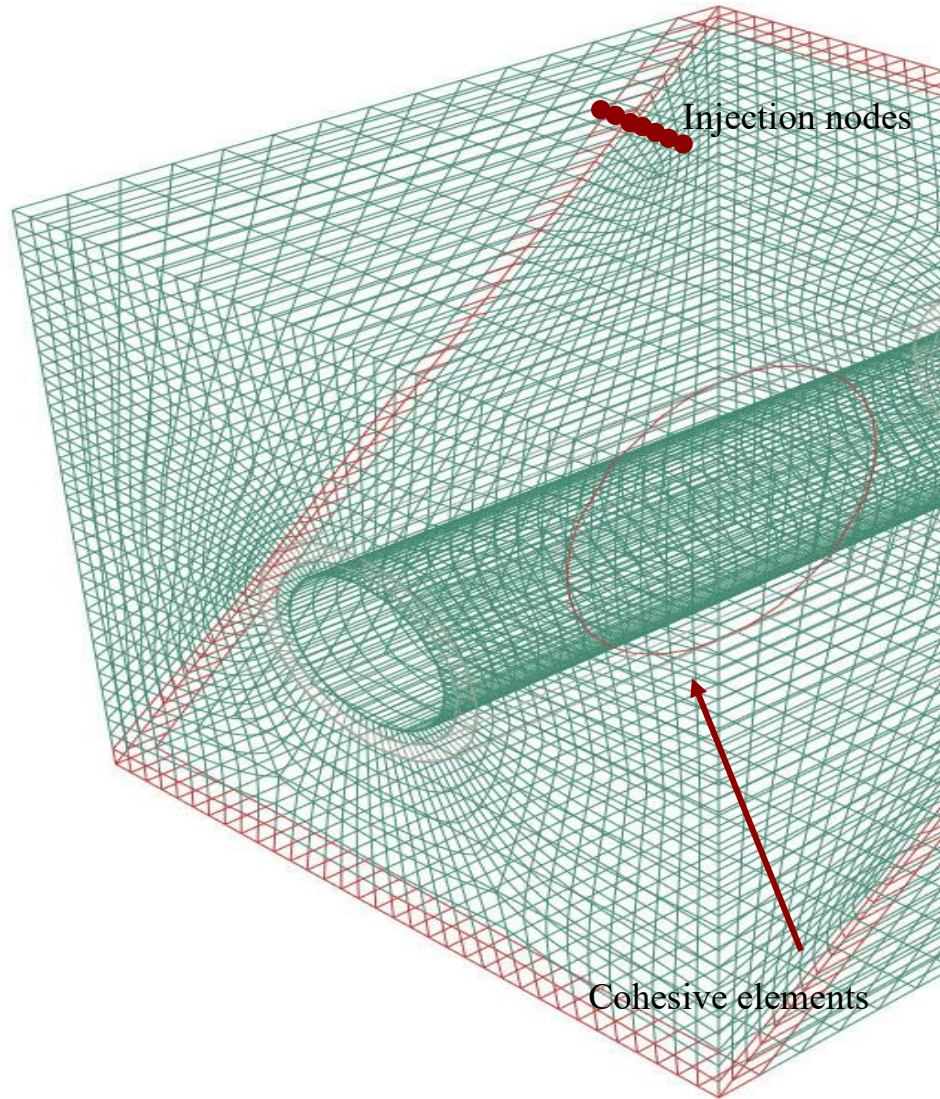
Figure 40: Schematic for injection base case.
Cohesive element is inserted in red labeled plane with a 45 degrees inclination. The base model is in 50cm×50cm×50cm scale. There are 7 injection nodes on top edge.
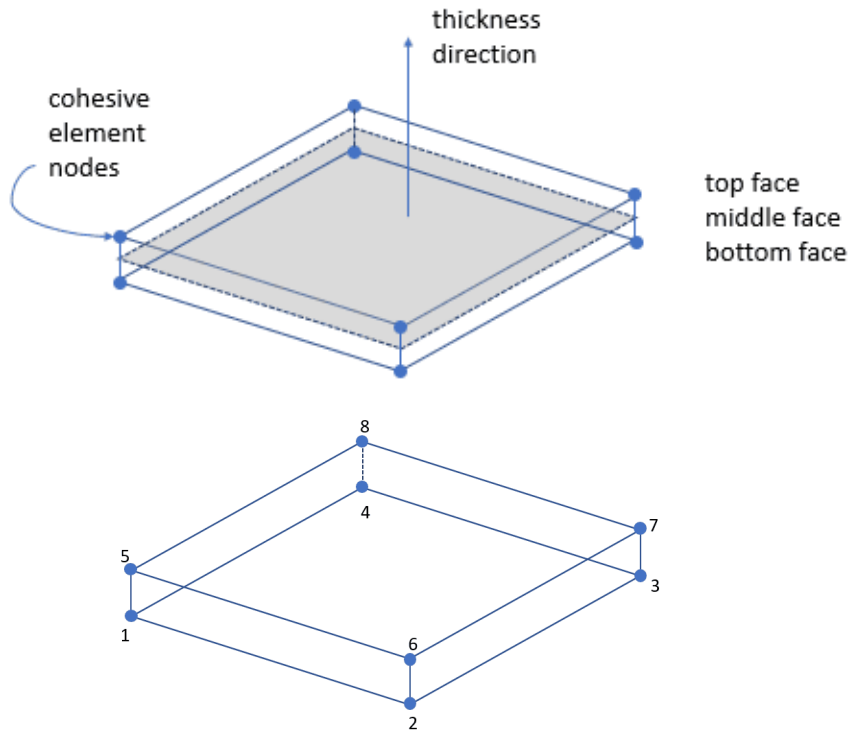
Figure 41: COH3D8P element schematic; C3D8P element schematic
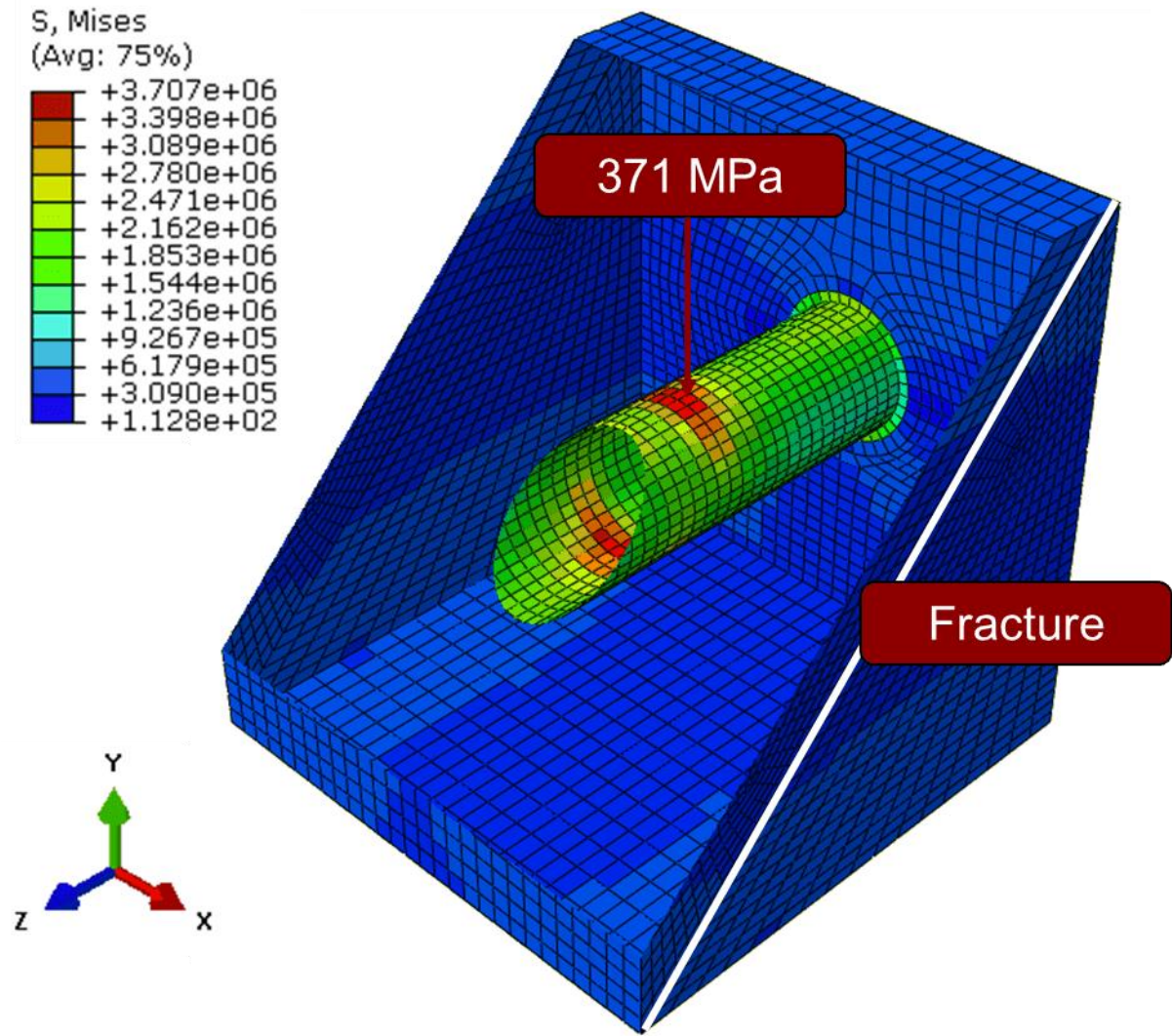
Figure 42: Base model casing stress spectrum
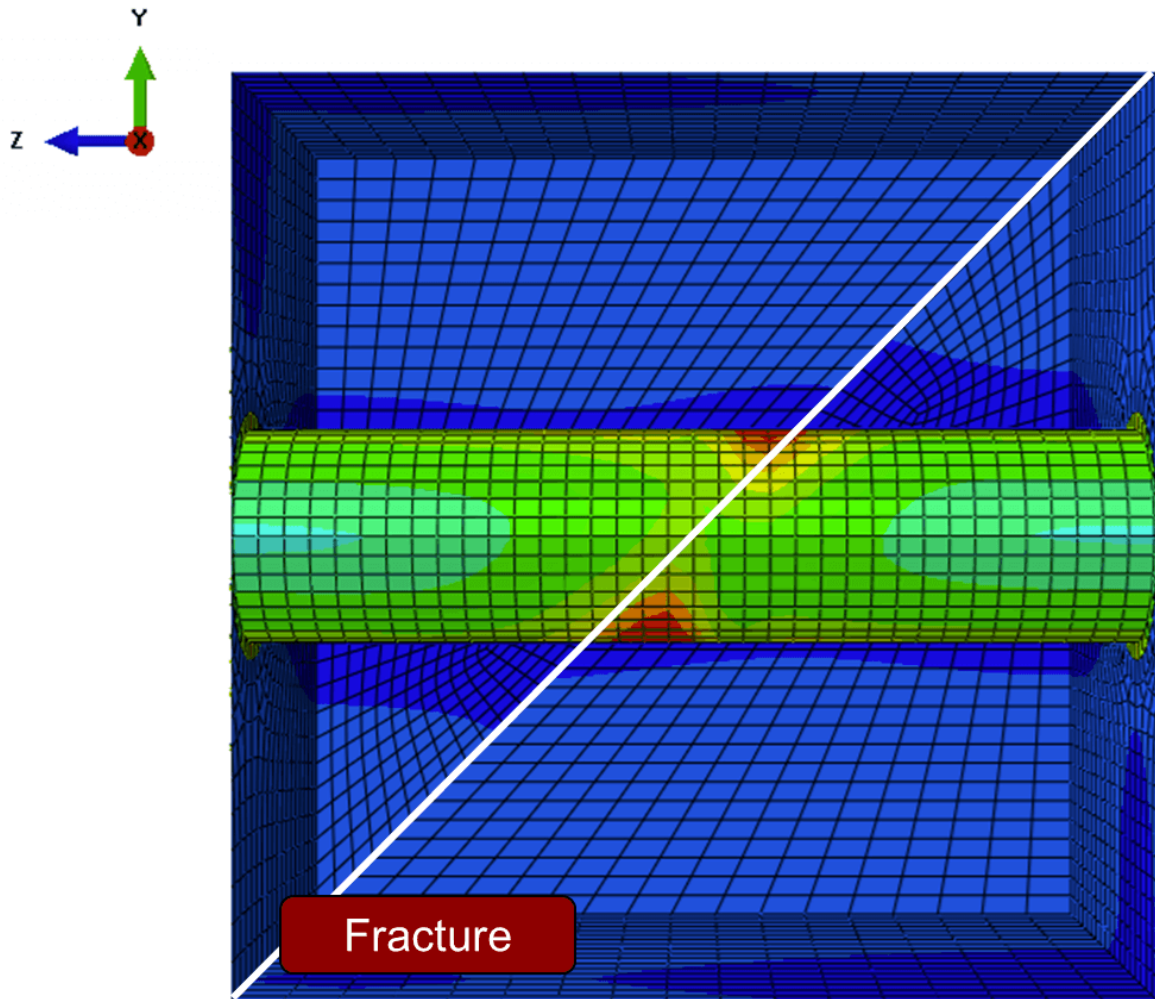
Figure 43:Base model casing stress spectrum Y-Z view
Injection model stress isosurfaces

S, Mises
(Avg: 75%)
+3.707e+06
+3.295e+06
+2.883e+06
+2.471e+06
+2.059e+06
+1.647e+06
+1.236e+06
+8.238e+05
+4.119e+05
+9.994e+01

371 MPa
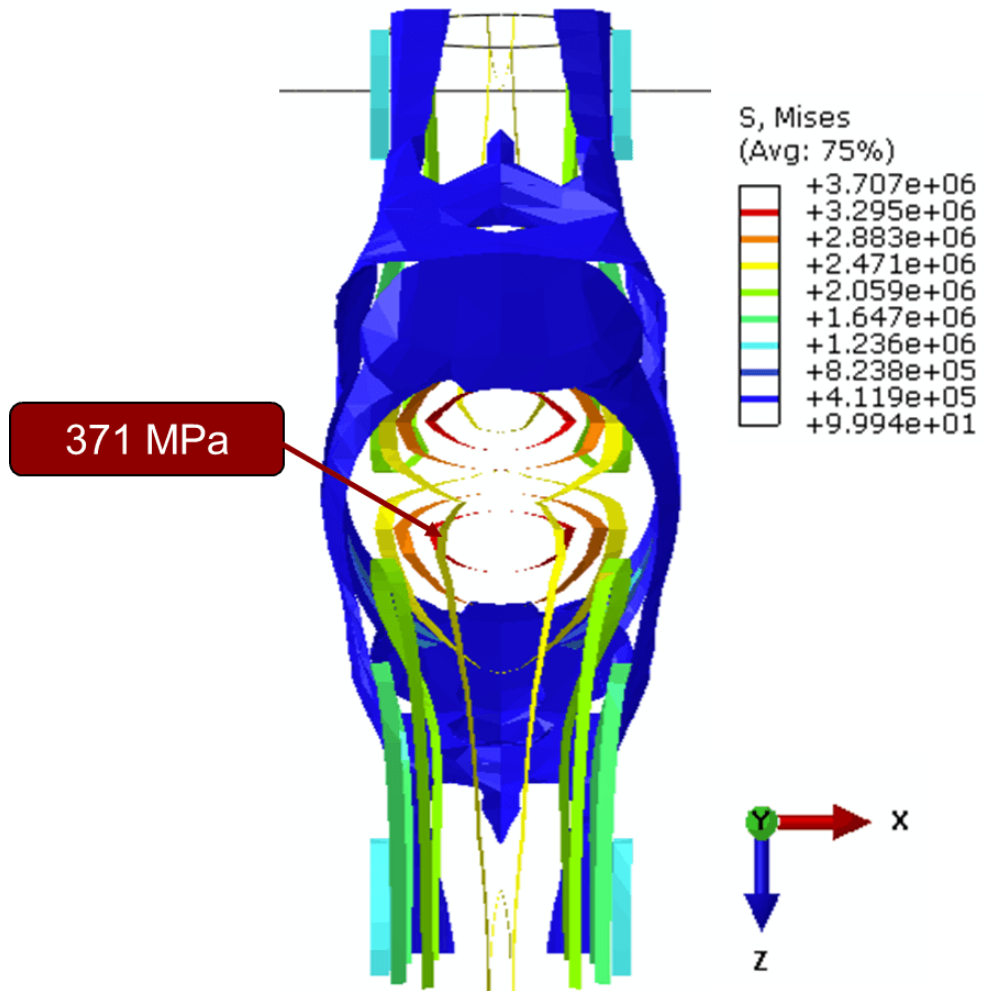
Figure 44: Isosurfaces of base case injection induced stress spectrum
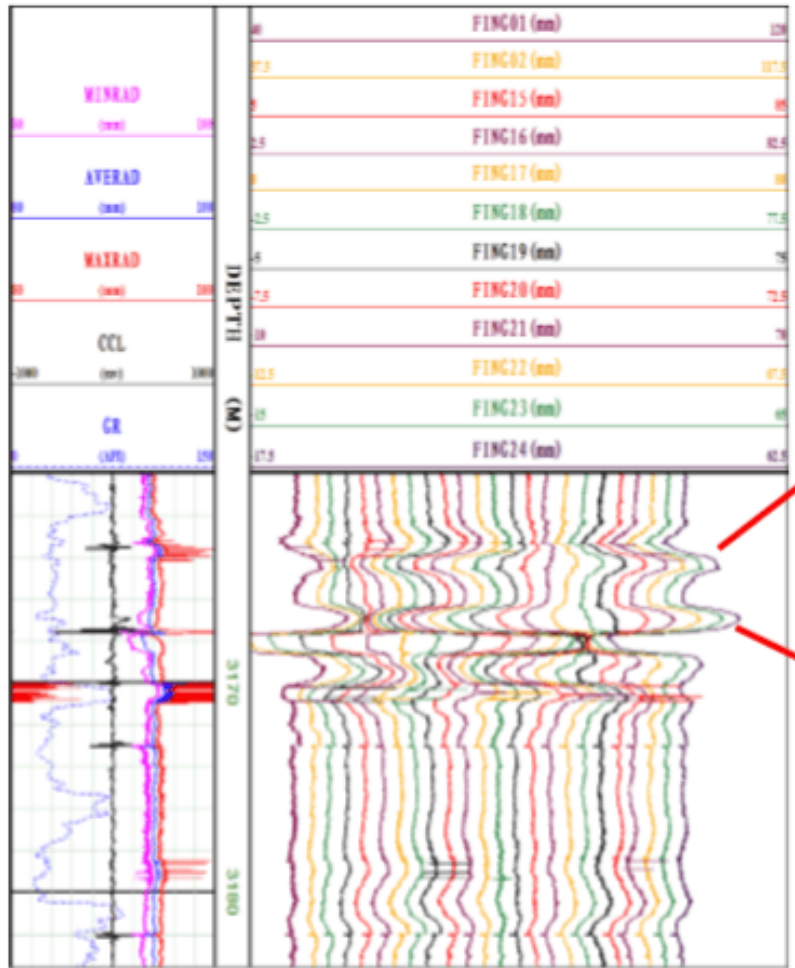
Figure 45: Caliper Logs shown similar pattern compare with casing stress isosurfaces
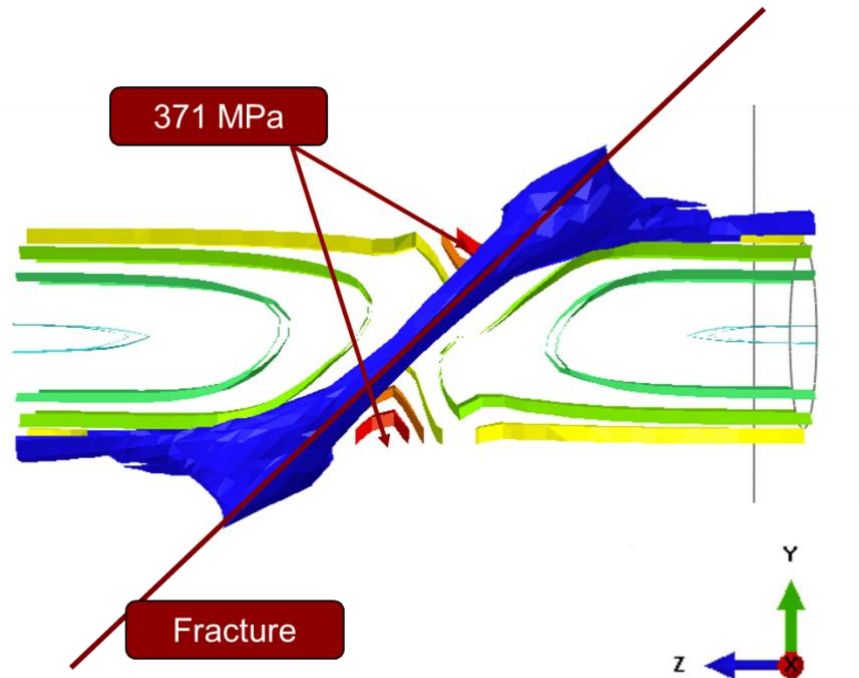
Figure 46: Isosurfaces in Y-Z view

5.6   Mechanical Model Base Case

The schematic of mechanical casing -cement -formation system is shown in **Figure 47**. The reservoir geomechanical parameters in **Table 11** are based on Ning201-H1 well since it has the most complete dataset for determining model sizes and in-situ stress. Each parameter has different range during hydraulic fractures. Material strength weakening and strengthening do not necessarily follow linear pattern, Therefore, parameter study provided a better interpretation of system stability and system strength. **Figure 48** reveals a statistical stress condition with matrix (on the left), and after completion (on the right). Since the in-situ stresses were applied to the entire system, thus the casing shown stress concentration in **Figure 48(b).**
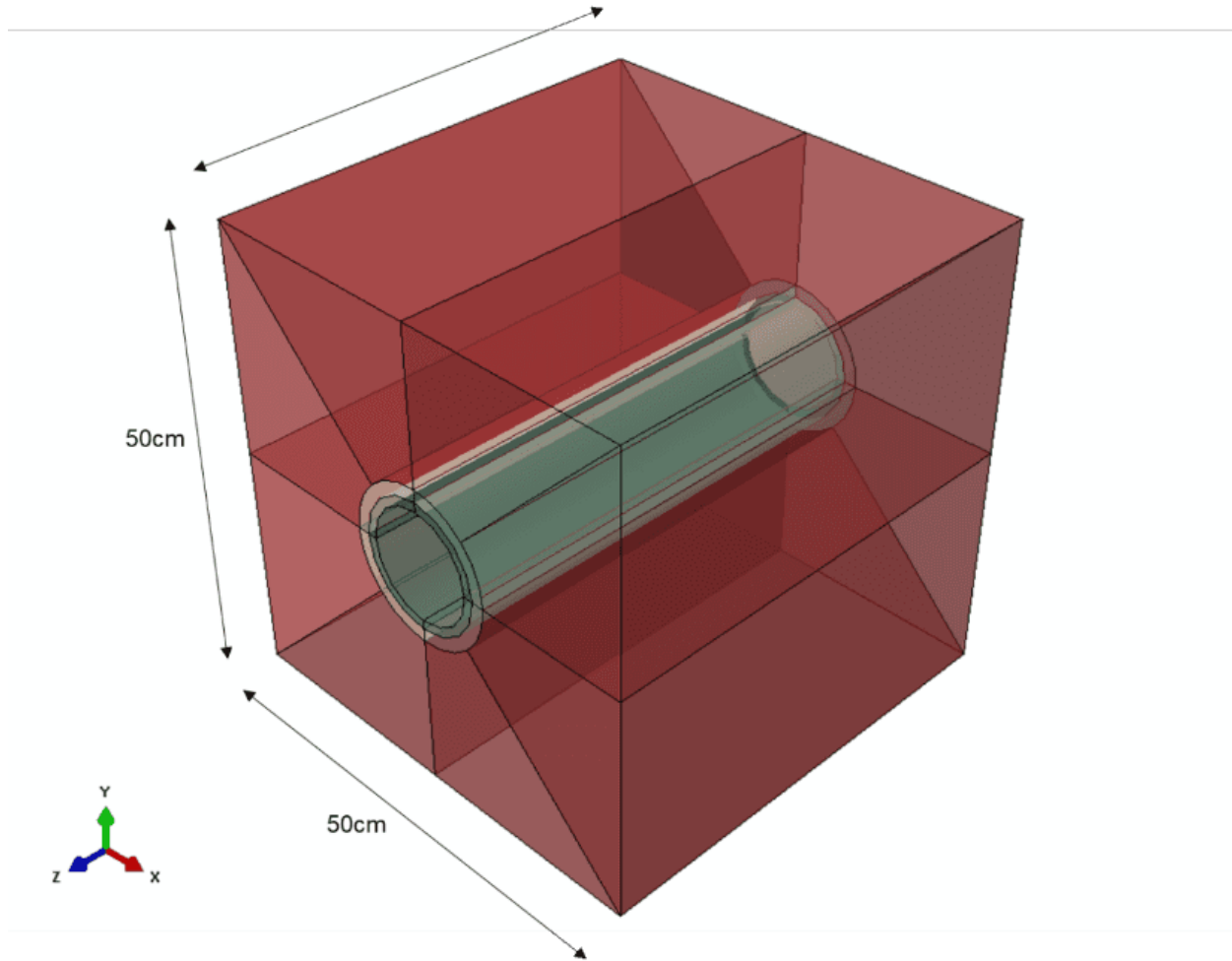
Figure 47: Schematic for casing-cement-formation system.
Dimension 50cm×50cm×50cm. Casing ID is 6mm, OD is 6mm, and cement OD is 8.4 mm.
Casing wall thickness and cement thickness using the well Ning201-H1

Table 10: Parameters calculation from the dataset

Ning201-H1		
Depth	m	2500
Biot Coefficient	-	0.7
Drilling fluid	g/cm^3	2.1
Pore Pressure	Mpa	29.4
Gravity (-Y)	cm/s^2	980
Effective in-situ stresses		
H	Mpa	65.42
V	Mpa	37.42
h	Mpa	36.42

Table 11: Mechanical properties for casing cement formation system

Parameters	Units	Casing	Cement	Formation
Density	kg/cm^3	7.85E-03	2.00E-03	2.25E-03
YM	Pa	2.07E+09	6.50E+07	2.00E+08
Poisson's Ratio	-	0.3	0.18	0.2
Permeability	mD	-	-	1.00E-09
Void Ratio	%	-	-	5
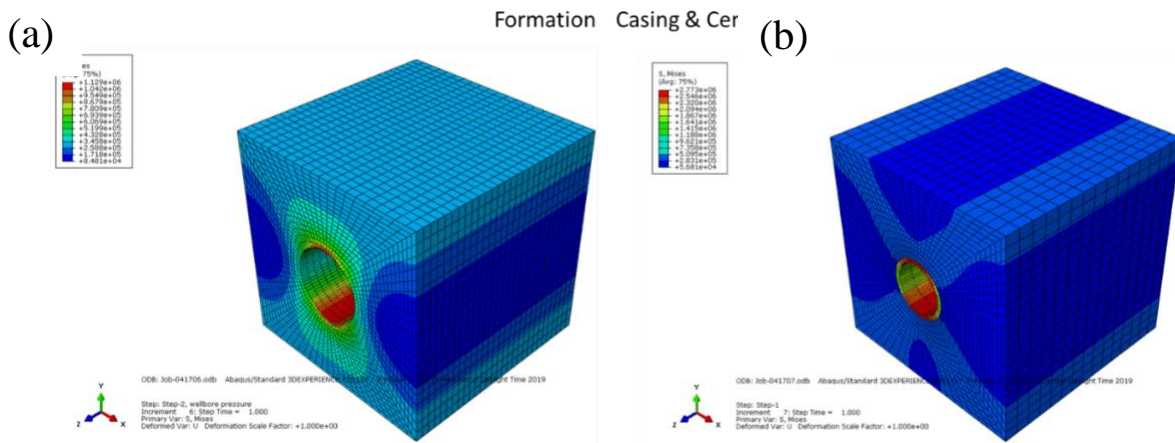
Figure 48: the geostatic stage for the casing-cement formation system.
(a) Results of geostatic stable step for formation;
(b) Casing installed. Hydrostatic pressure is applied to the tubing surface.

The deform ratios of the casing for known wellbores are listed in **Table 12**. The deformation percentages have value ranging from around 80% to 90%. As the lead print from given wellbores is mostly deformed singled sided. Thus, it is possible to simulate the movement from the slippage of fracture interfaces as a pressure applied onto the near-wellbore region. A pressure 10Gpa is used as it results in similar deform percentage with base model dimensions (50cm×50cm×50cm). Simplify the slippage movement as pressure applied upon wellbore is also efficient about testing whether different casing and cement design can alleviate the deform caused by displacement of natural fracture. The goal of this study is to compare possible approaches that

are available to reduce displacement magnitude and prevent the deformation from damaging the depletion of the wellbore. **Figure 49** is a vector map after simulating casing deformation. The simplification of on top pressure results in a 93% (**Table 13**) shrinkage of casing ID, which is similar to filed condition. Although it is not realistic to apply 10 GPa pressure onto near wellbore region. This part is aiming to examine casing and cement properties under the detected field casing deform ratio.

Table 12: deformation scenario from dataset

	Original ID (mm)	Stuck ID (mm)	Deform ratio (%)
Ning 201-H1	121.36	112	92%
Wei 201-h1	121.36	105	87%
Gong 115	97.18	76	78%
YS108H11-1	116	99	85%
Estimated Original Casing ID (mm)			
H2-6, H2-7, H3-6	121.36	96	79%
	121.36	100	82%
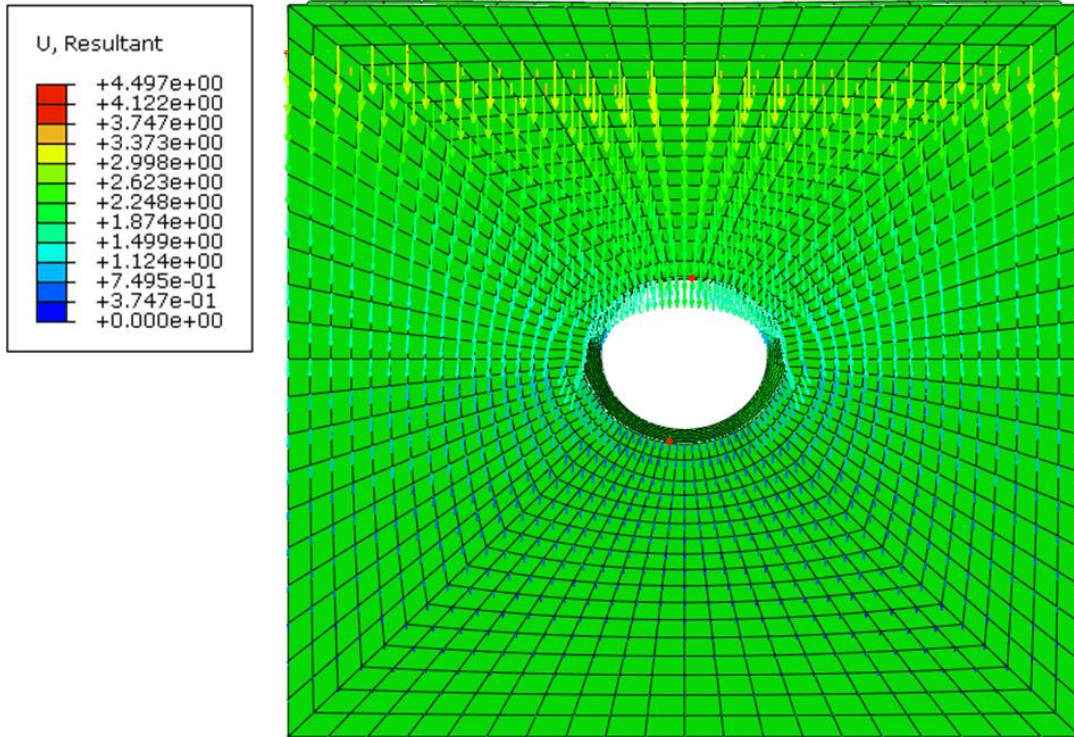
Figure 49: Vector graph for deformation level under loading at 10 GPa

Table 13: deform ratio from simulation

Original ID (mm)	Load ID (mm)	Relative Deform (mm)	Deform Ratio (%)
120	112	8.8	93

Chapter 6: Sensitivity Study on the Mechanisms of Casing Deformation

Given the large uncertainty of parameters in modeling the casing deformation, it is necessary to quantify their impacts on the induced stress upon casing. The base model used the most likely values of Longmaxi, parameter sensitivity studies were done in this chapter.

6.1   Injection model

Figure 50and **Figure 51** compared in-situ stress anisotropy impacts on injecting induced casing stress. The Maximum stress applied onto casing is 285 MPa and 371 MPa for isotropic and anisotropic scenarios with 86 MPa differences. Ave 75% in **Figure 51** legend is the default averaging threshold representing relative point stress. Default average threshold number defining points that its results was averaged. 100% yields the most smooth result graph, 0% yields the most discrete result map.
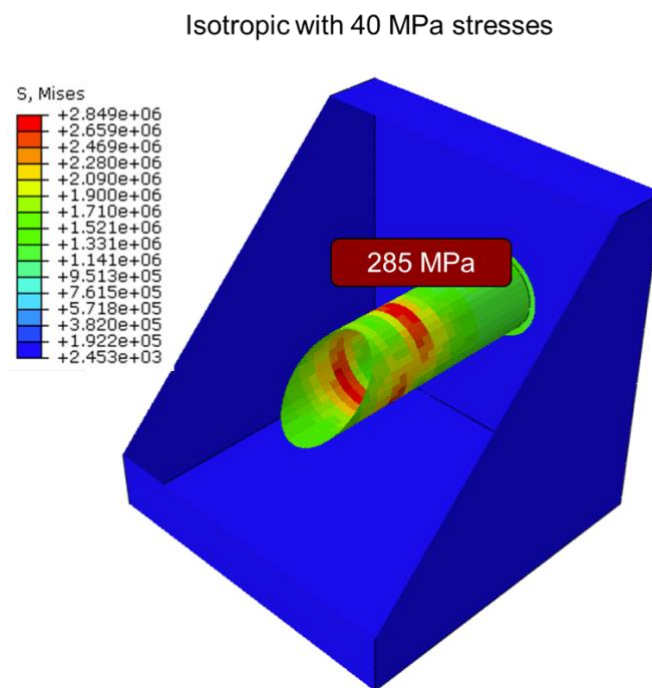
Figure 50: Injection model with isotropic in-situ stress set
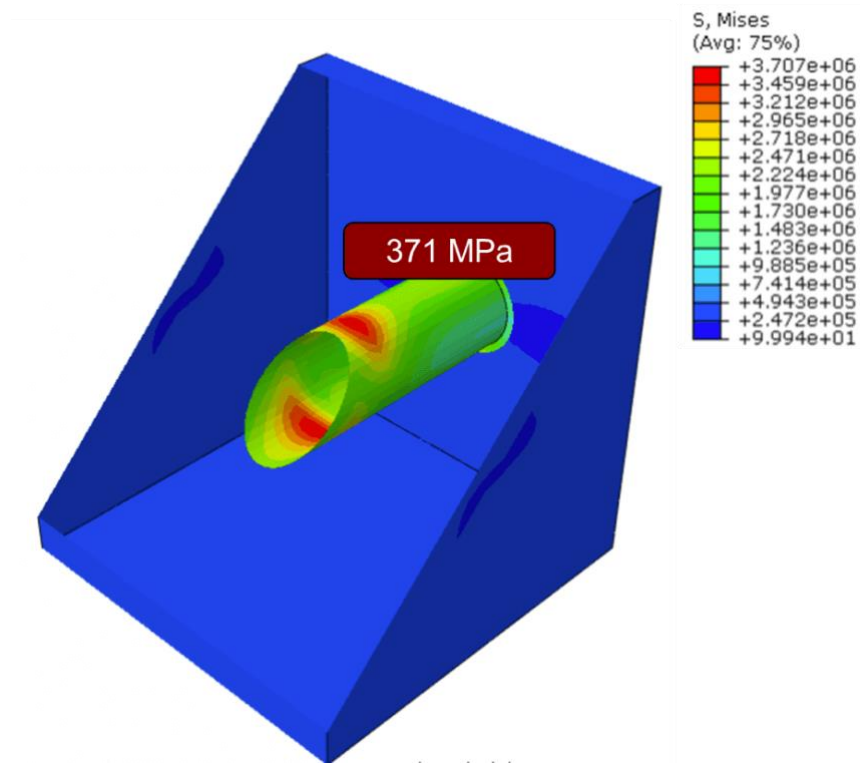
Figure 51: Injection model with Longmaxi in-situ stress.

Other than in-situ stress influence, injection rate from 0.002 ml/s to 0.005 ml/s are simulated for understanding its impacts on casing stress. The maximum fault-casing intersection stress have a difference of 163 MPa (**Figure 52**). Higher injection rate induces the larger stress (**Figure 53**). 648 MPa stress induced from 0.005 ml/s rate is already over Von Mises equivalent stress for P110 casing with a 1.2 safety factor (**Table 14**). This can be supportive evidence about injection causing casing deformation. The results of injection rates sensitivity studies is shown in **Figure 54**.

0.002 ml/s equivalent to 0.014 ml/s
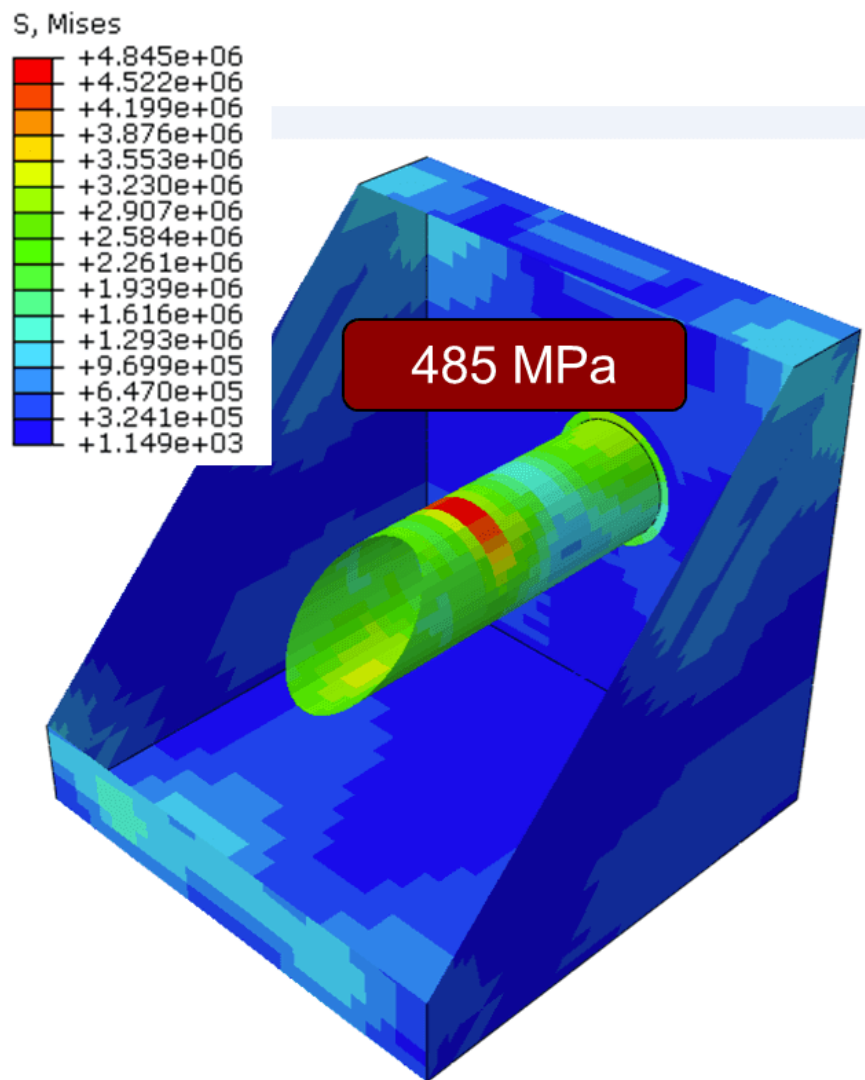
Figure 52: Stress spectrum with 0.002 ml/s injection rate
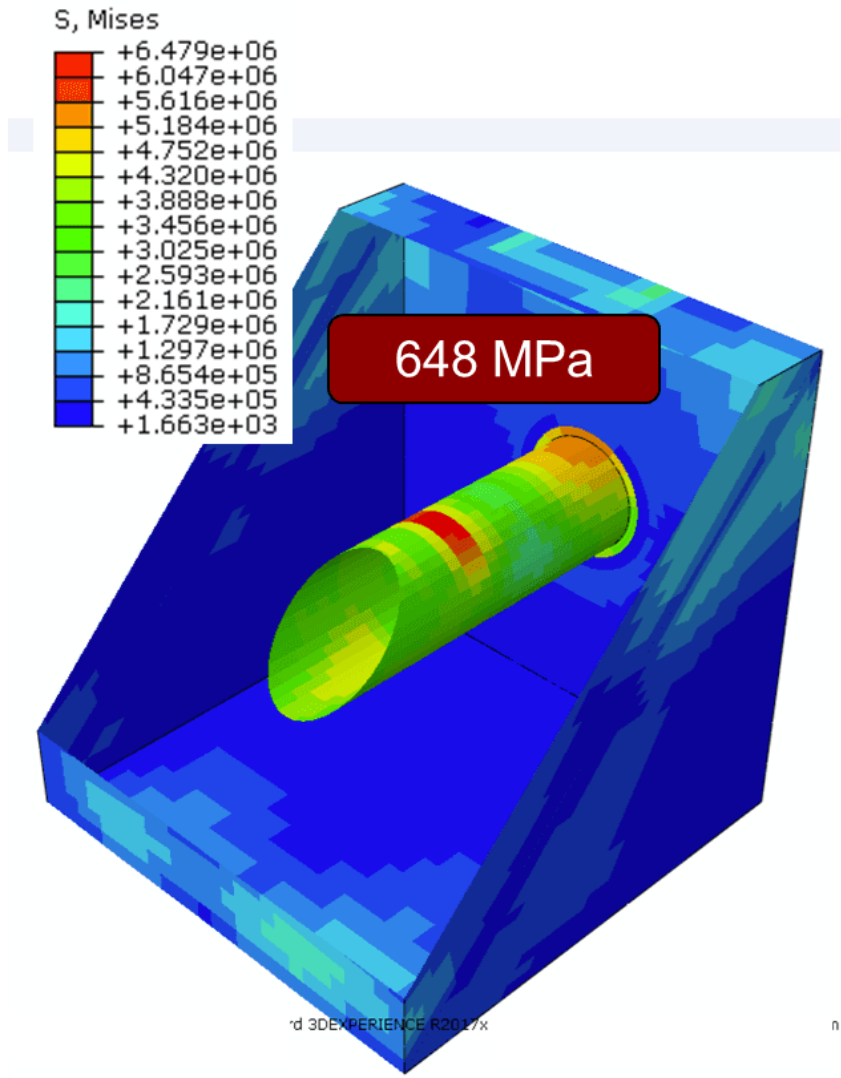
Figure 53: Stress spectrum with 0.005 ml/s injection rate

Table 14: Von Mises equivalent stress

Casing Grade	Von Mises Strength (MPa)	1.1	1.2
P110	758	689	632
Q125	862	784	718
P140	965	877	804
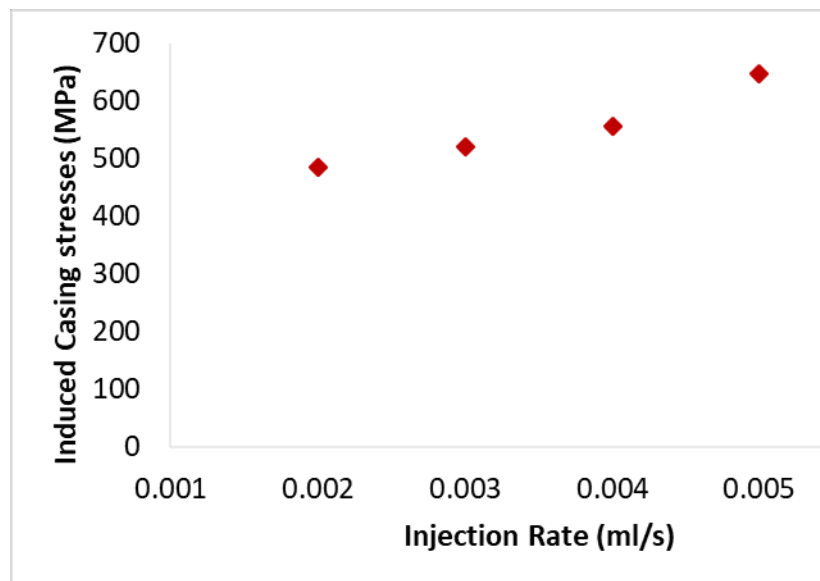
Figure 54:Injection induced maximum stress for injection rates studies.

Leakoff coefficient did not have a large impact on induced stress. Lower leakoff coefficient (1×10^{-10}) and higher leakoff coefficient (1×10^{-8}) shown 522 and 521MPa induced stresses respectively. This is reasonable due to the small model size. A model with larger leakoff area might yield better leakoff sensitivity study results.
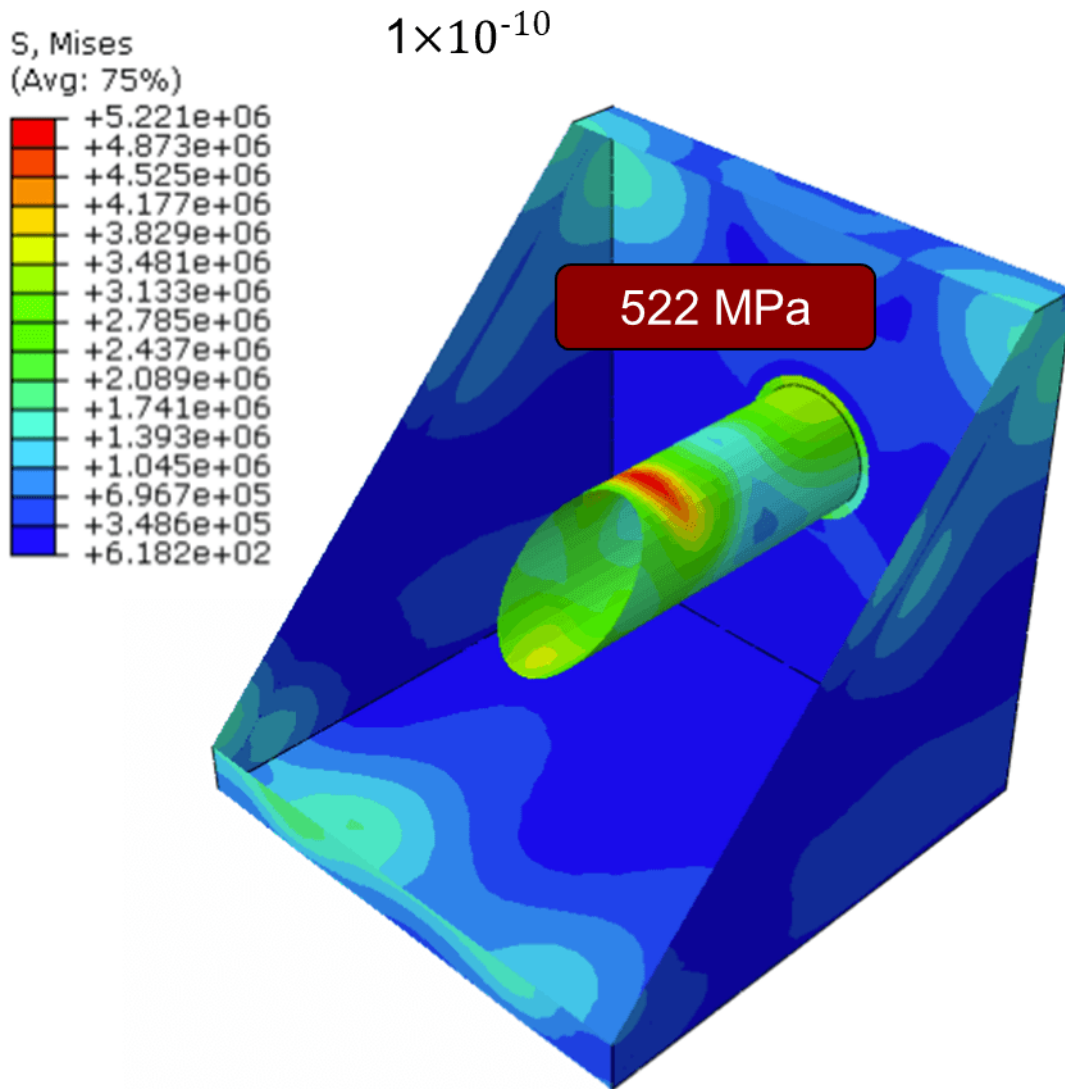
Figure 55: Casing stress spectrum with 1×10^{-10} fluid leakoff coefficient
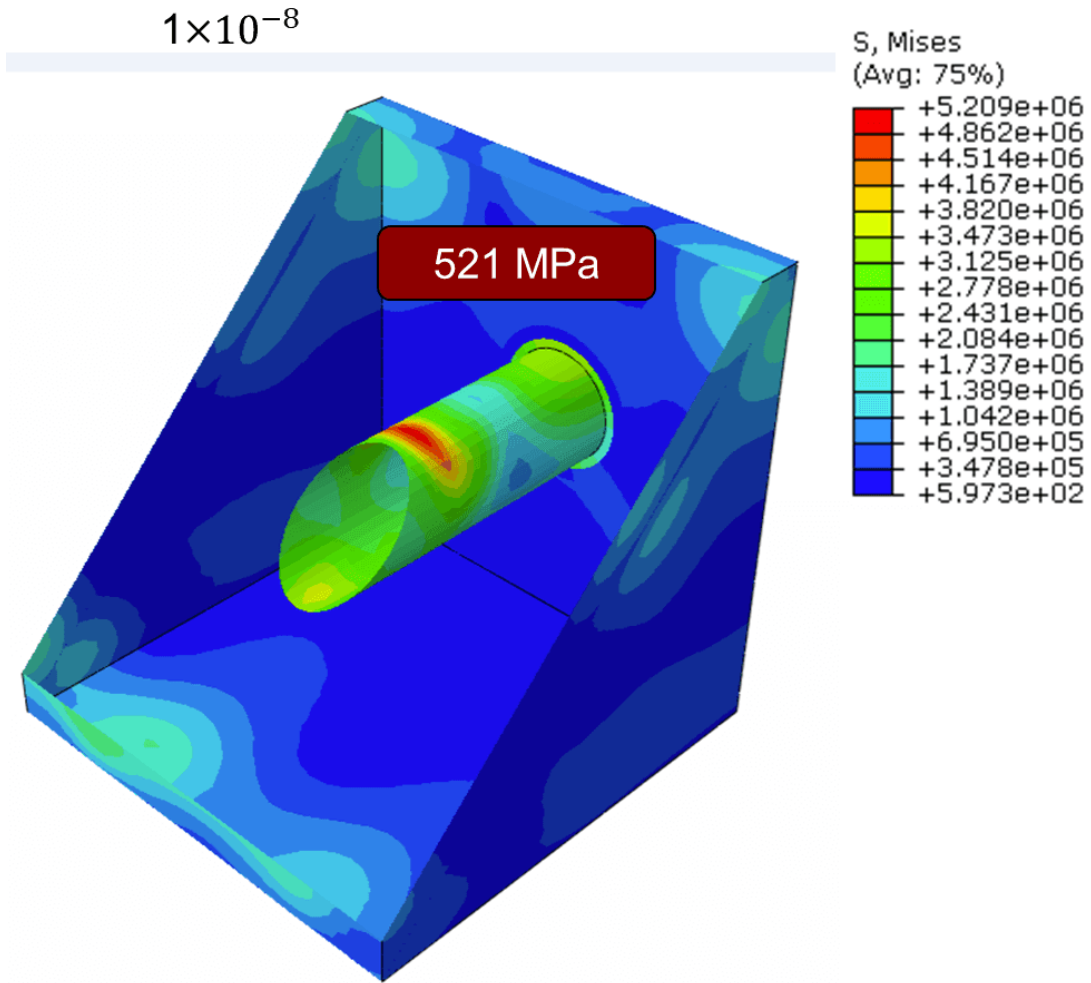
Figure 56:Casing stress spectrum with 1×10^{-8} fluid leakoff coefficient

6.2   Mechanical Model

In this section, young's modulus, poison's ratio, and cement thickness are studied and summarized. Parameters studies plotted with a 5mm displacement line, indicating the minimum equipment size that can pass through shortened casing. The cohesion of the bond between cement and casing could also change the stability of completion, however, it is excluded in this section. The input parameters for the base case is summarized in

Table 11 and the casing deformations are shown in **Figure 57**. Equivalent loading pressures take values at 5 Gpa, 10 GPa, and 15 GPa were applied to test casing deform ratios. The simulated displacements are plotted in **Figure 58 and Figure 59.** Assume used drilling bits are 7.625 inch and 8.625 inch. Casing OD for sensitivity studies use 194 mm and 220 mm for simulation. For the casing with the OD of 194 mm (**Figure 58**), increasing cement Young's Modulus improved the cement mechanical strength. For Poisson's ratio increase from 0.14 to 0.22, the cement mechanical strength does not show obvious improvement, as 8GPa pressure lead to 5 mm displacement of the casing ID. Young's modulus of cement seems to have the most obvious impact of reducing casing deformation. Comparing the displacement casing ID with 194mm and 220 mm OD, reduction of deform ID is about 1 mm for 10 GPa load cases.
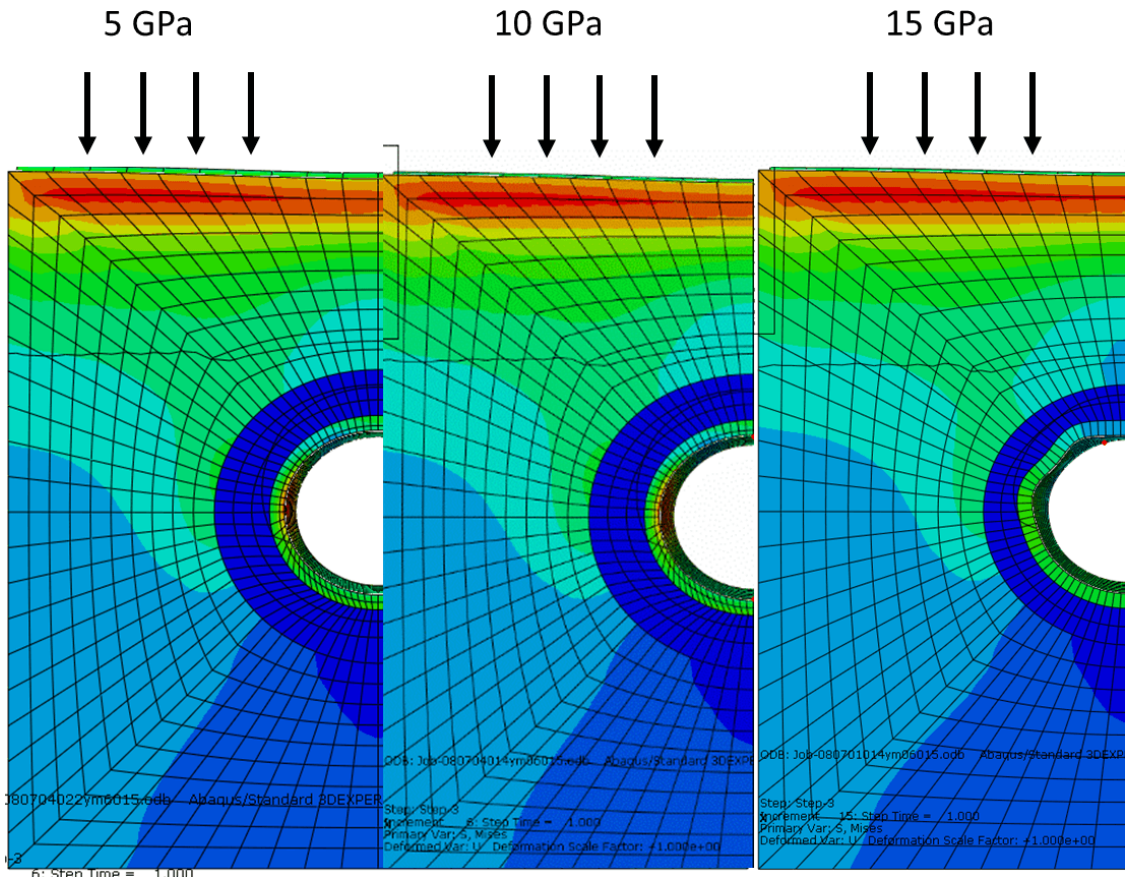
Figure 57: Casing deformation for different overloads.
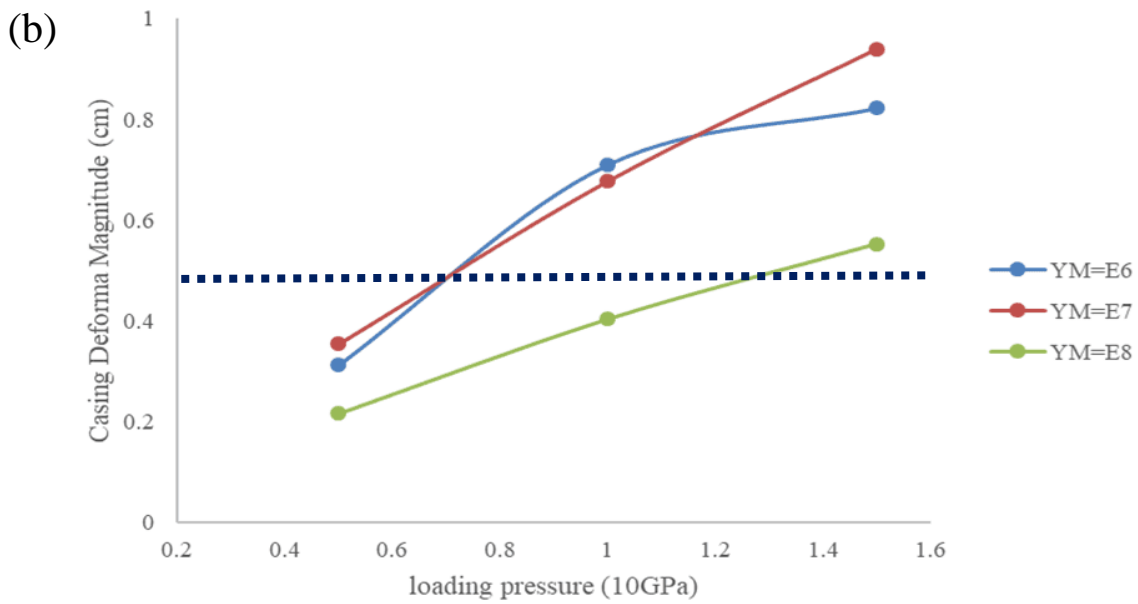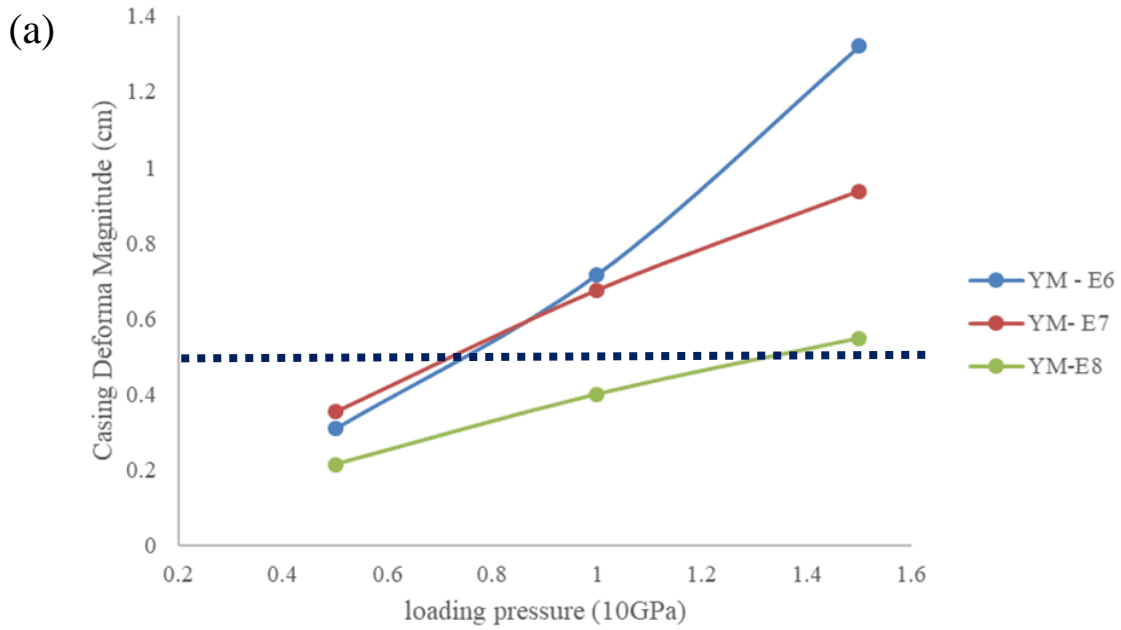
Figure 58: Sensitivity studies for 194mm casing ID, upper is Poisson's ratio 0.14, lower is for Poisson's ratio 0.22.
The loading on casing used the value of 5GPa, 10GPa, and 15GPa. where Young's Modulus taking values of 3GPa, 300MPa, and 30MPa
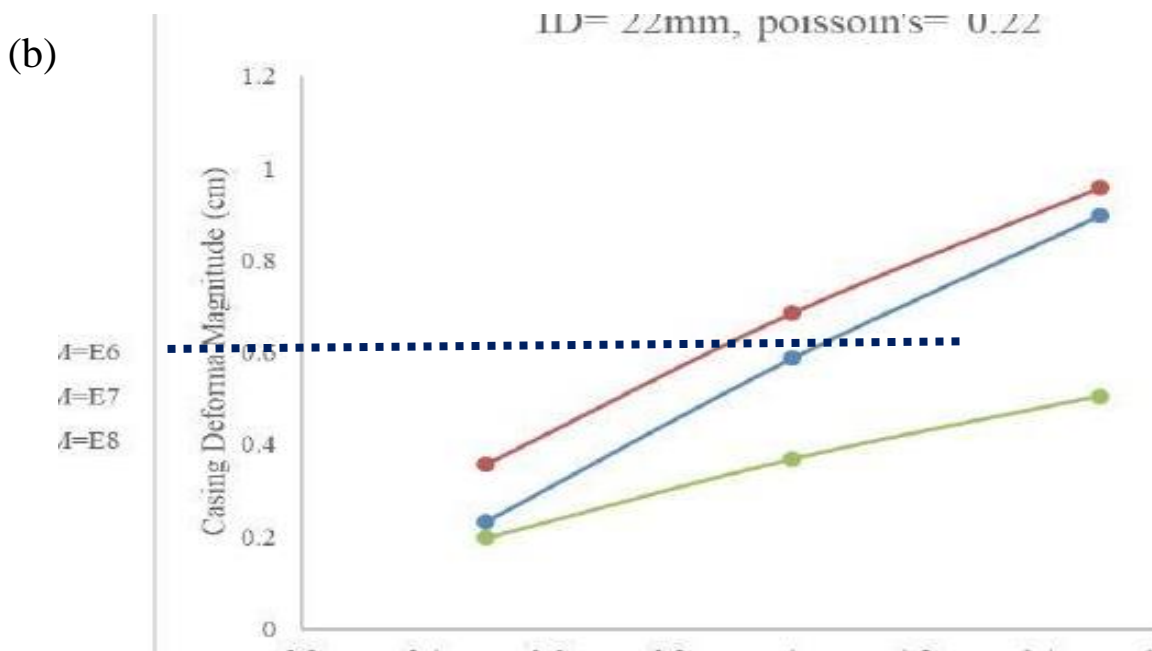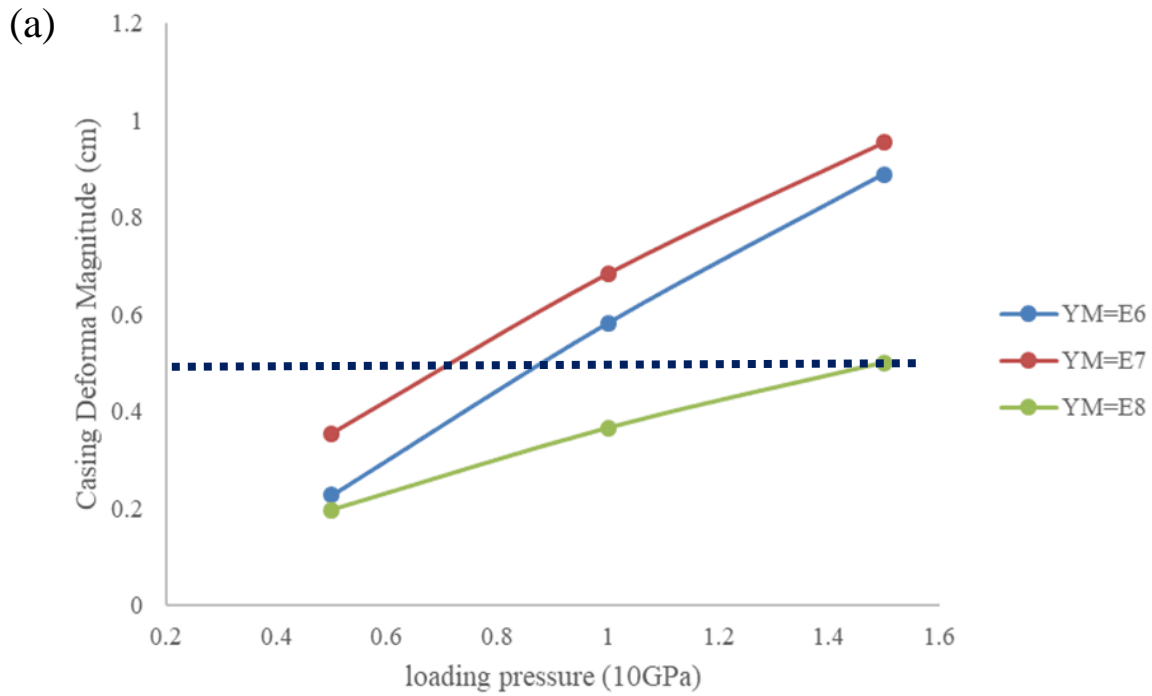
Figure 59: 220mm cement OD, upper is poissoin's ratio 0.14, lower is for poissoin's ratio 0.22. As 10 GPa results in a similar proportion of deforming regarding the real case. A lower loading-smaller amount of formation slippage; and a higher loading- a larger amount of detect slippage are simulated. The dashed line indicated a 0.5 cm causing displacement.

Cement mechanical properties determined by cement compressive strength and tensile strength. Since the cement is one of the possible sections that may be used to relieving the displacement magnitude. Foam cement had been tested on 2 wells in the past for Longmaxi thus studied in this section.

Iverson, et al. [81] compared neat cement with foam and elastomer cement. **Table 15** lists properties for different cement. Neat cement has the largest density. Adding elastomer and nitrogen into cement reduces cement compression strength. Foam cement has the lowest Poisson's ratio and elastomer cement gave the smallest young's modulus. These mechanical properties may change with a different mixture of cement sack and water. Mechanical property ranges from this table provide a sensitivity study scope in the table provided that is necessary to better interpret sensitivity studies.
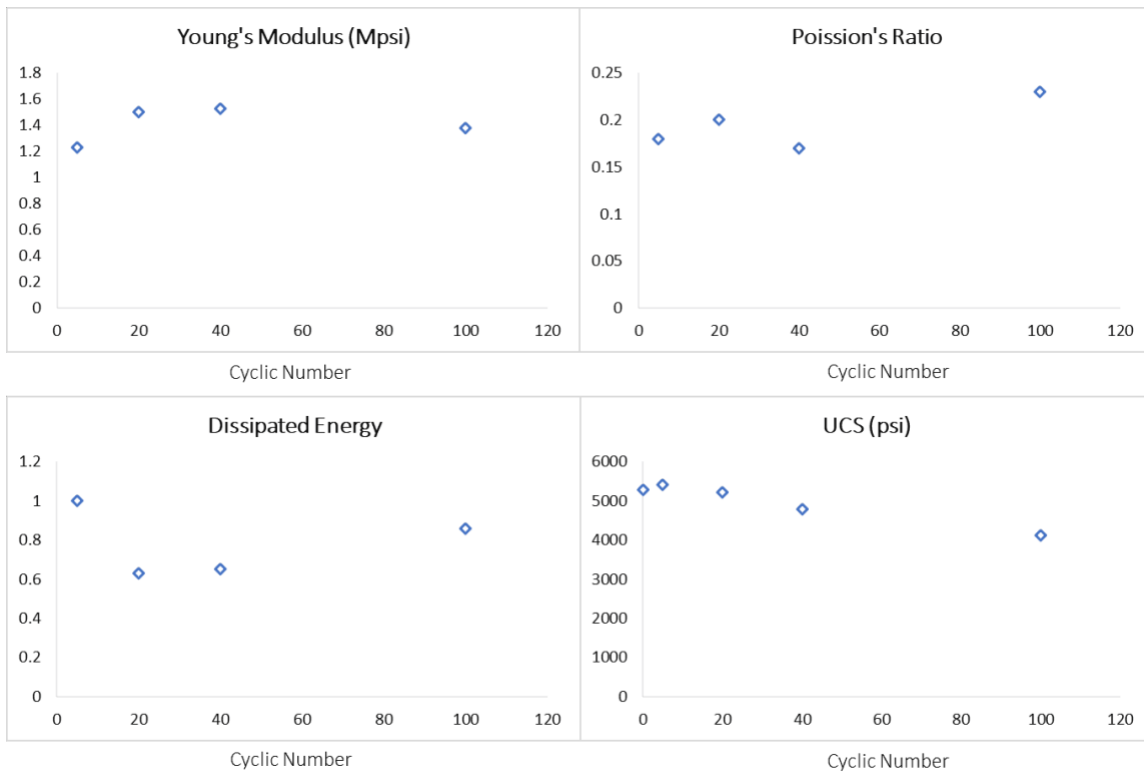
Figure 60: Mechanical properties' behaviors for 5, 20, 40, and 100 cyclical loadings [82]

Shadravan, et al. [82] studied fatigue impacts onto cement mechanical properties, authors tested specimens with loading cycles of 0, 5, 20, 40, 100. McDaniel, et al. [83] aimed to test the impact of cyclic stress applied to the cement component. From the conclusion, young's modulus and uniaxial compression strength decrease with the number of cycles increased

Sensitivity study about cement annular thickness combined with mechanical properties (Young's Modulus, and Poisson's ratio) and pressure loading, simulating the stress applied by movement of matrixes. Their basic structure is plotted in **Figure 61**. Outer diameters for cement annulus are 194 mm, 216 mm, and 244 mm respectively labeled in the figure. **Figure 62 and Figure 63** are comparative plots for cement sheath thickness, poison's ratio, and Youngs Modulus. From these figures with 10 GPa pressure, Young's modulus has around 3mm reduction increasing from 10GPa to 100GPa. Reduction of deform is within 1mm for increasing cement thickness. Increase Possion's ratio has the smallest impact upon reduction the deformation. These sensitivity studies are under 10 GPa loading in the near-wellbore area. It can be observed that large Young's Modulus still has the best stability, both poison's ratio (**Figure 62**) and thickness (**Figure 63**) do not have visible impact for large Young's Modulus.
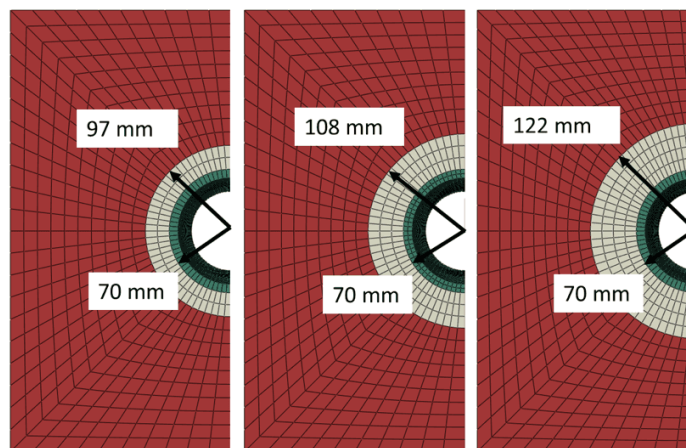
Figure 61: Sensitivity study about cement thickness.
Cement wall thicknesses using 13.5mm, 19mm, and 21 mm respectively. Casing size with ID=60mm and OD= 70mm.

(a)

(b)
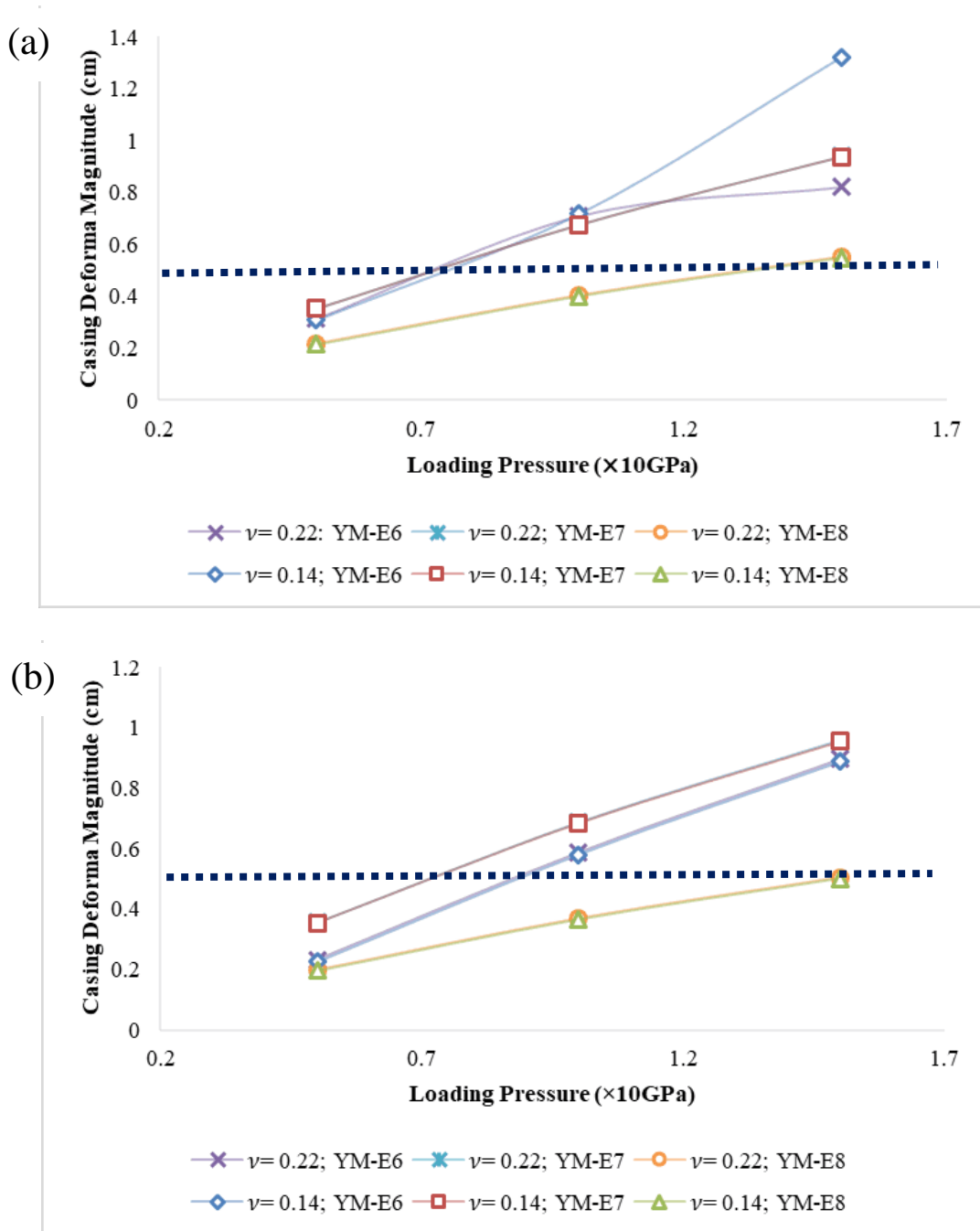
Figure 62: Poisson's ratio study.
For cement OD at (a)194mm and (b)220mm, Poisson's ratio is tested for 0.14 and 0.22 with Young's Modulus selected as 1 GPa (E6), 10 GPa (E7), and 100 GPa (E8). It is obvious that Poisson's ratio is not the critical parameter for providing protection to casing from displacement.

(a)

(b)
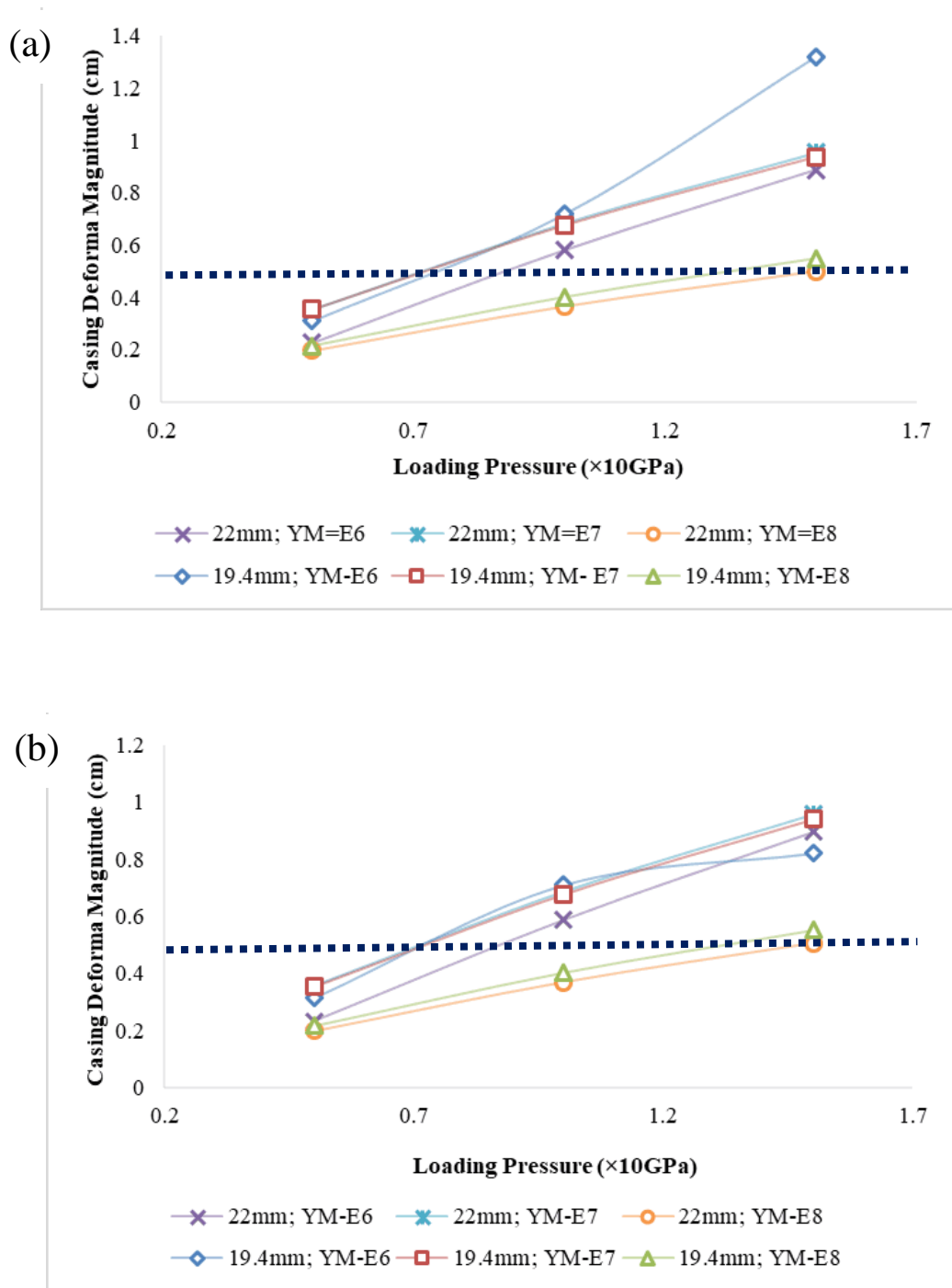
Figure 63：Cement sheath thickness sensitivity study.
(a) for 0.14 Poisson's ratio (b) for 0.22 Poisson's ratio. Under a constant casing diameter, Young's Modulus selected as 1 GPa (E6), 10 GPa (E7), and 100 GPa (E8).

Elastomer cement has the properties of smaller Young's modulus, compression strength, cohesion, and moderate poison's ratio. From **Figure 63,** a consistent trend can be observed that a higher Young's Modulus reduces the displacement magnitude. Thus, elastomer cement might not be appropriate material use to prevent the casing from large deformation.

The properties of foam cement compare with traditional cement and elastomer cement are shown in **Table 15**. From the certain cement mixture used for measurement in **Table 15,** foam cement has lower Young's Modulus, compression strength, tensile strength, poison's ratio, and cohesion. Moreover, it has a void ratio since the foam cement is generated from injecting nitrogen mostly. A void ratio is added to cement section and went over the same range of pressure on the top of near wellbore region. The difference in change in displacement is either negligible or no difference (**Figure 64**). There are 2 filed cases tried with foam cement completion in Changning-Weiyuan. Both well also encounters casing deformation, without a clear sign of displacement magnitude reduction [84]. Therefore, foam cement might not be a proper approach to trying to prevent large casing deformation. Unless further lab experiment proofs its impact upon alleviating casing deformation.

Table 15： **Mechanical properties for cement compare with foam cement and elastomer cement** [81]

Mechanical properties	Unit	Neat	Foam	Elastomer
Young's modulus	psi	1.81×10^6	8.08×10^5	4.91×10^5
Compression Strength	psi	6851	1052	1350
Tensile Strength	psi	429	190	218
Poisson's Ratio	-	0.2	0.151	0.205
Cohesion	psi	2208	391	540
Friction Angle	°C	24.84	12.49	13.58

In addition, Dooply, et al. [85] mentioned that the foam quality would change 70% at the surface and 10% downhole. There is large uncertainty about the foam cement density. Due to the probable density and rheology variation in the pumping process, the density of the foam cement

ranging in a large span. Considering the foam cement experiment done by Joao, et al. [86], operation with foam cement would ask for a longer thickening time and curing time for cement strength to develop. Comparing the foamed cement volume with the neat cement volume, the potential porosity of foam cement is about 28%. Thus, a sensitivity study about foam cement material porosity is set for 10%, 20%, and 30%. Equivalent to the void ratio of 11.1%, 23%, and 35%.
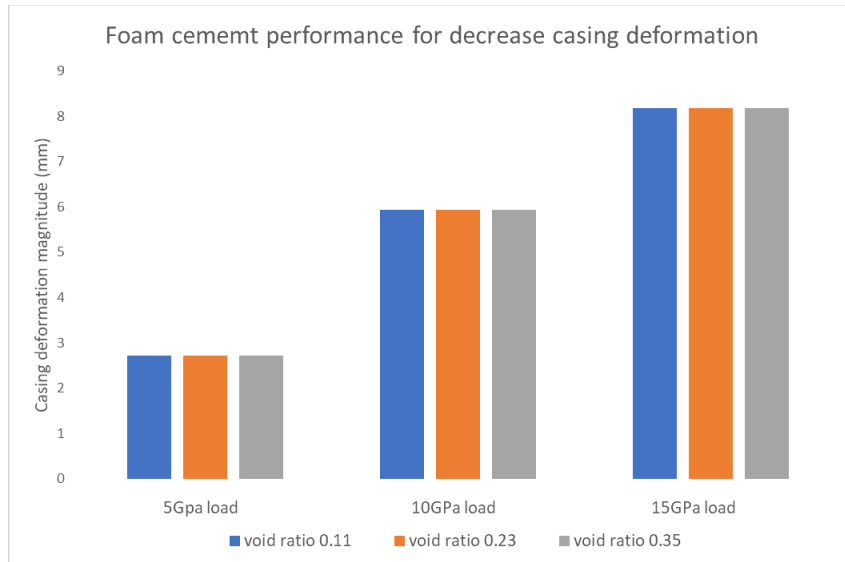
Figure 64: Displacement of foam cement.
From this figure, foam cement using porosity of 10%, 20%, and 30%.
will not improve the completion quality thus should not be considered.

Chapter 7: Summaries, Conclusions, and Suggestions

7.1   Summaries

The improvement of casing cement strength has some effects under geological interface slippage. Before drilling, it is necessary to examine well placement. And before hydraulic fracture, it is important to adjust the stimulation zone [9]. Increasing fracture lateral to avoid faults is proved to have a smaller casing deformation potential with a higher production rate in long-term [86]. Perforation design and fieldwork results are summarized in this section. Since the most simulated injection-induced stress does not exceed casing yield strength, fault interface does not slip during injection period.

An engineering completion design is shown in **Figure 65**. Gamma-ray is a plot in the first column, minimum stress gradient (σ_h), where red indicating low σ_h and blue indicating high σ_h. Column three composed rock quality (RQ) and completion quality (CQ). RQ including organic content, thermal maturity, effective porosity, permeability, saturation, organic shale thickness, and original hydrocarbon in place. This information is gathered from wellbore directional surveys, gamma-ray, petrophysics, and matrix mechanical properties. CQ including matrix mineralogy, mechanical properties, reservoir geomechanics, and analysis of natural fracture network. Columns 4 and 5 are geometric stage design and adjusted stage design respectively. The blue bar on each side of the column indicating the perforation location design with combination analysis with reservoir quality (RQ) and completion quality (CQ). Stage interval was adjusted from geometric to engineering design, which optimizes well productivity and reduces deform risk. Later stages designed with longer intervals and the front stages designed denser shown in the figure. The total fracture stage number decreased from 18 stages to 13 stages. The perforation design follows the same trend of the stage length selection. Comparing the last stages with the front stages, the

perforation spacing is almost doubled relative to geometric design. They also claimed that the optimum perforation clusters selection (PCs) should create by selecting similar matrix breakdown pressure. The designing process composed of pre-data averaging, segmenting the fracturing stages, dividing sections with similar matrix properties, and choosing perforation points that provided similar fracture initiation pressures. Lithology layers are differentiated into separate stimulation sections. This adjustment reduces stimulation stages. Engineering designed well had 10.3% higher in production pumping rate and 5.7% lower treating pressures compare with isometric fractured well [87].

Dong, et al. [84] presented a four-step flowchart (**Figure 66**) after encountering casing deformation. Firstly, use the caliper log to measure casing ID. Secondly, test a smaller size completion equipment. Thirdly, try to complete stimulation use coiled tubing. The very last option is to abandon intervals with the failure of previous three steps.
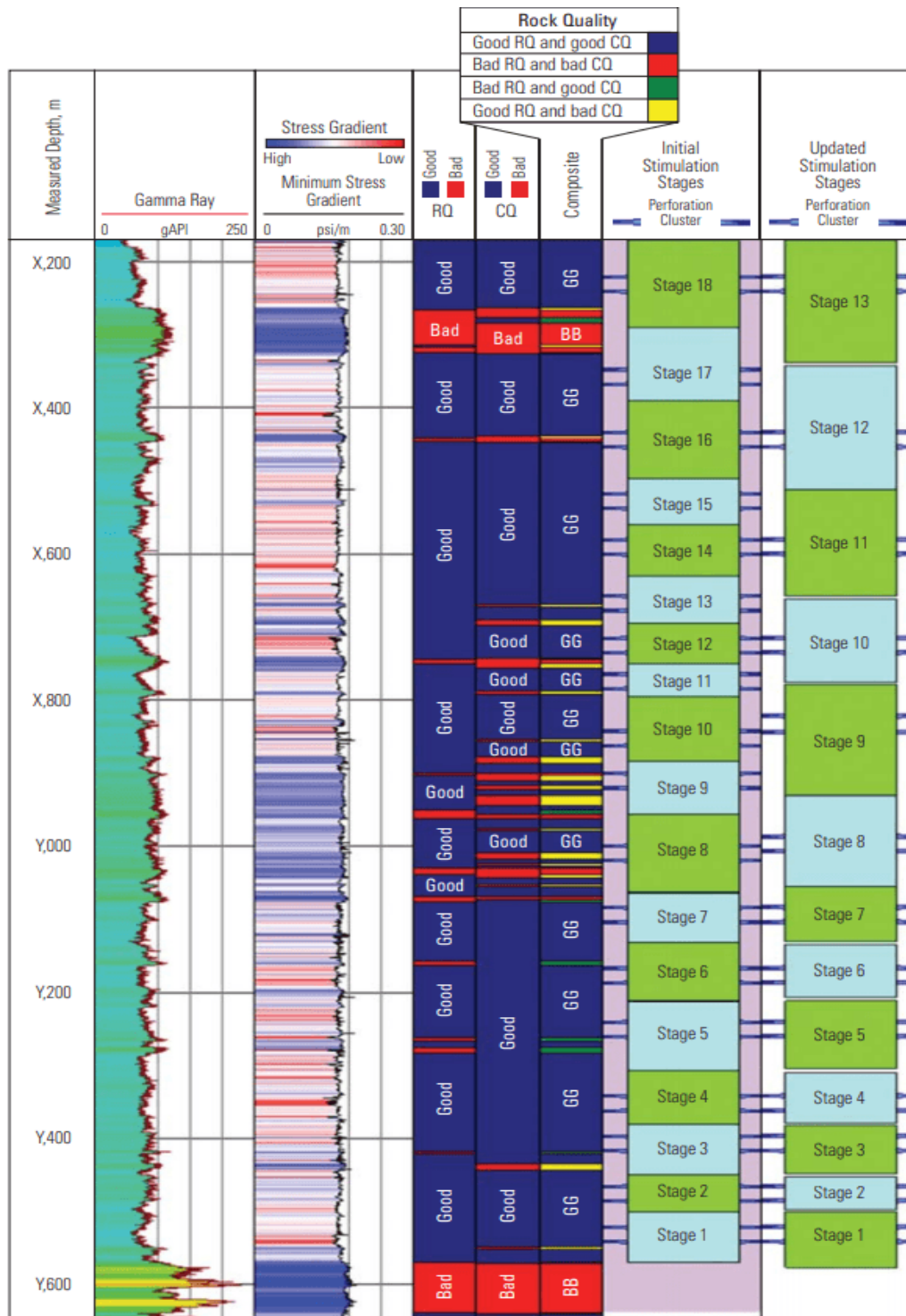
Figure 65: Completion stage optimization from the geometric design toward engineering design [87].
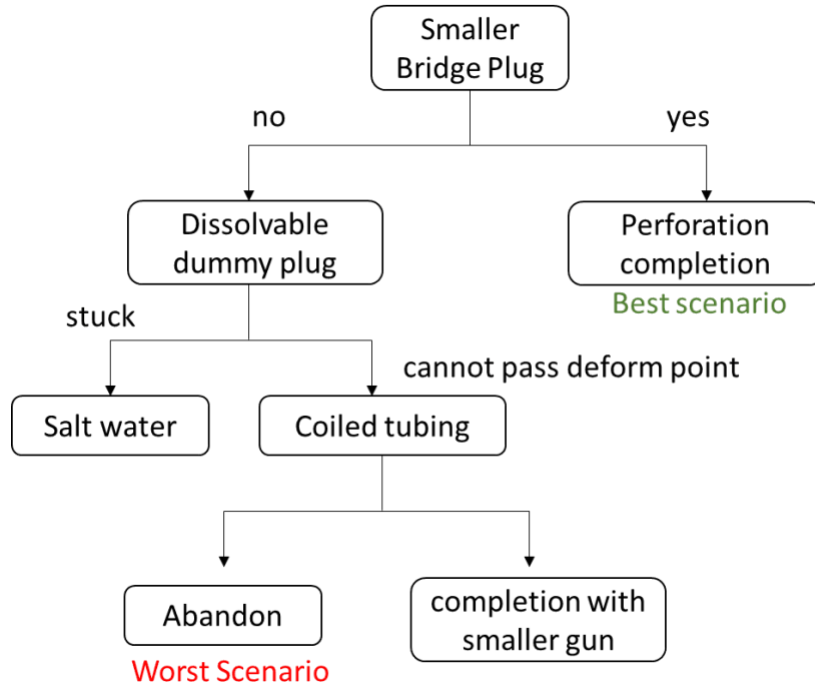
Figure 66: Flowchart after encountering casing deformation during hydraulic fracture. 84

7.2   Conclusions

- Cement is the easiest part of completion yet can impact completion quality in a great deal. On one hand, cement with large Young's modulus can provide better wellbore stability and integrity. On the other hand, increase cement annular thickness could reduce casing deformation with low Young's Modulus cement section.

- Increasing casing wall thickness or steel grade is viable for reducing casing deformation magnitude. However, additional cost spends on casing and abandon cost are huge.

- The most vital approach for casing deformation risk control is to combine formation evaluation and completion quality investigation into a combination index. Fracturing stage interval and perforation location selection need comprehensive design including in-situ stresses, geological settings, and lithology.

- Based on the engineering design of fracturing stages and perforation point, researchers stated that control fracture initiating pressure is critical for complex and layered formation. Similar breakdown pressure helps to maintain wellbore stability.

- The best approach encountering weakly bonded interfaces is to avoid hydraulic fracture near that certain area. A slippage magnitude more than 10 mm might be unable to decrease by increasing casing ID, wall thickness, or changing cement properties. Some studies and articles had provided their design for natural fracture enriched area and highly recommend increase stage distance and design stimulation plan with the evaluation of formation and completion quality.

7.3   Suggestions

The best approach is to design reservoir stimulation plan, including stages lengths and perforation points, according to geological conditions. Further study should be focused on optimizing stimulation design. Adjusted design also proved with a higher fracturing efficiency and lower deformation potential compare with geometric design. Good RQ and CQ sections composite stimulation stages. It is impossible to prevent interfaces reactivation during hydraulic fracture.

Displacement magnitude is the primary risk caused by fault reactivation. Microseismic can be used for fracture mapping, which helps to increase stimulation efficiency and avoid easily activated zone. It is important to investigate fracture geometry as it helps interpreting geological conditions and provides reliable data for simulation as this is the major factor that cannot be controlled with any artificial techniques but contributes hugely in operation. Cement strength depends on the operation. And weak cement strength or partially filled annuli apply abnormal pressure on casing instead of providing support. Thus, it is necessary to maintain a good completion quality for reduce casing deformation.

References

1.   Chen, S.; Zhu, Y.; Qin, Y.; Wang, H.; Liu, H.; Fang, J., Reservoir evaluation of the Lower Silurian Longmaxi Formation shale gas in the southern Sichuan Basin of China. *Marine and Petroleum Geology* **2014,** *57*, 619-630.
2.   Yang, R.; He, S.; Hu, Q.; Hu, D.; Yi, J., Geochemical characteristics and origin of natural gas from Wufeng-Longmaxi shales of the Fuling gas field, Sichuan Basin (China). *International Journal of Coal Geology* **2017,** *171*, 1-11.
3.   Wang, Y.; Dong, D.; Li, X.; Huang, J.; Wang, S.; Wu, W., Stratigraphic sequence and sedimentary characteristics of Lower Silurian Longmaxi Formation in Sichuan Basin and its peripheral areas. *Natural Gas Industry B* **2015,** *2* (2-3), 222-232.
4.   He, Z.; Hu, Z.; Nie, H.; Li, S.; Xu, J., Characterization of shale gas enrichment in the Wufeng Formation–Longmaxi Formation in the Sichuan Basin of China and evaluation of its geological construction–transformation evolution sequence. *Journal of Natural Gas Geoscience* **2017,** *2* (1), 1-10.
5.   King, G. E. In *Thirty years of gas shale fracturing: What have we learned?*, SPE Annual Technical Conference and Exhibition, Society of Petroleum Engineers: 2010.
6.   Warpinski, N.; Lorenz, J.; Branagan, P.; Myal, F.; Gall, B., Examination of a Cored Hydraulic Fracture in a Deep Gas Well (includes associated papers 26302 and 26946). *SPE Production & Facilities* **1993,** *8* (03), 150-158.
7.   Fisher, M. K.; Wright, C. A.; Davidson, B. M.; Goodwin, A.; Fielder, E.; Buckler, W.; Steinsberger, N. In *Integrating fracture mapping technologies to optimize stimulations in the Barnett Shale*, SPE annual technical conference and exhibition, Society of Petroleum Engineers: 2002.
8.   Weijers, L.; Wright, C.; Mayerhofer, M.; Pearson, M.; Griffin, L.; Weddle, P. In *Trends in the North American Frac Industry: Invention through the Shale Revolution*, SPE Hydraulic Fracturing Technology Conference and Exhibition, Society of Petroleum Engineers: 2019.
9.   Meyer, J. J.; Gallop, J.; Chen, A.; Reynolds, S.; Mildren, S. In *Can Seismic Inversion Be Used for Geomechanics? A Casing Deformation Example*, Unconventional Resources Technology Conference, Houston, Texas, 23-25 July 2018, Society of Exploration Geophysicists, American Association of Petroleum …: 2018; pp 438-444.
10.   Yan, W.; Zou, L. Z.; Li, H.; Deng, J. G.; Ge, H. K.; Wang, H. G., Investigation of casing deformation during hydraulic fracturing in high geo-stress shale gas play. *Journal of Petroleum Science and Engineering* **2017,** *150*, 22-29.
11.   Zeng, J.; Gao, D.; Wang, Y.; Fang, J.; Liu, K. In *Research on the effect of casing deformation on sustained casing pressure*, 52nd US Rock Mechanics/Geomechanics Symposium, American Rock Mechanics Association: 2018.
12.   Chong, Z.; Li, X.; Chen, X., Effect of injection site on fault activation and seismicity during hydraulic fracturing. *Energies* **2017,** *10* (10), 1619.
13.   Dahi-Taleghani, A.; Olson, J. E., Numerical modeling of multistranded-hydraulic-fracture propagation: accounting for the interaction between induced and natural fractures. *SPE journal* **2011,** *16* (03), 575-581.

14.   Gale, J. F.; Holder, J. In *Natural fractures in some US shales and their importance for gas production*, Geological Society, London, Petroleum Geology Conference Series, Geological Society of London: 2010; pp 1131-1140.

15.   Bunger, A. P.; Kear, J.; Jeffrey, R. G.; Prioul, R.; Chuprakov, D. In *Laboratory investigation of hydraulic fracture growth through weak discontinuities with active ultrasound monitoring*, 13th ISRM International Congress of Rock Mechanics, International Society for Rock Mechanics and Rock Engineering: 2015.

16.   Ma, Y.; Pan, Z.; Zhong, N.; Connell, L. D.; Down, D. I.; Lin, W.; Zhang, Y., Experimental study of anisotropic gas permeability and its relationship with fracture structure of Longmaxi Shales, Sichuan Basin, China. *Fuel* **2016,** *180*, 106-115.

17.   Yan, W.; Ge, H.; Wang, J.; Wang, D.; Meng, F.; Chen, J.; Wang, X.; McClatchey, N. J., Experimental study of the friction properties and compressive shear failure behaviors of gas shale under the influence of fluids. *Journal of Natural Gas Science and Engineering* **2016,** *33*, 153-161.

18.   Dusseault, M. B.; Bruno, M. S.; Barrera, J., Casing Shear: Causes, Cases, Cures. **2001**.

19.   Daneshy, A. A., Impact of Off-Balance Fracturing on Borehole Stability and Casing Failure. In *SPE Western Regional Meeting*, Society of Petroleum Engineers: Irvine, California, 2005.

20.   Chipperfield, S. T.; Wong, J. R.; Warner, D. S.; Cipolla, C. L.; Mayerhofer, M. J.; Lolon, E. P.; Warpinski, N. R., ShEaR DiLaTioN DiagNoSTiCS—a NEW aPPRoaCh foR EvaLuaTiNg TighT gaS STiMuLaTioN TREaTMENTS. *The APPEA Journal* **2007,** *47* (1), 221-238.

21.   Furui, K.; Fuh, G.-F.; Abdelmalek, N. A.; Morita, N., A Comprehensive Modeling Analysis of Borehole Stability and Production-Liner Deformation for Inclined/Horizontal Wells Completed in a Highly Compacting Chalk Formation. **2010**.

22.   Warpinski, N. R. In *Integrating microseismic monitoring with well completions, reservoir behavior, and rock mechanics*, SPE Tight Gas Completions Conference, Society of Petroleum Engineers: 2009.

23.   Maxwell, S.; Mack, M.; Zhang, F.; Chorney, D.; Goodfellow, S.; Grob, M. In *Differentiating wet and dry microseismic events induced during hydraulic fracturing*, Unconventional Resources Technology Conference, San Antonio, Texas, 20-22 July 2015, Society of Exploration Geophysicists, American Association of Petroleum …: 2015; pp 1513-1524.

24.   Chen, Z.; Jeffrey, R. G.; Zhang, X.; Kear, J., Finite-Element Simulation of a Hydraulic Fracture Interacting With a Natural Fracture. *Spe Journal* **2017,** *22* (1), 219-234.

25.   Haddad, M.; Du, J.; Vidal-Gilbert, S., Integration of Dynamic Microseismic Data With a True 3D Modeling of Hydraulic-Fracture Propagation in the Vaca Muerta Shale. *SPE Journal* **2017**.

26.   Moradian, Z.; Fathi, A.; Evans, B. In *Shear reactivation of natural fractures in hydraulic fracturing*, ARMA Symposium, Houston, 2016.

27.   Daneshy, A. In *Three-Dimensional Analysis of Interactions Between Hydraulic and Natural Fractures*, SPE Hydraulic Fracturing Technology Conference and Exhibition, Society of Petroleum Engineers: 2019.

28.   Dahi Taleghani, A.; Olson, J. E., How natural fractures could affect hydraulic-fracture geometry. *SPE journal* **2013,** *19* (01), 161-171.

29.   Bao, X.; Eaton, D. W., Fault activation by hydraulic fracturing in western Canada. *Science* **2016**, aag2583.

30.   Shrivastava, K.; Sharma, M. M. In *Mechanisms for the formation of complex fracture networks in naturally fractured rocks*, SPE Hydraulic Fracturing Technology Conference and Exhibition, Society of Petroleum Engineers: 2018.

31.   Yin, F.; Han, L. H.; Yang, S. Y.; Deng, Y.; He, Y. M.; Wu, X. R., Casing deformation from fracture slip in hydraulic fracturing. *Journal of Petroleum Science and Engineering* **2018**, *166*, 235-241.

32.   Wang, H.; Liu, H.; Wu, H.; Wang, X., A 3D numerical model for studying the effect of interface shear failure on hydraulic fracture height containment. *Journal of Petroleum Science and Engineering* **2015**, *133*, 280-284.

33.   Qian, B.; Yin, C.; Li, Y.; Xu, B.; Qin, G. In *Diagnostics of Casing Deformation in Multi-Stage Hydraulic Fracturing Stimulation in Lower Silurian Marine Shale Play in Southwestern China*, Unconventional Resources Technology Conference, San Antonio, Texas, 20-22 July 2015, Society of Exploration Geophysicists, American Association of Petroleum …: 2015; pp 402-415.

34.   Lian, Z. H.; Yu, H.; Lin, T. J.; Guo, J. H., A study on casing deformation failure during multi-stage hydraulic fracturing for the stimulated reservoir volume of horizontal shale wells. *Journal of Natural Gas Science and Engineering* **2015**, *23*, 538-546.

35.   Chen, Z.; Shi, L.; Xiang, D., Mechanism of casing deformation in the Changning–Weiyuan national shale gas demonstration area and countermeasures. *Natural Gas Industry B* **2017**, *4* (1), 1-6.

36.   Sugden, C.; Johnson, J.; Chambers, M.; Ring, G.; Suryanarayana, P., Special considerations in the design optimization of the production casing in high-rate, multistage-fractured shale wells. *SPE Drilling & Completion* **2012**, *27* (04), 459-472.

37.   Xi, Y.; Li, J.; Liu, G. H.; Cha, C. Q.; Fu, Y. Q., Numerical investigation for different casing deformation reasons in Weiyuan-Changning shale gas field during multistage hydraulic fracturing. *Journal of Petroleum Science and Engineering* **2018**, *163*, 691-702.

38.   Daneshy, A. A. In *Hydraulic fracturing of horizontal wells: Issues and insights*, SPE Hydraulic Fracturing Technology Conference, Society of Petroleum Engineers: 2011.

39.   Tian, Z.; Shi, L.; Qiao, L., Problems in the wellbore integrity of a shale gas horizontal well and corresponding countermeasures. *Natural Gas Industry B* **2015**, *2* (6), 522-529.

40.   Tiejun, L.; Hao, Y.; Zhanghua, L.; Biao, S., Casing failure mechanism during volume fracturing: A case study of shale gas well. *Advances in Mechanical Engineering* **2017**, *9* (8), 1687814017717182.

41.   Maxwell, S. C.; Urbancic, T. I.; Steinsberger, N.; Zinno, R., Microseismic Imaging of Hydraulic Fracture Complexity in the Barnett Shale. In *SPE Annual Technical Conference and Exhibition*, Society of Petroleum Engineers: San Antonio, Texas, 2002.

42.   Amirhesari, N.; Tani, K. In *Literature Review On Prediction Of Surface Deformation Caused By Fault Dislocation*, ISRM International Symposium-6th Asian Rock Mechanics Symposium, International Society for Rock Mechanics and Rock Engineering: 2010.

43.   Jaeger, J., Cook., NGW Fundamentals of Rock Mechanics. McGraw Hill: 1979.

44.   Zoback, M. D., *Reservoir geomechanics*. Cambridge University Press: 2010.

45.   Terzaghi, K.; Peck, R. B.; Mesri, G., *Soil mechanics in engineering practice*. John Wiley & Sons: 1996.

46.   Renshaw, C.; Pollard, D. In *An experimentally verified criterion for propagation across unbounded frictional interfaces in brittle, linear elastic materials*, International journal of rock mechanics and mining sciences & geomechanics abstracts, Elsevier: 1995; pp 237-249.

47.   Gu, H.; Weng, X. In *Criterion for fractures crossing frictional interfaces at non-orthogonal angles*, 44th US rock mechanics symposium and 5th US-Canada rock mechanics symposium, American Rock Mechanics Association: 2010.

48.   Sarmadivaleh, M.; Rasouli, V., Modified Reinshaw and Pollard criteria for a non-orthogonal cohesive natural interface intersected by an induced fracture. *Rock mechanics and rock engineering* **2014,** *47* (6), 2107-2115.

49.   Wu*, K.; Olson, J. In *Mechanics analysis of interaction between hydraulic and natural fractures in shale reservoirs*, Unconventional Resources Technology Conference, Denver, Colorado, 25-27 August 2014, Society of Exploration Geophysicists, American Association of Petroleum …: 2014; pp 1824-1841.

50.   Benzeggagh, M. L.; Kenane, M., Measurement of mixed-mode delamination fracture toughness of unidirectional glass/epoxy composites with mixed-mode bending apparatus. *Composites science and technology* **1996,** *56* (4), 439-449.

51.   Shet, C.; Chandra, N., Analysis of energy balance when using cohesive zone models to simulate fracture processes. *Journal of engineering materials and technology* **2002,** *124* (4), 440-450.

52.   Irwin, G. R., Analysis of stresses and strains near the end of a crack traversing a plate. *J. appl. Mech.* **1957**.

53.   Griffith, A. A., VI. The phenomena of rupture and flow in solids. *Philosophical transactions of the royal society of london. Series A, containing papers of a mathematical or physical character* **1921,** *221* (582-593), 163-198.

54.   Yuan, J.; Zhou, J.; Liu, S.; Feng, Y.; Deng, J.; Xie, Q.; Lu, Z., An improved fracability-evaluation method for shale reservoirs based on new fracture toughness-prediction models. *SPE Journal* **2017,** *22* (05), 1,704-1,713.

55.   Settgast, R. R.; Fu, P. C.; Walsh, S. D. C.; White, J. A.; Annavarapu, C.; Ryerson, F. J., A fully coupled method for massively parallel simulation of hydraulically driven fractures in 3-dimensions. *International Journal for Numerical and Analytical Methods in Geomechanics* **2017,** *41* (5), 627-653.

56.   Zielonka, M. G.; Searles, K. H.; Ning, J.; Buechler, S. R. In *Development and validation of fully-coupled hydraulic fracturing simulation capabilities*, Proceedings of the SIMULIA community conference, SCC2014, 2014; pp 19-21.

57.   ABAQUS, F., ABAQUS 6.14 Documentation. *Dassault Syst Provid Google Scholar* **2014**.

58.   Yew, C.; Ma, M.; Hill, A. In *A study of fluid leakoff in hydraulic fracture propagation*, International Oil and Gas Conference and Exhibition in China, Society of Petroleum Engineers: 2000.

59.   Economides, M. J.; Nolte, K. G., *Reservoir stimulation*. Prentice Hall Englewood Cliffs, NJ: 1989; Vol. 2.

60.   Ghaderi, A.; Taheri-Shakib, J.; Sharifnik, M. A., The effect of natural fracture on the fluid leak-off in hydraulic fracturing treatment. *Petroleum* **2019,** *5* (1), 85-89.

61.   Mayerhofer, M.; Economides, M., Fracture-injection-test interpretation: leakoff coefficient vs. permeability. *SPE Production & Facilities* **1997,** *12* (04), 231-236.

62.   Warpinski, N.; Teufel, L., Influence of geologic discontinuities on hydraulic fracture propagation (includes associated papers 17011 and 17074). *Journal of Petroleum Technology* **1987,** *39* (02), 209-220.

63.   Roussel, N. P.; Sharma, M. M., Optimizing fracture spacing and sequencing in horizontal-well fracturing. *SPE Production & Operations* **2011,** *26* (02), 173-184.

64.   Meyer, B. R.; Bazan, L. W. In *A discrete fracture network model for hydraulically induced fractures-theory, parametric and case studies*, SPE hydraulic fracturing technology conference, Society of Petroleum Engineers: 2011.

65.   Haddad, M.; Sepehrnoori, K., Simulation of hydraulic fracturing in quasi-brittle shale formations using characterized cohesive layer: Stimulation controlling factors. *Journal of Unconventional Oil and Gas Resources* **2015,** *9*, 65-83.

66.   Dugdale, D. S., Yielding of steel sheets containing slits. *Journal of the Mechanics and Physics of Solids* **1960,** *8* (2), 100-104.

67.   Barenblatt, G. I., The Mathematical Theory of Equilibrium Cracks in Brittle Fracture. In *Advances in Applied Mechanics*, Dryden, H. L.; von Kármán, T.; Kuerti, G.; van den Dungen, F. H.; Howarth, L., Eds. Elsevier: 1962; Vol. 7, pp 55-129.

68.   Turon, A.; Dávila, C. G.; Camanho, P. P.; Costa, J., An engineering solution for mesh size effects in the simulation of delamination using cohesive zone models. *Engineering Fracture Mechanics* **2007,** *74* (10), 1665-1682.

69.   Systèmes, D., Abaqus Analysis User's Guide. *Solid (Continuum) Elements* **2014,** *6*.

70.   Benzeggagh, M.; Kenane, M., Measurement of mixed-mode delamination fracture toughness of unidirectional glass/epoxy composites with mixed-mode bending apparatus. *Composites science and technology* **1996,** *56* (4), 439-449.

71.   Geertsma, J.; De Klerk, F., A Rapid Method of Predicting Width and Extent of Hydraulically Induced Fractures. **1969**.

72.   Nierode, D., Comparison of hydraulic fracture design methods to observed field results. *Journal of petroleum technology* **1985,** *37* (10), 1,831-1,839.

73.   Cipolla, C.; Warpinski, N.; Mayerhofer, M.; Lolon, E.; Vincent, M., The Relationship Between Fracture Complexity, Reservoir Properties, and Fracture Treatment Design. Paper SPE 115769 presented at the SPE ATC&E, Denver, Colorado, 21–24 September. 2008.

74.   Economides, M. J.; Hill, A. D.; Ehlig-Economides, C.; Zhu, D., *Petroleum production systems*. Pearson Education: 2013.

75.   Diehl, T. In *Using ABAQUS cohesive elements to model peeling of an epoxy-bonded aluminum strip: a benchmark study for inelastic peel arms*, DuPont Engineering Technology, Abaqus users conference, 2006.

76.   Rahimi, R., The effect of using different rock failure criteria in wellbore stability analysis. **2014**.

77.   Kalil, I. A.; McSpadden, A. R., Casing burst stresses in particulate-filled annuli: where is the cement? *SPE Drilling & Completion* **2012,** *27* (04), 473-485.

78.   Guo, Y.; Last, N.; Blanford, M. In *Simple Calculation of Compaction-Induced Casing Deformation Adjacent to Reservoir Boundaries*, IADC/SPE Drilling Conference and Exhibition, Society of Petroleum Engineers: 2018.

79.   Feng, Y.; Gray, K., Parameters controlling pressure and fracture behaviors in field injectivity tests: a numerical investigation using coupled flow and geomechanics model. *Computers and Geotechnics* **2017,** *87*, 49-61.

80.   Lele, S.; Tyrrell, T.; Dasari, G. In *Geomechanical analysis of fault reactivation due to hydraulic fracturing*, 51st US Rock Mechanics/Geomechanics Symposium, American Rock Mechanics Association: 2017.

81.   Iverson, B.; Darbe, R.; McMechan, D. In *evaluation of Mechanical Properties of Cements*, The 42nd US Rock Mechanics Symposium (USRMS), American Rock Mechanics Association: 2008.

82.   Shadravan, A.; Kias, E.; Lew, R.; Maharidge, R. In *Utilizing the evolving cement mechanical properties under fatigue to predict cement sheath integrity*, SPE Kuwait Oil and Gas Show and Conference, Society of Petroleum Engineers: 2015.

83.   McDaniel*, J.; Combs, N. K.; Watters, L. In *Zonal isolation assurance: Relating cement mechanical properties to mechanical durability*, Unconventional Resources Technology Conference, Denver, Colorado, 25-27 August 2014, Society of Exploration Geophysicists, American Association of Petroleum …: 2014; pp 2639-2648.

84.   Dong, K.; Liu, N.; Chen, Z.; Huang, R.; Ding, J.; Niu, G., Geomechanical analysis on casing deformation in Longmaxi shale formation. *Journal of Petroleum Science and Engineering* **2019,** *177*, 724-733.

85.   Dooply, M. I.; Flamant, N. C.; Iza Kanahuati, A.; Pringuey, T. In *Foam Cement Job Simulations: Learning from Field Measurements*, SPE Annual Technical Conference and Exhibition, Society of Petroleum Engineers: 2013.

86.   Joao, A. T.; Andrade, G.; Alegria, A. In *Foam Cement Implementation-Deepwater Angola Case Histories*, Abu Dhabi International Petroleum Exhibition & Conference, Society of Petroleum Engineers: 2017.

87.   Miller, C. K.; Waters, G. A.; Rylander, E. I. In *Evaluation of production log data from horizontal wells drilled in organic shales*, North American Unconventional Gas Conference and Exhibition, Society of Petroleum Engineers: 2011.